

FAR-INFRARED FOURIER
TRANSFORM SPECTROSCOPY OF
NTD Ge AND $\text{Ge}_x\text{Si}_{(1-x)}/\text{Si}$ HETEROSTRUCTURES

By



HO FAN JANG, B.Sc., M.Sc.

A Thesis

Submitted to the Faculty of Graduate Studies

in Partial Fulfilment of the Requirements

for the Degree

Doctor of Philosophy

McMaster University

July 1989

FIR STUDIES OF
NTD Ge AND $\text{Ge}_x\text{Si}_{(1-x)}$ /Si HETEROSTRUCTURES

DOCTOR OF PHILOSOPHY(1989)
(Physics)

McMASTER UNIVERSITY
Hamilton, Ontario

TITLE: Far-Infrared Fourier Transform Spectroscopy of
NTD Ge and $\text{Ge}_x\text{Si}_{(1-x)}/\text{Si}$ Heterostructures

AUTHOR: Ho Fan Jang, B.Sc. (Simon Fraser University)
M.Sc. (Simon Fraser University)

SUPERVISORS: Dr. T. Timusk
Dr. A. A. Berezin

NUMBER OF PAGES: xii, 116

ABSTRACT

Far-infrared Fourier transform spectroscopy is used to investigate the excited states of impurities in semiconductors. Two different research projects are presented. The first involves an investigation of the far-infrared absorption of compensated p-type Ge at a temperature of 3 K. The absorption mechanism which is of interest is due to photon-induced hopping transitions of charge carriers between impurity centers. The samples were prepared by neutron transmutation doping (NTD). It is found that the absorption spectra for samples with carrier concentrations ($N_a - N_d$) ranging from 2.3×10^{15} to $2.6 \times 10^{16} \text{ cm}^{-3}$ show a broad absorption with the maximum occurring at a frequency between 10 and 24 cm^{-1} . The absorption coefficient of this maximum ranges between 2 and 87 cm^{-1} . The dynamical change of absorption due to the evolution of the Ga impurity is also presented. The absorption and the frequency of its maximum increase asymptotically with respect to time. It is found that at low frequencies, the absorption coefficient is proportional to frequency. The overall behavior of the absorption spectra is found to be consistent with a theory based on the localized pair model. E. Kaczmarek and Z. W. Gortel have theoretically predicted a sharp peak at 20.4 cm^{-1} on the absorption curve. Its position is independent of the compensation or the impurity concentration of the sample. However, this peak has not been observed in the experimental absorption spectra.

The second project involves the investigation of shallow impurities in selectively boron-doped $\text{Ge}_x\text{Si}_{(1-x)}/\text{Si}$ strained-layer heterostructures using far-infrared photothermal ionization spectroscopy (PTIS). The spectra are obtained under various experimental conditions: with and without band-

ABSTRACT

edge light and by varying the temperature of, and voltage applied to, the sample. The transport properties; resistivity, sheet charge density and Hall hole mobility of these samples are presented. It is found that a sample with a two-dimensional hole gas (2-DHG) behavior at the $\text{Ge}_x\text{Si}_{(1-x)}/\text{Si}$ interface has a weak photoresponse. This is due to the small number of photogenerated carriers in comparison with the residual hole carriers. For samples which do not show 2-DHG behavior, the photoresponse from the substrate plays the dominant role for low applied voltages. At higher voltages, the response from the epitaxial layers becomes evident. The majority impurity was identified as the intentional dopant boron and the dominant minority impurity was found to be phosphorus. It is concluded that although the free carriers are generated in the heavily B-doped layer, those carriers conducted through the low energy, high mobility $\text{Ge}_x\text{Si}_{(1-x)}/\text{Si}$ interface layer, will dominate the photoresponse.

Acknowledgements

I am sincerely thankful to my supervisor, Dr. T. Timusk, for his help, guidance, and for providing an excellent research environment. I wish to thank Dr. Berezin for the encouragement and support during all these years. I also wish to thank Dr. Datars for his help during Dr. Timusk's sabbatical year and for allowing me to work in his lab.

I acknowledge Dr. D. C. Houghton for providing the MBE-GeSi samples used in the research and Mr. J. McCaffrey for characterizing them. I thank Dr. H. Zaleski for initiating the research on the transport properties of these samples. I also wish to thank J. D. Evan for use of the Hall measurement set up.

I wish to express my appreciation to Henry Basista for his assistance in the early stages of this research, and to my friend Greg Cripps for his assistance in preparing the NTD Ge samples and for his continued support in this research.

I have benefited from discussions with Dr. Taylor during the preparation of this thesis. I also wish to express my appreciation to Dr. Haller for corrections made to this thesis.

I would like to thank the assistance of Robert Hughes, Maureen Reedyk and Chris Rymaszewski in the preparation of this thesis. Also, I would like to express my enjoyment in working with them and all the people around the lab.

I wish to thank Bill Scott for his endless supply of liquid helium, and Andy Duncan and Gino Innocente for their technical support.

Acknowledgements

Special thanks goes to my sister for taking the total responsibility for caring for my mother and to those friends who have supported me all these years.

Finally, I wish to express my deepest appreciation to my wife for her understanding and patience, and to my mother and my father for their endless encouragement and love.

TABLE OF CONTENTS

	Page
<i>Abstract</i>	iii
<i>Acknowledgements</i>	v
<i>Table of Contents</i>	vii
<i>List of Tables</i>	ix
<i>List of Figures</i>	x
 CHAPTER 1 INTRODUCTION	 1
1.1 Introduction	1
 CHAPTER 2 FAR-INFRARED ABSORPTION OF NTD GERMANIUM	 5
2.1 Introduction	5
2.2 Absorption Theory for N-Type Materials	10
2.3 Classical Impurity Band.....	13
2.4 Theoretical Absorption for N-Type Si	23
2.5 Absorption Theory for P-Type Materials	27
 CHAPTER 3 EXPERIMENTAL TECHNIQUES	 33
3.1 Introduction	33
3.2 Principle of NTD Ge.....	34

TABLE OF CONTENTS

3.3	Sample Preparation	37
3.4	The FIR Transmission Experiment	43
3.5	Derivation of The Optical Parameters	44
CHAPTER 4 RESULTS AND DISCUSSION.....		51
4.1	Introduction	51
4.2	Absorption Spectra for NTD Ge.....	52
4.3	Time Dependent Spectra for NTD Ge.....	69
4.4	Conclusions	77
CHAPTER 5 PHOTOTHERMAL IONIZATION SPECTROSCOPY OF SELECTIVELY BORON- DOPED $\text{Ge}_x\text{Si}_{(1-x)}/\text{Si}$ STRAINED-LAYER HETEROSTRUCTURES		83
5.1	Introduction	83
5.2	PTIS Technique.....	85
5.3	Selectively Boron-Doped $\text{Ge}_x\text{Si}_{(1-x)}/\text{Si}$ Strained-Layer Heterostructures	92
5.4	Experimental	93
5.5	Transport Properties	95
5.6	PTIS of $\text{Ge}_x\text{Si}_{(1-x)}/\text{Si}$	99
5.7	Conclusions	107
APPENDIX A - Schechter Envelope Functions		111
LIST OF REFERENCES		113

LIST OF TABLES

TABLE

3.1	List of the Natural Abundance, Cross Section and Half-Life of Relevant Ge Isotopes	36
3.2	Physical Data for NTD Ge Samples	41
3.3	Hall Measurement Data for NTD Ge Samples	41
4.1	Refractive Index of NTD Ge at $T = 3$ K	52
4.2	ω_{\max} and $\alpha(\omega_{\max})$ of the absorptions	59
4.3	Properties of Absorption Spectra for NTD Ge	77
5.1	Structural Data for the Selectively B-Doped $\text{Ge}_x\text{Si}_{(1-x)}/\text{Si}$ Strained-Layer Heterostructures	85
5.2	Boron and Phosphorus Excited State Energies	107
A.1	Values of the Parameters for Ge	112

LIST OF FIGURES

FIGURE

2.1	Impurity center configuration relevant to the direct absorption process	12
2.2	The function $(\frac{r}{r_d})F'(\frac{\Omega}{\epsilon_d}, \frac{r}{r_d})$ plotted against $\frac{\Omega/\epsilon_d}{r/r_d}$	18
2.3	The function $f(K)$ plotted against r/r_d as $\Omega \rightarrow 0$	22
2.4	The predicted absorption spectra for n-type Si	24
2.5	(a) Maximum absorption frequency for various doping concentrations. (b) Value of the maximum absorption as function of doping concentration	26
2.6	(a) Dependence of the angular averages of the squares of the energy overlap integrals. (b) Dependence of $R(\omega)$ on the wavelength of radiation for p-type Ge and Si	30
3.1	Time evolution of different impurities in NTD Ge	38
3.2	Top view of the arrangement in the cold working surface of the cryostat.	42
3.3	(a) A transmission spectrum for a NTD GE sample. (b) Absorption spectrum obtained from the fitting routine	48
4.1	Transmission spectra for NTD Ge samples in the region from $0 - 90 \text{ cm}^{-1}$	54
4.2	Absorption spectra for NTD Ge samples in the region from	

LIST OF FIGURES

	30-80 cm^{-1}	56
4.3	Absorption spectra for NTD Ge samples in the region from 0 – 60 cm^{-1}	58
4.4	General properties of the absorption spectra versus impurity concentration	60
4.5	The experimental absorption spectra V1,V2 and V3 obtained by Vavilov <i>et al.</i>	62
4.6	The relative absorption coefficient α/K versus frequency for the theoretical spectra T1 and T2 obtained by E. Kaczmarek <i>et al.</i> for p-type Ge	66
4.7	Comparison of the absorption spectra for NTD Ge samples to that of the n-type Si sample obtained by Neuringer <i>et al.</i> ..	68
4.8	The time dependent resistivity for NTD Ge	70
4.9	Time dependent absorption spectra for NTD Ge	72
4.10	General properties of the absorption spectra versus time for NTD Ge	76
5.1	The two-step ionization process which is the basis of PTIS .	86
5.2	PTI spectra for B-doped Si at various temperature without band-edge light	88
5.3	PTI spectra for the n-type Si substrate at various temperature with and without band-edge light	90
5.4	(a) The energy gap for the $\text{Ge}_x\text{Si}_{(1-x)}/\text{Si}$ strained layer. (b) Typical band diagram for selectively p-doped $\text{Ge}_x\text{Si}_{(1-x)}/\text{Si}$ strained-layer heterostructures	94
5.5	Transport properties for selectively p-doped $\text{Ge}_x\text{Si}_{(1-x)}/\text{Si}$ strained-layer heterostructures	96

LIST OF FIGURES

5.6	PTI spectra for sample S210 at a temperature of 9.8 K, without band-edge light, for two different applied voltages	100
5.7	PTI spectra for sample S222, at a temperature of 6.7 K, without band-edge light, with two different applied voltages	102
5.8	PTI spectra for sample S222, at a temperature of 20.0 K, with band-edge light and three different applied voltages	104

Chapter 1

INTRODUCTION

1.1 INTRODUCTION

An investigation of the interaction between a photon and an electron provides a great deal of insight into the underlying nature of a substance. One of the well-known processes for such an interaction is absorption whereby an electron in state E_1 absorbs a photon with energy $\hbar\omega$, and subsequently goes into an excited state E_2 such that $\hbar\omega = E_2 - E_1$. In semiconductors, optical absorption experiments have provided a lot of vital information; for instance, the refractive index and the absorption coefficient can be used to derive band structures and the bandgap.

An interesting phenomenon in semiconductors is that at sufficiently low temperatures, the electrical properties are governed by the shallow impurities. Studies of such shallow impurities have interested physicists for the

past few decades. Optical absorption is a powerful technique for investigating the excited states of impurities. It has been demonstrated that a detailed understanding of the static and dynamic structures of impurity centers can be obtained from optical spectroscopy. In addition, such understanding often provides further information about the host material.

Since the excited energies of impurity states in semiconductors (e. g., Si, Ge, GaAs) are usually well below 100 meV, optical experiments must be performed using far-infrared radiation. Fourier transform spectroscopy (FTS) is one of the most important tools used in far-infrared optical spectroscopy because it provides a high signal-to-noise ratio combined with the opportunity to obtain a very high resolution.

In this thesis, FTS is used to investigate the excited states of impurities. Two different projects will be presented. The first one involves an investigation of the far-infrared absorption of compensated p-type Ge at a temperature of 3 K. In a compensated semiconductor, it is known that at very low temperatures all of the free carriers freeze out and the main source of conduction is due to a hopping conductivity over the impurities. The main absorption mechanism, which is of interest here, is due to photon-induced hopping transitions of charge carriers between impurity centers. These are the lowest possible excited states of the impurities. The transition energies are below 50 cm^{-1} . A polarizing interferometer which is well suited for low frequency work was used. Such far-infrared absorption experiments are of interest because they provide information regarding the interaction between impurity centers and the nature of disordered systems. Chapters 2 to 4 will be devoted to this research.

The second project involves the investigation of shallow impurities in selectively boron-doped $\text{Ge}_x\text{Si}_{(1-x)}/\text{Si}$ strained-layer heterostructures, grown using molecular-beam epitaxy (MBE). Optical spectroscopy is well suited for such an investigation because highly resolved spectra can identify different impurities in the samples. However, optical absorption spectroscopy alone cannot be used because of the negligible absorption of such a thin epitaxial layer ($< 1\mu\text{m}$). A powerful technique, Photothermal Ionization Spectroscopy (PTIS), which is both sensitive and spectroscopic, is used to probe the shallow impurities in these thin layer samples. Chapter 5 will be devoted to this topic.

Chapter 2

FAR-INFRARED ABSORPTION OF NTD GERMANIUM

2.1 INTRODUCTION

The properties of disordered systems have been a subject of interest to physicists for many years. A great deal of understanding has been gained in the past few decades with regard to the role of electron correlation and disorder on the phenomenon of electron localization. In a lightly doped semiconductor, the electron states near the Fermi level are localized due to strong disorder and small overlap of impurity wave functions.

It is known that at very low temperatures, the conductivity remains non-zero for a compensated semiconductor even though charged carriers have been frozen into donor or acceptor centers. This has been attributed to hopping of charge carriers between empty sites of impurities due to compensation. Many experiments on d.c. and a.c. hopping conductivities at low

temperature have been studied and various theories have been put forward to account for these phenomena.

Both experiment and theory have extended to frequencies corresponding to the far-infrared (FIR). It is not possible to directly measure the high-frequency conductivity. Infrared absorption experiments can, however, be used to study this regime. Studies of the far infrared absorption in shallow-impurity-doped and compensated semiconductors are of interest because they provide information on the interaction between impurity centers, in addition to an understanding of the nature of disordered systems. Theoretical work on the low temperature FIR absorption of lightly-doped n-type materials with a low-compensation ratio ($K < 0.2$) was first done by Blinowski and Mycielski [1]. Their model is based on the localized pair model where the absorption is due to photon-induced hopping transitions of charge carriers in pairs of neutral and ionized donors situated near an ionized acceptor. Their theory has shown some agreement with the absorption measurements reported by Milward *et al.* for n-type Si [2] and Demeshina *et al.* for n-type Ge [3].

However, the situation for p-type materials is not well established. There have been no experiments done on p-type Si and relatively few absorption measurements have been made on p-type Ge. The absorption in Ge:Ga was measured in the $16\text{-}50\text{ cm}^{-1}$ range by Smith *et al.* [4] and Zwerdling *et al.* [5]; however, their measurements are only able to determine the order of magnitude of the absorption coefficients. The absorption in Ge:In was reported for the region extending from $10\text{ to }100\text{ cm}^{-1}$ by Nakagawa *et al.* [6]. Most recently, a study of the absorption of submillimeter and millimeter radiation

(3 to 15 cm^{-1}) on neutron-transmutation doped (NTD) compensated p-type Ge was performed by Vavilov *et al.* [7].

A comparison between the p-type experimental spectra and the n-type theory of Blinowski and Mycielski shows that they differ appreciably. To account for such differences, E. Kaczmarek *et al.* developed an absorption theory for p-type semiconductors [8]. They use essentially the same theoretical model as Blinowski and Mycielski for the n-type case, except that they use a different envelope function to describe the isolated-acceptor ground state. However, the existing experimental data cannot be used to justify the theory. Clearly, more work is needed in order to achieve a better understanding of photon-induced hopping absorption for p-type materials.

In this thesis, the results of far-infrared absorption experiments on compensated NTD Ge at a temperature of 3 K will be presented. The purpose of this research is to investigate the properties of hopping absorptions for p-type Ge in detail and compare them to existing theories. From this analysis, some understanding of the interactions between acceptors, the general characteristics of disordered systems and the effects of electron-electron interactions will be obtained.

NTD Ge is chosen for such studies because of the high quality of this doping technique [9]. The investigation of far-infrared absorption in NTD Ge is of considerable interest since these materials are widely used as sensitive bolometers for the detection of FIR radiation at low temperatures [10]. Moreover, the unique properties of NTD Ge provide the opportunity to study two different dependences of the absorption spectra. First, the dependence of a sample's absorption on impurity concentration with the same degree of compensation can be studied. This is possible for NTD Ge samples because

the concentration is varied by the irradiation time and the compensation is fixed by the nuclear reaction as discussed in Chapter 3. Seven samples with carrier concentrations ($N_a - N_d$) ranging from 1.3 to $26 \times 10^{15} \text{ cm}^{-3}$ were prepared for this experiment. The impurity concentrations of these samples are on the insulator side of the Mott transition [11]. Nevertheless, these samples cover the important range of impurity concentrations in which the results can be compared with the present absorption theory. Second, the dependence of absorption for samples with different majority impurity concentrations, but with the same minority impurity concentration can be studied. This is possible by doing a time dependent absorption experiment after the irradiation as shown in Chapter 3.

In the following sections of this chapter, the necessary background theory for understanding this absorption process is presented. A general overview of the absorption theory due to Blinowski and Mycielski for lightly-doped compensated n-type semiconductors will be introduced in section 2.2. Impurity band structure is needed for calculating absorption coefficients. For a lightly-doped compensated semiconductor, the formation of an impurity band is mainly due to the scattering of levels associated with the randomly distributed Coulomb potentials of charge impurity centers. The classical impurity band theory, which has been studied intensively, is discussed in section 2.3. The Coulomb gap, which is the consequence of the long-range Coulomb interactions between charges, and is significant for materials with an intermediate compensation ratio [12], will be introduced. The effects of this gap, on the absorption spectra, are discussed. Also, included are the effects of dipole-dipole interactions between ionized pairs, which are ignored in the Blinowski and Mycielski theory. To illustrate the general characteristics

of the theoretical results, numerical absorption spectra are presented for n-type Si in section 2.4. Finally, in section 2.5, the absorption theory developed by E. Kaczmarek and Z. W. Gortel for p-type semiconductors is discussed. They use essentially the same theoretical model as Blinowski and Mycielski in the n-type case, except that they use the Schechter envelope function to describe the isolated-acceptor ground state rather than a hydrogen-like ground state. This theory predicts a sharp absorption peak at 20.4 cm^{-1} . Its position does not depend on the compensation or on the concentration of acceptors.

Chapter 3 discusses the basic principle of NTD Ge and how to prepare the samples for the absorption experiments. The details of the FIR transmission experiment are discussed. Finally, the derivation of the optical parameters from the transmission spectra is presented.

Chapter 4 presents the results of the far-infrared absorption experiments. The changes in the absorption spectra due to the change in the impurity concentration with a fixed compensation ratio, and the change of majority impurity concentration with fixed minority concentration are discussed. The general characteristics of the spectra will be compared with the existing theory based on the localized pair model and particularly the spectra predicted by E. Kaczmarek *et al.* for p-type Ge. The spectra are also compared to the experimental work done by Vavilov *et al.* on NTD Ge, and by Milward *et al.* on n-type Si.

2.2 ABSORPTION THEORY FOR N-TYPE MATERIALS

Theoretical investigations of the absorption at low temperatures in the far-infrared for n-type compensated Ge and Si were carried out by Bli-nowski and Mycielski [1], Banaszkiewicz [13], and most recently by Bara-nowskii and Uzakov [14]. At low temperatures, in a compensated n-type semiconductor, all the acceptors, N_a , will be ionized. Therefore, there are an equal number of ionized donors and acceptors, and $(N_d - N_a)$ donors will remain neutral. If the impurity concentration is low, then it is possible to treat the photon absorption as the result of zero-phonon electron transitions in pairs of ionized and neutral donors. This process, called the direct-absorption, was first proposed by Tanaka and Fan [15].

The two lowest electron states of the two-centre Hamiltonian were obtained by Miller and Abrahams as follows [16]:

$$\epsilon^{\pm} = (\varphi_1 + \varphi_2)/2 \pm \Gamma/2, \quad (2.1)$$

where, φ_1 and φ_2 are the ground state energies of the site 1 and site 2 impurities. The energy separation (Γ), denotes separation in energy of these two lowest states with some approximations, and is given by [14],

$$\Gamma = (\Omega^2 + 4I^2)^{1/2}, \quad (2.2)$$

where, Ω is the difference between the coulomb potential energies of the two centers of the donor pair. In general, Ω is created by all the surrounding charges. I is the energy overlap integral which is usually anisotropic. Under the influence of FIR radiation, the electron will be excited from one level to the other. The pairs of donors for which $\Omega \ll 2I$ are called homopolar

pairs; whereas, when $\Omega \gg 2I$ they are called polar pairs. These are shown in Fig. 2.1.

The energy absorbed per unit time by a pair in the presence of an electric field $E = E_0 \cos(\omega t)$ at a temperature, T , such that $kT \ll \varepsilon_d = e^2 N_d^{1/3} / \kappa$ is given by [14],

$$Q = \frac{2\pi}{\hbar} \frac{\hbar\omega}{4} \frac{e^2 E_0^2 r^2 \cos^2 \vartheta}{I^2} I^2 \delta(\hbar\omega - \Gamma) \left[1 - \exp\left(-\frac{\hbar\omega}{kT}\right) \right], \quad (2.3)$$

where, e is the electron charge, κ is the permittivity, r is the separation between sites in the pair, and ϑ is the angle between the vector \vec{r} and the direction of the external field. The absorption coefficient of such a system is given by,

$$\alpha(\omega) = \frac{4\pi}{E_0^2 c \kappa^{1/2}} \int 4\pi r^2 F(\Omega, r) Q d^3 r d\Omega, \quad (2.4)$$

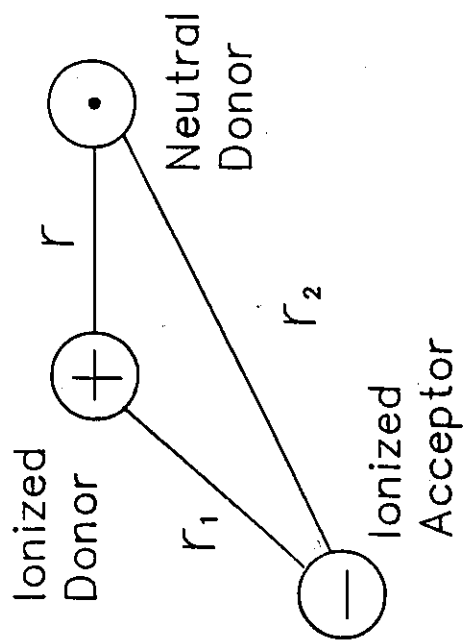
where, c is the speed of light and the distribution function $F(\Omega, r)$ is defined such that $4\pi r^2 F(\Omega, r) dr d\Omega$ is the probability of finding, in a unit volume, a pair consisting of an ionized and neutral donor separated by a distance within the interval $(r, r+dr)$ and with a difference in Coulomb energies within the interval $(\Omega, \Omega + d\Omega)$. To simplify the calculation an approximation is made by taking the angular average of I , $I^2(r) = \langle I^2 \rangle$, which can be substituted into Eqn. (2.4) for computational purposes. Integration of Eqn. (2.4) with respect to Ω and ϑ gives,

$$\alpha(\omega) = \frac{16\pi^3 e^2}{3c\hbar\kappa^{1/3}} \left[1 - \exp\left(-\frac{\hbar\omega}{kT}\right) \right] \int_{r_\omega}^{\infty} \frac{r^4 I^2(r)}{\sqrt{\hbar^2 \omega^2 - 4I^2(r)}} F(\sqrt{\hbar^2 \omega^2 - 4I^2(r)}, r) dr. \quad (2.5)$$

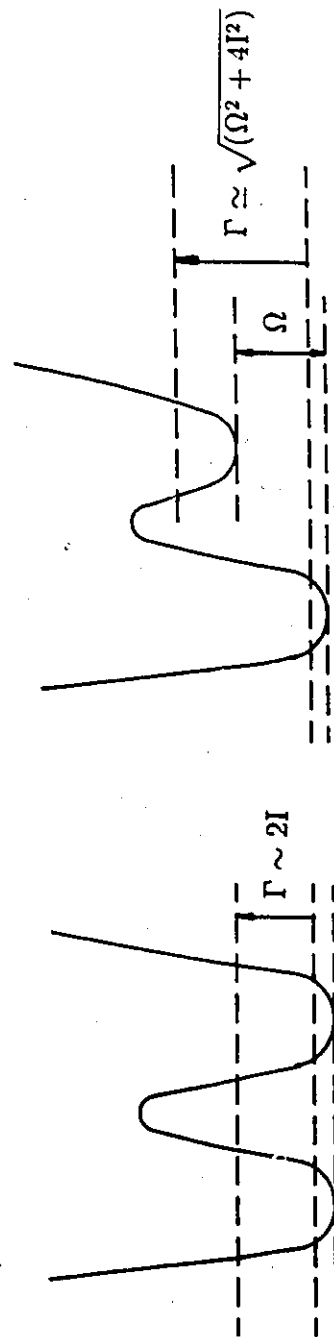
In the above expression, the quantity r_ω is found from the condition $2I(r_\omega) = \hbar\omega$. In the case of hydrogen-like centers such as the donors in Ge or Si, $I(r)$ can be expressed as [16],

$$I(r) = I_0 (r/a)^{3/4} \exp(-r/a), \quad (2.6)$$

Figure 2.1 Impurity center configuration relevant to the direct absorption process for a donor-pair which is situated near an acceptor. The symbols \ominus , \oplus , and \odot refer to the ionized acceptor, ionized donor and neutral donor respectively. Homopolar pairs and polar pairs for the photon-induced electronic transition are also shown.



Localized Pair Model



Homopolar Pair

$$(\Omega \ll 2I)$$

Polar Pair

$$(\Omega \gg 2I)$$

which is valid when $r \gg a$, where a is the localization radius and I_0 is an energy of the order of the donor state energy. Then, r_ω is given by the equation,

$$\frac{r_\omega}{a} = \ln \frac{2I_0(r_\omega/a)^{3/4}}{\hbar\omega}. \quad (2.7)$$

For $r \approx r_\omega$, the energy overlap integral $I(r)$ is large and the denominator in the integral, $(\hbar^2\omega^2 - 4I^2(r))^{1/2}$, remains small. It is clear from Eqn. (2.5) that if $F(\Omega, r)$ is a slowly varying function compared with the exponential function then the main contribution to the absorption at a frequency ω is due to the pairs with an internal distance of the order of r_ω . That is, homopolar pairs will contribute significantly to the absorption process.

2.3 CLASSICAL IMPURITY BAND

Before the function $F(\Omega, r)$ for the impurity band is discussed, it is useful to introduce the single particle density of states (DOS), $g(\epsilon)$, for an impurity band of a lightly-doped semiconductor. For impurity concentrations with $N_d \ll N_M$, where N_M is the critical impurity concentration for the Mott metal-insulator transition which is estimated from $N_M a^3 \approx 0.02$ [11], the electron state can be regarded as strictly localized.

For a lightly-doped semiconductor with a finite degree of compensation, the scatter of energy levels is mainly associated with the Coulomb potentials which are created by randomly distributed charge impurity centers. The quantum overlap of the wave functions of neighbouring states contributes a term containing $\exp[-(N_d^{1/3} a)^{-1}]$ to the energy. If $N_d a^3 \ll 1$, this term is small compared with the Coulomb potentials which are of the order of ϵ_d . The impurity band, for which quantum effects are ignored and only the

electrostatic forces between the charge centers is allowed, is called the classical impurity band (CIB) [12, 17]. In real semiconductors the CIB is valid for $N_d a^3 \leq 0.002$ [12, 17]. Within the CIB model, the DOS of an impurity band has a two-peak structure. It has been predicted by Efros and Shklovskii [18] that the DOS tends to zero as the energy, ε , approaches the Fermi level (μ) and this is known as the Coulomb gap. The origin of such behavior is related to the long-range Coulomb interaction between charges. It can be shown that in the three-dimensional case $g(\varepsilon)$ is of the form [18],

$$g(\varepsilon) \propto \frac{(\varepsilon - \mu)^2 \kappa^3}{e^6}, \quad (2.8)$$

for the states with energy ε close to Fermi level. Eqn. (2.8) is valid provided that the energy $|\varepsilon - \mu|$ is smaller than ε_d such that $e^2/(\kappa|\varepsilon - \mu|)$ exceeds the mean separation between donors. The width of the Coulomb gap (Δ) is defined such that Eqn. (2.8) holds for $|\varepsilon - \mu| < \Delta$. In cases of low or high degrees of compensation, Δ is small compared to the total impurity band width. However, at an intermediate degree of compensation, Δ is of the order of the entire impurity band. Efros [19] also obtained a sharper bound for three-dimensional systems at low energies by considering many particle-hole excitations in which the surrounding electrons were allowed to relax.

$F(\Omega, r)$ is the distribution function for creating particle-hole excitations of separation r and of excitation energy Ω (the Coulomb potential energy difference). If r is much smaller than the mean distance between neighbouring sites, then the occupation and energies of the two sites of a pair are uncorrelated and $F(\Omega, r)$ can be approximated from the single-particle DOS by a convolution as follows [17, 20]:

$$\begin{aligned}
F(\Omega, r) &\approx F^o(\Omega, r) = \int_{\mu}^{\infty} d\varepsilon_1 \int_{-\infty}^{\mu} d\varepsilon_2 g(\varepsilon_1) g(\varepsilon_2) \delta\left(\varepsilon_1 - \varepsilon_2 - \frac{e^2}{\kappa r} - \Omega\right) \\
&= f^o\left(\Omega + \frac{e^2}{\kappa r}\right),
\end{aligned} \tag{2.9a}$$

with

$$f^o(x) = \int_{\mu}^{\mu+x} g(\varepsilon) g(\varepsilon - x) d\varepsilon. \tag{2.9b}$$

In this approximation, $F(\Omega, r)$ depends only on $x = \Omega + e^2/\kappa r$. With the assumption that Eqn. (2.8) is valid for $|\varepsilon - \mu| \ll \Delta$ and $g(\varepsilon) \approx g_o$ for $|\varepsilon - \mu| \gg \Delta$, one obtains [17],

$$F(\Omega, r) \approx \left(\Omega + \frac{e^2}{\kappa r}\right) g_o^2, \quad \text{for } x \gg \Delta \tag{2.9c}$$

$$F(\Omega, r) = \frac{3\kappa^6}{10\pi^2 e^{12}} \left(\Omega + \frac{e^2}{\kappa r}\right)^5 \quad \text{for } x \ll \Delta. \tag{2.9d}$$

For a three-dimensional system with correlation between sites taken into account, the theory of Baranovskii *et al* [21] predicted that the function $F(\Omega, r)$ can be written in the form,

$$F(\Omega, r) = F^o(\Omega, r) \exp\left\{-\frac{r}{r_o} \phi(\Omega, r)\right\}, \tag{2.10a}$$

where, $r_o \approx e^2/\kappa\Delta$. The exponential term takes into account the dipole-dipole interaction (DDI) of pairs. The function $\phi(\Omega, r)$ should tend to zero at $\Omega \gg \Delta$ because the correlation is insignificant. It can be shown that at $\Omega \ll \Delta$ and $r \approx r_o$, the function $\phi(\Omega, r)$ is of the form [21],

$$\phi(\Omega, r_o) \propto \ln^{1/4}(\Delta/\Omega). \tag{2.10b}$$

Let $\Phi(\Omega)$ denote the density of states for pairs with excitation energy Ω . It can be obtained from the following:

$$\Phi(\Omega) = \int F(\Omega, r) dr. \tag{2.10c}$$

It is found that $\Phi(\Omega)$ vanishes as

$$\frac{1}{[\ln(\Delta/\Omega)]^{1/2}} \quad \text{as} \quad \Omega \rightarrow 0. \quad (2.10d)$$

Such behavior, in fact, has similar origin to that which causes the Coulomb gap in the single particle DOS: the behavior of $\Phi(\Omega)$ as shown in Eqn. (2.10d) is due to the long-range dipole-dipole interaction ($\propto 1/r^3$).

The Ω in $F(\Omega, r)$, discussed in Eqns. (2.9) and (2.10), is the excitation energy, Γ , of the pair since it does not take into account the overlap integral $I(r)$. However, the "quantum repulsion" of energy levels increases the excitation energy, Γ , as described in Eqn. (2.2). Therefore, when quantum repulsion is taken into account, the argument, Ω , of the function $F(\Omega, r)$, is no longer the excitation energy of the pair. The function $F(\Omega, r)$ in Section 2.1 depends on the overlap integral because the quantum repulsion changes the occupation of the pair. However, at the low energy region, $\hbar\omega \ll \varepsilon_d$, the quantum effects can be neglected in calculating $F(\Omega, r)$. At a frequency ω , the pairs for which Γ is equal to $\hbar\omega$ will participate in the absorption. It follows from Eqn. (2.2) that the quantum repulsion for such pairs does not exceed $\hbar\omega$. The occupation of a pair depends on the lower energy, ε^- , given in Eqn. (2.1). The value $(\varphi_1 + \varphi_2)/2$ changes in the impurity band from pair to pair by a magnitude of the order of ε_d . In the case of low energy, $\hbar\omega \ll \varepsilon_d$, the quantum repulsion affects only a small fraction of pairs. Therefore, the dependence on the overlap integral energy $I(r)$ can be ignored in calculating the function $F(\Omega, r)$ in a low energy region, $\hbar\omega \ll \varepsilon_d$.

In general, both the DOS and $F(\Omega, r)$ cannot be easily obtained for an impurity band. There is no analytical theory to find the DOS or $F(\Omega, r)$ even if quantum effects are ignored. Baranovskii and Uzakov [14] calculated

$F(\Omega, r)$ by using a Monte Carlo technique to computer model an impurity band within the CIB model. Their results make it possible to calculate, at fairly low frequencies, the absorption coefficient for materials within a wide range of compensation, K , from 0.1 to 0.9.

In the case of small compensation ($K < 0.2$) [1], it can be assumed that all donors except the ones nearest to an acceptor are neutral and that the potential is due to the Coulomb potential of this ionized acceptor. The dipole potentials of other ionized acceptors and ionized donor pairs present in the materials are ignored. As shown in Fig. 2.1, let r_1 and r_2 be the distances from the ionized acceptor to the ionized and neutral donors, respectively. The distance r between the sites in the pair and the Coulomb energy are given by,

$$r = \sqrt{r_1^2 + r_2^2 - 2r_1r_2\cos\theta}, \quad (2.11a)$$

$$\Omega = \frac{e^2}{\kappa} \left(\frac{1}{r_1} - \frac{1}{r_2} \right), \quad (2.11b)$$

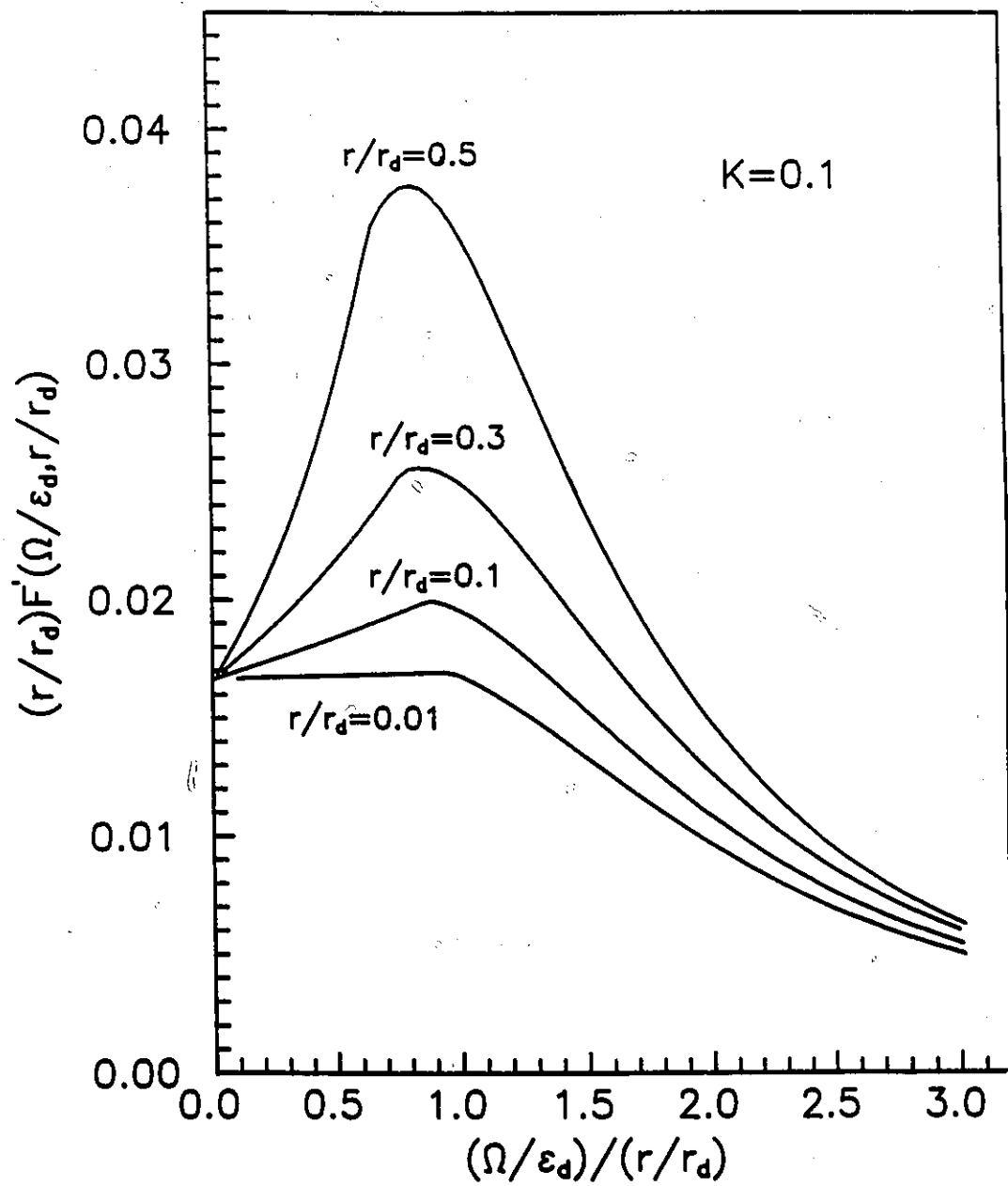
where θ is the angle between the directions of r_1 and r_2 . Under such an assumption, an analytic formula for $F(\Omega, r)$ is given by [22],

$$4\pi r^2 F(\Omega, r) = N_a N_d^2 \int dr_1 dr_2 \exp \left\{ -\frac{4}{3} \pi r_1^3 N_d \right\} \delta \left(r - \sqrt{r_1^2 + r_2^2 - 2r_1r_2\cos\theta} \right) \\ \times \delta \left(\Omega - \frac{e^2}{\kappa r_1} + \frac{e^2}{\kappa r_2} \right). \quad (2.12)$$

Integrating with respect to the angle θ and also with respect to the modulus r_2 , the expression for $F(\Omega, r)$ becomes,

$$F(\Omega, r) = \frac{2\pi N_d^2 N_a \kappa}{r e^2} \int_{R_1}^{R_2} \frac{r_1^4 \exp \left\{ -\frac{4}{3} \pi r_1^3 N_d \right\}}{\left(1 - \frac{\kappa}{e^2} \Omega r_1 \right)^3} dr_1, \quad (2.13a)$$

Figure 2.2 The function $(\frac{r}{r_d})F'(\frac{\Omega}{\epsilon_d}, \frac{r}{r_d})$ plotted against $\frac{\Omega/\epsilon_d}{r/r_d}$ with $K=0.1$.
Curves shown here are calculated with $r/r_d = 0.01, 0.1, 0.3$ and 0.5 .



where,

$$R_1 = \frac{r}{2} + \frac{e^2}{\kappa\Omega} - \frac{1}{2} \sqrt{r^2 + \left(\frac{2e^2}{\kappa\Omega}\right)^2}, \quad (2.13b)$$

$$R_2 = \min \left\{ \frac{1}{2} \sqrt{r^2 + \frac{4e^2 r}{\kappa\Omega}} - \frac{r}{2}, r_\mu \right\} \quad (2.13c)$$

and

$$r_\mu = \frac{e^2}{\kappa\mu}, \quad (2.13d)$$

where $\mu = 0.61\epsilon_d$ is the Fermi energy for a low degree of compensation. r_μ takes into account the fact that the donor nearest to the acceptor will not be ionized if its distance from the acceptor exceeds r_μ .

It is useful to note that the function $F(\Omega, r)$ in the CIB model can be expressed in the following form [14]:

$$rF(\Omega, r) = \frac{\kappa}{e^2} N_d^{4/3} \left\{ \frac{r}{r_d} F' \left(\frac{\Omega}{\epsilon_d}, \frac{r}{r_d} \right) \right\}, \quad (2.14)$$

where, $r_d = (4/3\pi N_d)^{-1/3}$ is the average distance between donors and $F'(\Omega/\epsilon_d, r/r_d)$ is a dimensionless function. In general, $F'(\Omega/\epsilon_d, r/r_d)$ depends on the majority carrier concentration (N_d in n-type) and the degree of compensation, K . In the case of low compensation, $F(\Omega, r)$ is given by Eqn. (2.13a), and $F'(\Omega/\epsilon_d, r/r_d)$ is proportional to K . It follows from Eqn. (2.5) that the (α/K) spectra would be the same for a given value of N_d and the shape of the absorption curve does not depend on the concentration of the minority impurity.

The function $(r/r_d)F'(\Omega/\epsilon_d, r/r_d)$ calculated from Eqns. (2.13) and (2.14) is plotted against $(\Omega/\epsilon_d)/(r/r_d)$ in Fig. 2.2, with $K=0.1$, for different values of r/r_d (0.01, 0.1, 0.3, 0.5). From this figure, it is clear that $rF(\Omega, r)$ decreases steeply for,

$$\frac{\Omega/\epsilon_d}{r/r_d} > 1. \quad (2.15)$$

That is, $\Omega > erE_N$, where $E_N = eN_d^{2/3}/\kappa$ is the characteristic scale. For small r , $rF(\Omega, r)$ is fairly constant for $\Omega < erE_N$.

If the dipole-dipole interaction of pairs is not taken into account for small Ω , then the function $rF(\Omega, r)$ is approximated by a constant for pairs with $r \ll r_d$. It has been shown by S. D. Baranovskii *et al.* [21] that if the localized compact pair description is valid for $r_\omega \ll N_d^{-1/3}$ and if the degree of compensation is not extremely high ($1 - K < 1$), that is, the compact pair can be either neutral or singly ionized, but cannot be doubly ionized, then one can obtain,

$$\lim_{\Omega \rightarrow 0} F(\Omega, r) = \frac{N_d^2 K f(K) e^2}{2(e^2 N_d^{1/3}/\kappa)^2 \kappa r}, \quad (2.16)$$

where, $f(K)$ is a function which mainly depends on the degree of compensation and not on the value of r for the compact pairs. Eqn. (2.16) is derived for the compact pairs; therefore $(\Omega + e^2/\kappa r) \gg \Delta$ holds. The expression for $F(\Omega, r)$ in Eqn. (2.16) does agree with Eqn. (2.9c) for $\Omega \rightarrow 0$. The function $f(K)$ can easily be illustrated in the case of low compensation $K < 0.2$; for instance, $f(K)$ can be derived from Eqn. 2.12 as follows:

$$f(K) = 4\pi \int_{r/2r_d}^{r_\omega/r_d} R^4 \exp\left(-\frac{4}{3}\pi R^3\right) dR. \quad (2.17)$$

Since for compact pairs, $r \ll r_d$, the integral in fact depends on the lower limit $r/2r_d$ very weakly. This is demonstrated in Fig. 2.3. The function $rF(\Omega, r)$ approaches the same value for different $r/2r_d$ as Ω goes to zero. The function $f(K)$ is approximately constant for $r_\omega \approx r < r_d$.

At this point, it will be useful to obtain expressions for the absorption for the low and high frequency limits within this localized model. In the limit

of low frequencies, $\hbar\omega \ll e r_\omega E_N$ (i.e., $\Omega \ll e r_\omega E_N$), $F(\Omega, r)$ in Eqn. (2.16) can be used. When it is substituted into Eqn. (2.5) it gives [17],

$$\alpha(\omega) = \frac{4\pi^3}{6c} a \omega r_\omega^3 N_d^{4/3} Kf(K), \quad (2.18a)$$

where, the r in the integral is assumed to be constant since it varies slowly compared to the exponential function. Eqn. (2.18a) is derived for compact pairs with $a \ll r_\omega \ll r_d$ and $\Omega \approx 0$. The DDI cannot be neglected except for the case with a very low degree of compensation (i.e., Δ is small). Therefore, Eqn. (2.18a) is obtained only to within a factor depending on the frequency logarithmically (see Eqns. (2.10)) because it does not take into account dipole-dipole interactions. It should be emphasized that for the case of an intermediate compensation, Δ is of order of the impurity band. At very low frequencies, i.e., $(\Omega + e^2/\kappa r) \ll \Delta$, the form of the function $F(\Omega, r)$ in Eqn. (2.9c) is not suitable; instead, $F(\Omega, r) \propto (\Omega + e^2/\kappa r)^5$ in Eqn. (2.9d) should be used. In this case, the absorption at the limit of low frequencies, $\hbar\omega \ll e^2/\kappa r_\omega \ll \Delta$, is given by the following [17, 23],

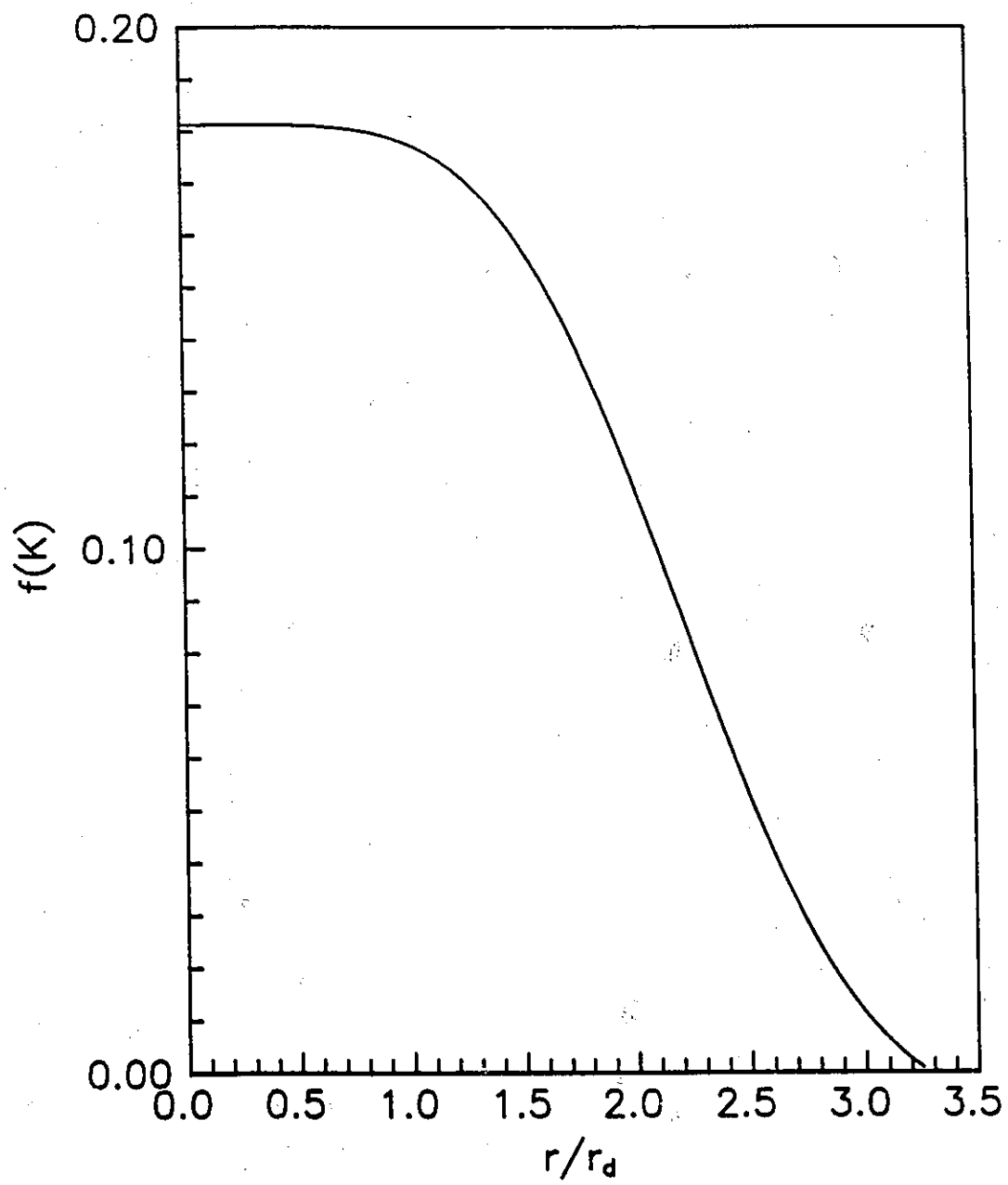
$$\alpha(\omega) \propto \frac{\omega}{r_\omega} \propto \frac{\omega}{\ln(2I_0/\hbar\omega)}, \quad (2.18b)$$

where, $r_\omega \propto \ln(2I_0/\hbar\omega)$ is assumed (see Eqn. (2.7)). Hence, the dependence of absorption on frequency in Eqn. (2.18b) is stronger than linear.

In the limit of high frequencies, $\hbar\omega \gg e r_\omega E_N$, one has to take into account that $F(\Omega, r)$ decreases steeply as Ω increases for $\Omega \gg e r_\omega E_N$. Then the main contribution to the integral in Eqn. (2.5) comes from a narrow interval near $r \approx r_\omega$, where $\Omega \approx e r_\omega E_N \ll \hbar\omega$. In this case, the function $r^4 F(\Omega, r)$ in the integral is assumed constant for $\Omega \leq e r_\omega E_N$ and zero otherwise. Then it gives [17],

$$\alpha(\omega) \approx \frac{4\pi^3 e^2}{3c \hbar \kappa} a r_\omega^4 N_d^2 Kf(K). \quad (2.19)$$

Figure 2.3 The function $f(K)$ plotted against r/r_d as $\Omega \rightarrow 0$.



At low frequencies, $\hbar\omega < e r_\omega E_N$, only pairs with $\Omega \leq \hbar\omega$ will participate in the absorption. Therefore, the absorption increases with increasing frequency. However, at high frequencies, $\hbar\omega > e r_\omega E_N$, the contribution is from $\Omega < e r_\omega E_N$, where r_ω decreases with increasing frequency. It follows from the above analysis that $\alpha(\omega)$ has a maximum at [17],

$$\hbar\omega_{\max} \approx e r_\omega E_N = \frac{e^2 N_d^{2/3}}{\kappa} r_\omega. \quad (2.20)$$

2.4 THEORETICAL ABSORPTION FOR N-TYPE SI

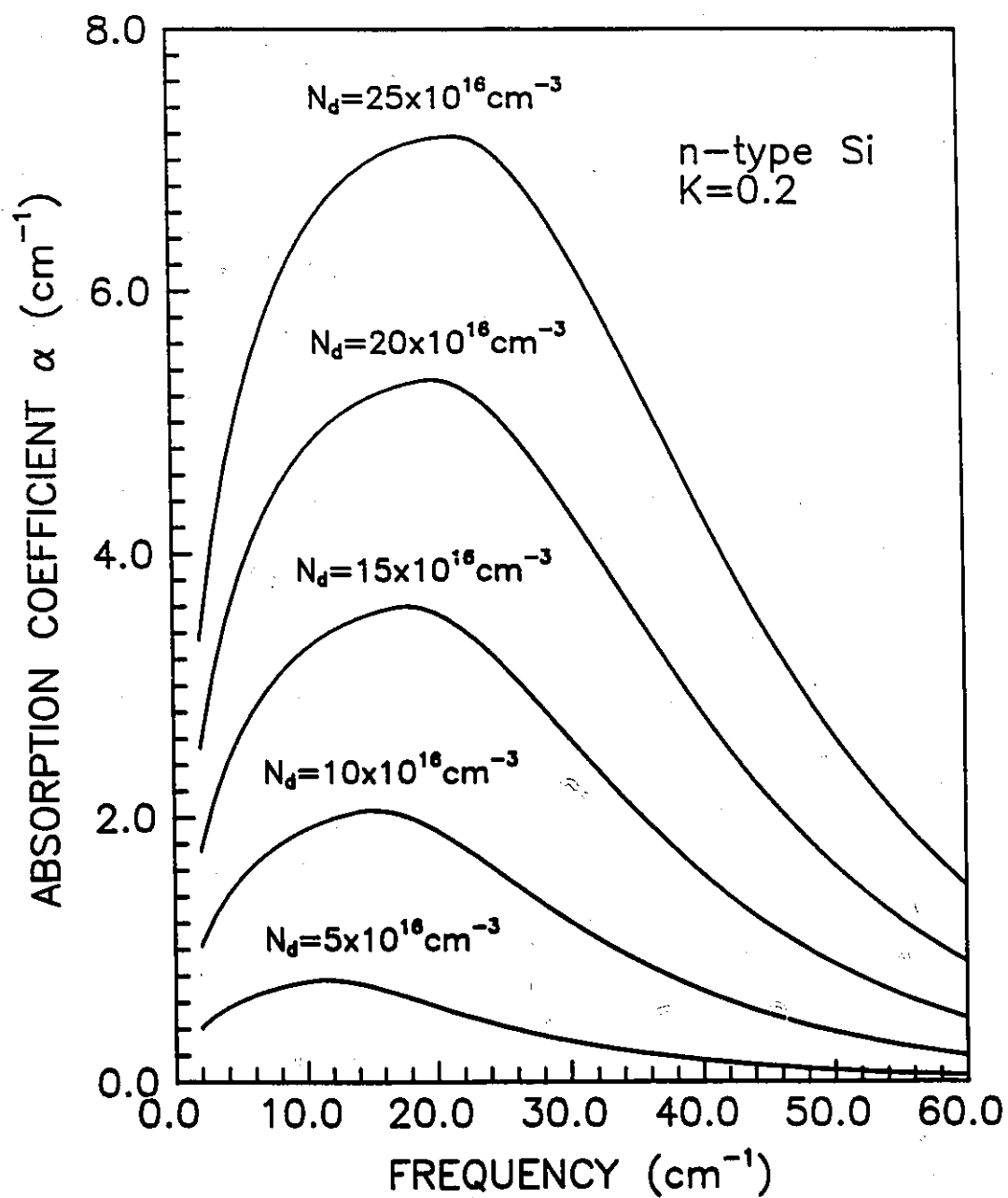
In order to illustrate the general character of the predicted absorption spectrum, numerical calculations of the absorption spectra of compensated n-type Si were carried out using Eqn. (2.5) at $T=0$. The functions $I(r)$ and $F(\Omega, r)$ in Eqns. (2.6) and (2.13) were used to perform these calculations. The $I(r)$ in Eqn. (2.6) is the angular average of $I(r, \vartheta)$ which is anisotropic in Si. The localization radius, a , is 19.3 Å, and I_0 is obtained from the following expression [14]:

$$I_0 = \frac{e^2}{3\pi a} \left(\frac{4\pi}{\eta n_0^2} \right)^{1/4}. \quad (2.21)$$

A parameter η , the index of refraction n , and the number of valleys n_0 have the values 4.2, 3.42, and 6 respectively for Si [16]. Using these values, I_0 is found to be 92.08 cm^{-1} . The numerically calculated spectra for various donor concentrations ($N_d = 5, 10, 15, 20, 25 \times 10^{16} \text{ cm}^{-3}$) with compensation $K=0.2$ are plotted in Fig. 2.4.

These theoretical absorption spectra show that the absorption starts at very low frequencies and extends to frequencies in excess of 60 cm^{-1} . It is clear that the absorption increases with increased impurity concentration. This can be explained within this localized model by recognizing that the

Figure 2.4 The predicted absorption spectra for n-type Si with compensation $K=0.2$ at various doping concentrations.

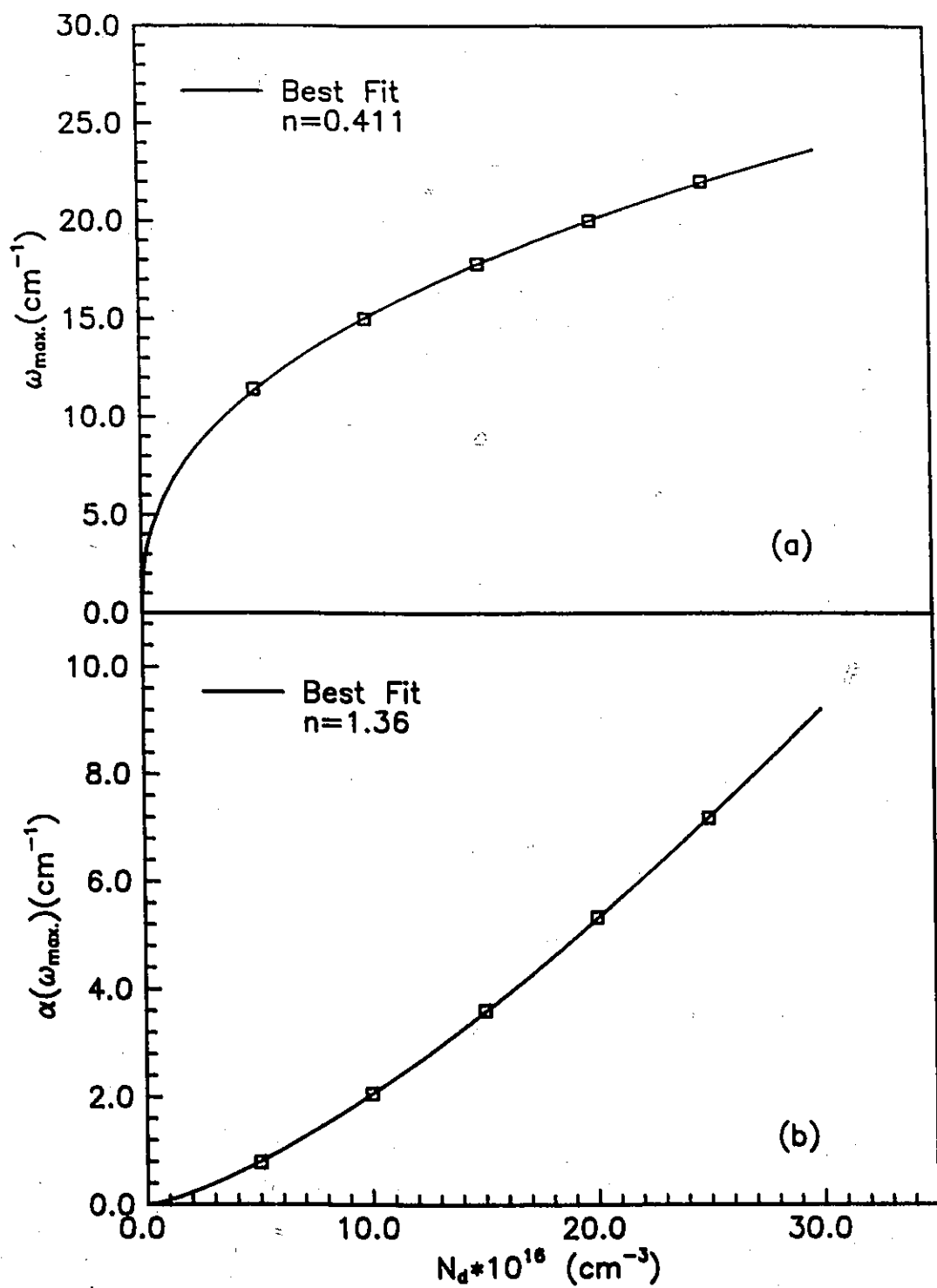


increasing absorption is due to the increasing number of pairs. If only the homopolar pairs contribute to the absorption process (i.e., Ω is small), then $rF(\Omega, r)$ is a constant for $r < r_d$ as shown in Fig. 2.3. In this case, the shape of the absorption should not depend on the concentration and there should not be such a rapid drop at high frequencies. However, it is clear that this is not the case. This localized model demonstrates that the polar pairs also make significant contributions. The frequency of maximum absorption shifts to higher frequencies with increasing N_d . This is due to the fact that the Coulomb potential difference of the ionized minority impurity at the positions of the two centers of the majority pair increases. As is shown in Fig. 2.2, $rF(\Omega, r)$ decreases steeply only when $\Omega > e r E_N = (e^2 \kappa) r N_d^{2/3}$. Hence, if N_d increases, the number of pairs with higher Ω increases. At high frequency, the absorption drops mainly because the number of polar pairs with small separations, r , and high potential differences, Ω , is low.

Figure 2.5 shows the frequency at the maximum plotted against N_d . It is found that ω_{\max} is proportional to $N_d^{0.4}$. The dependence of the maximum of the absorption spectrum on N_d is proportional to $N_d^{1.36}$. The character of the absorption maximum is clearly dependent on the function $F(\Omega, r)$; however, it is also influenced by the form of the energy overlap integral $I(r)$.

The n-type Si infrared absorption spectra for frequencies above 10 cm^{-1} have been experimentally measured by Milward and Neuringer [2]. Some quantitative agreement between theoretical and experimental results for compensation samples for frequencies $10 \text{ cm}^{-1} \leq \omega \leq \omega_{\max}$ has been demonstrated. However, for $\omega > \omega_{\max}$ the agreement is poor. The calculated absorption is less than the observed one. It should be noted that the separation r_ω , at $\omega = \omega_{\max}$, varies from $3.8a$ to $2.9a$ for samples with ω_{\max}

Figure 2.5 (a) Maximum absorption frequency for various doping concentrations. The data points are obtained from Fig. 2.4. The solid curve represents the power curve fit ($y = ax^n$) to the data with $n = 0.4$. (b) Value of the maximum absorption as function of doping concentration. The solid curve represents the power curve fit to the data with $n = 1.36$.



ranging from 11.4 to 22 cm^{-1} as shown in Fig. 2.4. It is clear that at these frequencies the condition $r_0 \gg a$ is violated. Eqn. (2.6) describing $I(r)$ cannot be used and the quantum mechanical calculation of the energy levels of an electron in the potential of two charged donors is necessary. It should also be noted that ϵ_d varies from 36.6 and 62.5 cm^{-1} for samples with concentrations ranging from 5×10^{16} to $25 \times 10^{16} \text{ cm}^{-3}$. It is clear that at high frequencies the condition $\hbar\omega \ll \epsilon_d$ is also violated and the quantum effect on the function $F(\Omega, r)$ cannot be ignored.

2.5 ABSORPTION THEORY FOR P-TYPE MATERIALS

It is known that the low-frequency ac impurity conduction at low temperatures in p-type materials is similar to that in n-type materials. However, previous experimental data showing the far-infrared spectra of p-type Ge differ appreciably from those of n-type Ge. The differences are as follows [8]: (i) The maximum value of the absorption coefficient of p-type Ge is much higher than that for n-type Ge, (ii) the maximum of the absorption coefficient for p-type Ge occurs at higher frequencies than that of n-type Ge, and (iii) the dependence of the absorption coefficient on frequency for p-type Ge is not as strong as that of n-type materials.

In order to explain these differences, E. Kaczmarek and Z. W. Gortel [8] used the envelope functions introduced by Schechter [24] (see Appendix A) to describe the isolated-acceptor ground state rather than using the well-known hydrogen-like envelope function. The latter picture is qualitatively similar to that for n-type materials in which the donor ground state is described by the hydrogen-like functions with an anisotropic exponent. The basic difference between the two pictures is that the Schechter function in

p-type materials will give the four lowest two-center states formed by the ground states of the two impurities [25]; while there are only two in the latter case. All of these four states have different energies and should be taken into account when calculating the low-temperature absorption coefficient in the infrared.

The reason that the use of the Schechter envelope functions is essential in calculating the absorption coefficients for p-type materials has been pointed out by Gortel *et al* [26]. It can be shown that if the dominant contribution to the absorption is due to the polar pairs, then the results from a hydrogen-like approximation would agree qualitatively with the results from the model based on the Schechter envelope functions. In fact, this conclusion explains the similarities of ac impurity conductivity in both n- and p-type materials because the dominant contribution to the hopping conductivity is from those polar pairs. However, for the contribution from the homopolar pairs [26] the results of these two models are different both qualitatively and quantitatively. It was stated earlier that the homopolar pairs give an important contribution to the far-infrared absorption processes. Therefore, the use of the hydrogen-like approximation is not appropriate here.

With the Schechter wavefunction for an isolated acceptor, the interaction between two acceptors gives four lowest doubly degenerate two-center states instead of the two given in Eqn. (2.1). Their energies are given by the following equations:

$$\epsilon_{1,4} = -J + (S + \sqrt{BA_5^1})I_1 \pm \Gamma_1, \quad (2.22a)$$

$$\epsilon_{2,3} = -J + (S - \sqrt{BA_5^1})I_2 \pm \Gamma_2, \quad (2.22b)$$

where,

$$\Gamma_1^2 = I_1^2 + \frac{1}{4}\Omega^2[1 - (S + \sqrt{BA_5^1})^2], \quad (2.23a)$$

$$\Gamma_2^2 = I_2^2 + \frac{1}{4}\Omega^2[1 - (S - \sqrt{BA_5^1})^2]. \quad (2.23b)$$

I_1 and I_2 are the energy overlap integrals given by,

$$I_1 = (L + \sqrt{BA_5^2}) - J(S + \sqrt{BA_5^1}), \quad (2.24a)$$

$$I_2 = (L - \sqrt{BA_5^2}) - J(S - \sqrt{BA_5^1}), \quad (2.24b)$$

and,

$$S = c_1^2 A_1^1 + c_2^2 A_2^1 + c_3^2 A_3^1 + (c_3^2 - 3c_2^2)(l^2 m^2 + l^2 n^2 + n^2 m^2) A_4^1, \quad (2.25a)$$

$$L = c_1^2 A_1^2 + c_2^2 A_2^2 + c_3^2 A_3^2 + (c_3^2 - 3c_2^2)(l^2 m^2 + l^2 n^2 + n^2 m^2) A_4^2, \quad (2.25b)$$

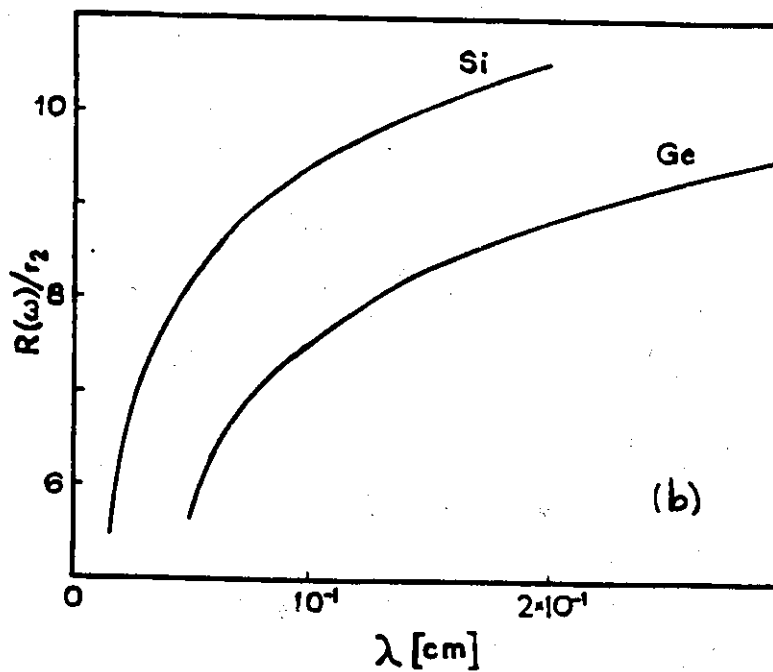
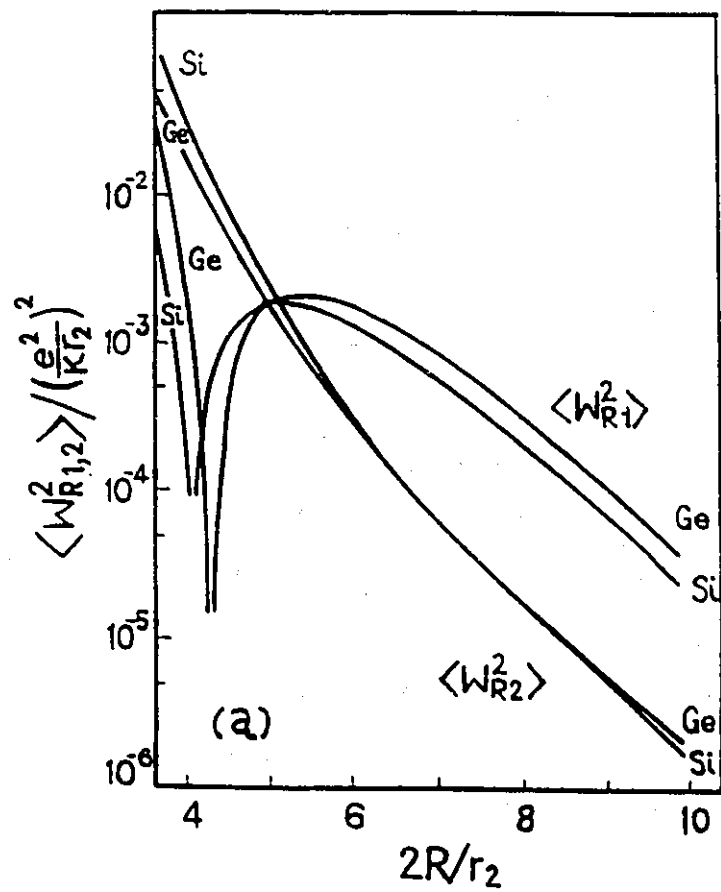
$$J = (\varphi_1 + \varphi_2)/2, \quad (2.25c)$$

$$B = \frac{1}{4}c_1^2 \{c_2^2[(3n^2 - 1)^2 + 3(l^2 - m^2)^2] + 4c_3^2(l^2 m^2 + l^2 n^2 + m^2 n^2)\}. \quad (2.25d)$$

where l , m , and n are the cosines of the angles between the pair and $[100]$, $[010]$, and $[001]$ crystal directions, respectively. The explicit expressions for the function $A_\nu^\lambda(r)$ ($\nu = 1, 2, 3, 4, 5$ and $\lambda = 1, 2, 3$) can be found in papers by E. Kaczmarek [25]. The quantities c_1 , c_2 and c_3 (see Appendix A) are the variation parameters of the Schechter functions; the remaining two variation parameters of the envelope functions r_1 and r_2 , are contained in the $A_\nu^\lambda(r)$ functions.

The dependence of $\langle I_1^2 \rangle$ and $\langle I_2^2 \rangle$ on $2r$ is plotted in Fig. 2.6a. The behavior of I_1 is qualitatively different from that of the hydrogen-like case as described by Eqn. (2.6). The difference is due to the presence of the d-like contributions in the Schechter envelope functions. This leads to energy

Figure 2.6 (a) Dependence of the angular averages of the squares of the energy overlap integrals $\langle W_{R1}^2 \rangle$ and $\langle W_{R2}^2 \rangle$ (i.e., $\langle I_1^2 \rangle$ and $\langle I_2^2 \rangle$ in the text) on the pair separations, $2R$, for p-type Ge and Si (in arbitrary units). (b) Dependence of $R(\omega)$ (i.e., r_ω in the text) on the wavelength of radiation for p-type Ge and Si. Both figures are obtained from the work of E. Kaczmarek *et al.* [8].



differences between the two-center states nonmonotonically dependent on a pair separation r as shown in Fig. 2.6a. Neglecting these contributions gives $I_1 = I_2$, as in the hydrogen-like case. Although the d-like contributions have a much smaller amplitude than the s-like parts, they can be important at some distances from the acceptor ion. If Ω is neglected, it is clear from this figure that the lowest energy state is ε_3 for the pairs with $r < \frac{5}{2}r_2$ and ε_4 for pairs with $r > \frac{5}{2}r_2$.

It can be shown that only transitions from the states ε_4 to ε_1 and from ε_3 to ε_2 contribute significantly to the total absorption. The remaining transitions are far less probable since their transition rates are of the fourth order in the overlap integrals. Taking the respective angular average values for I_1 and I_2 , the absorption coefficients α_{41} and α_{32} for these two transitions can be obtained from Eqn. (2.5). Taking into account the occupation of the initial states one obtains the total absorption coefficient,

$$\alpha(\omega) = f_4 \alpha_{41}(\omega) + f_3 \alpha_{32}(\omega), \quad (2.26)$$

where, f_4 and f_3 are the temperature-dependent occupation functions of the initial states ε_4 and ε_3 ,

$$f_4 = \frac{1}{\{1 + \exp[-(\varepsilon_3 - \varepsilon_4)/kT]\}}, \quad (2.27a)$$

$$f_3 = 1 - f_4. \quad (2.27b)$$

It is assumed that the temperature is so low that the higher final states ε_1 and ε_2 are always empty.

It is found that by using the Schechter envelope function, the photon-induced transition rate of a carrier is dominated by two terms [26]. The first

term has a form analogous to that of the n-type material. This term is proportional to the square of the overlap energy integral, which for a pair with a given separation, is larger for the p-type than for the n-type material. The second term which is absent in the hydrogen-like approximation, is even larger than the first term for some directions. Therefore, the much larger absorption in the p-type material is expected when the Schechter envelope function is used. Also, the larger value of the resonance energy can also explain the shift in the maximum of the absorption towards higher frequencies.

The theory also predicts a sharp absorption peak at 20.4 cm^{-1} . Its position does not depend on the compensation or on the concentration of acceptors. The shape and relative height of the peak is temperature independent [8]. The presence of the peak is a direct result of the peculiar behavior of the overlap energy integral $\langle I_1^2 \rangle$ as a function of the pair separation. Because of the slow variation of $\langle I_1^2 \rangle$ in the vicinity of its maximum value (see Fig. 2.6a), $\langle I_1^2 \rangle_{\text{max}}$, a large number of pairs can absorb radiation with the energy $\hbar\omega = 2(\langle I_1^2 \rangle_{\text{max}})^{1/2}$. Therefore, the position of this sharp peak is determined by $\hbar\omega = 2(\langle I_1^2 \rangle_{\text{max}})^{1/2}$. As mentioned earlier, the non-monotonicity of $\langle I_1^2 \rangle$ is caused by the presence of the d-like parts in the variational envelope functions for isolated acceptors.

Chapter 3

EXPERIMENTAL TECHNIQUES

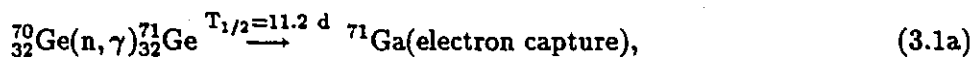
3.1 INTRODUCTION

The basic principle of p-type compensated NTD Ge will be first presented. The NTD Ge samples have extremely homogeneous distributions of dopants because the impurities are produced from isotopes of Ge which are evenly distributed throughout the sample. The impurity concentration of a sample can easily be controlled by the neutron irradiation time. The compensation ratio; however, remains constant. Hence, absorption experiments can be done on samples with different concentrations but fixed compensation. It is also possible to perform the time dependent absorption experiments on NTD Ge to investigate the absorption change due to the change of the majority impurity concentration at a fixed minority impurity concentration. The preparation and properties of the samples are described in section 3.3. The experimental apparatus used to make the FIR absorption measurements

is described in section 3.4. The method by which optical parameters of a sample, such as the absorption coefficient, are obtained from a transmission spectrum, is discussed in the final section 3.5.

3.2 PRINCIPLE OF NTD GE

The Ge samples were irradiated with thermal neutrons. Some of the five naturally occurring stable isotopes: ^{70}Ge , ^{72}Ge , ^{73}Ge , ^{74}Ge , and ^{76}Ge capture neutrons and become radioactive and subsequently decay into different chemical elements which are acceptor or donor impurities in Ge. The nuclear reactions of interest are [10]:



Three Ge isotopes, ^{70}Ge , ^{74}Ge , and ^{76}Ge participate in the doping process. The isotope, ^{70}Ge , captures a neutron (this capture is accompanied by γ radiation) and is transformed into the radioactive isotope ^{71}Ge , which subsequently decays into the acceptor ^{71}Ga by electron capture with a half-life of 11.2 days.

Two donor-impurities are also created: As and Se. The isotope ^{74}Ge is converted into the radioactive ^{75}Ge through a (n, γ) reaction. The ^{75}As is formed from the radioactive ^{75}Ge via β decay, with a half-life of 82.8 min. When ^{76}Ge captures a neutron, it becomes the radioactive ^{77}Ge which is then transformed by β decay into the unstable isotope ^{77}As which has a half-life

of 11.3 hrs.. This unstable isotope is then transformed into stable ^{77}Se by β decay with a half-life of 38.8 hrs..

The natural abundance, thermal neutron absorption cross sections, and half-lives of the relevant isotopes of Ge are listed in Table 3.1. The production rates of different impurities can be calculated from the data in this table. They are 2.9×10^{-2} and 0.6×10^{-2} (atoms/cm³)/(neutrons/cm²) for Ga and As respectively. The production rate of ^{77}Se is small compared to Ga and As. After a sufficiently long time, all the decay processes will have been exhausted, the ratio of the concentrations of the different dopants, i.e. the compensation (K), will be fixed by the thermal neutron capture cross section and natural abundance of the dopant-producing isotopes. According to the experimental results of Yu. A. Osipyan *et al.* [27], based on the time dependent Hall measurements, the relation of the concentrations of these impurities in NTD Ge is as follows:

$$N_{\text{Ga}} : N_{\text{As}} : N_{\text{Se}} = 1 : 0.26 : 0.012. \quad (3.2)$$

These results are in fair agreement with the theoretical results obtained using the reaction data in Table 3.1. Hence, the degree of compensation for the NTD Ge is ≈ 0.27 . This doping method allows us to investigate the absorption change of Ge samples due to the change of the impurity concentration with fixed compensation.

As a result of different decay half-lives, different impurities are formed at different rates. As, which is the dominant donor impurity, reaches its saturation value within a day after irradiation due to the short decay half-life (82.8 m) of ^{74}Ge . The Se donors also reach 80% of their saturated value

TABLE 3.1. List of the Natural Abundance, Cross Section and Half-life of Relevant Ge Isotopes. [28]

Isotope	Natural Abundance (%)	Cross Section (10^{-24} cm^2)	Half-life	Dopant Type
$^{70}_{32}\text{Ge}$	20.5	3.25	11.2 d (^{71}Ga)	p
$^{72}_{32}\text{Ge}$	27.4	1.0		
$^{73}_{32}\text{Ge}$	7.8	15		
$^{74}_{32}\text{Ge}$	36.5	0.36	82.8 m (^{75}As)	n
$^{76}_{32}\text{Ge}$	7.8	0.06	11.3 h (^{77}As)	
			38.8 h (^{77}Se)	n

about 5 days after irradiation. However, because of the longer decay half-life (11.2 d) of ^{71}Ge , the concentration of the acceptor impurity reaches the saturated value of N_d only after a time $t = t_0$ of the order of several days after the start of irradiation. The NTD Ge sample approaches total compensation (i.e., $K=1$) as t approaches t_0 . The NTD Ge, which is n-type for $t < t_0$, will convert to p-type at $t = t_0$. For $t > t_0$ the degree of compensation will decrease with time and approach asymptotically to the steady-state value of $K \approx 0.27$.

The concentration, $N(t)$, of a particular impurity concentration at time t after starting the irradiation can be calculated using the following expressions:

$$N(t) = N_0 \left\{ \frac{1}{t_r} \left[t - \frac{\tau}{\ln 2} (1 - \exp(-\frac{\ln 2}{\tau} \cdot t)) \right] \right\}, t \leq t_r \quad (3.3a)$$

$$N(t) = N_0 \left\{ 1 - \frac{\tau}{(\ln 2 \cdot t_r)} \left[\exp(-\frac{\ln 2 \cdot (t - t_r)}{\tau}) - \exp(-\frac{\ln 2}{\tau} \cdot t) \right] \right\}, t \geq t_r \quad (3.3b)$$

where, N_0 is the saturated concentration of an impurity long after irradiation, t_r is the time of neutron irradiation and τ is the decay half-life of an unstable

isotope as shown in Table 3.1. Fig. 3.1 illustrates the dynamic change of Ga and As impurity concentrations for samples that have been irradiated for 10 hrs. The compensation $K = N_o(\text{As})/N_o(\text{Ga}) = 0.286$ is assumed, and it is found that the sample goes through total compensation at $t = 5.65$ days after the start of the irradiation.

These decay properties of NTD Ge allow us to investigate the change in absorption due to the change in the majority impurity concentration while keeping the minority impurity concentration constant. This is done by performing time dependent absorption experiments after the donor impurities have reached their saturated value and the acceptors are still being formed.

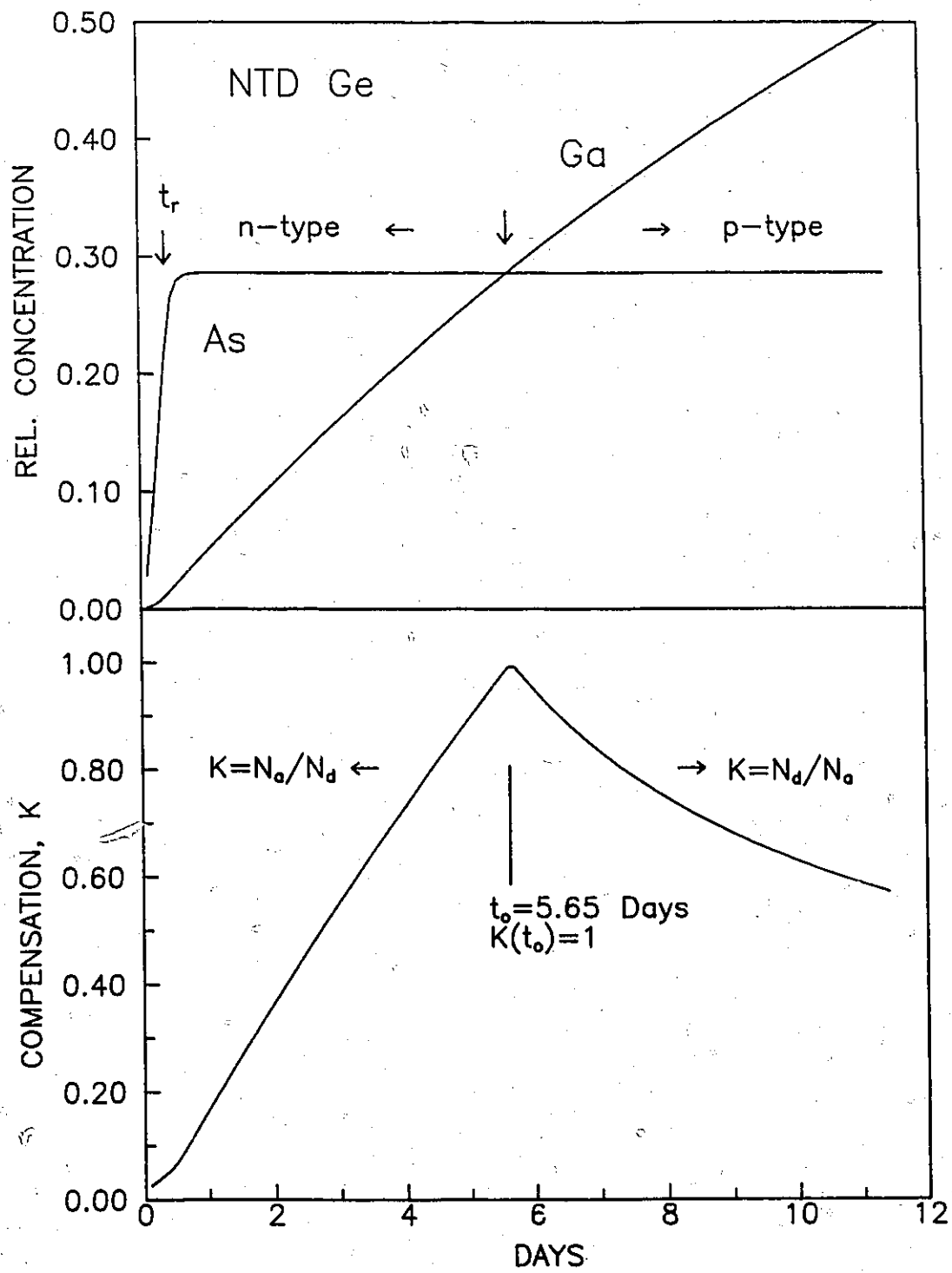
3.3 SAMPLE PREPARATION

The starting materials for the NTD Ge samples were single crystal low impurity n-type Ge wafers with $(N_d - N_a) < 10^{12} \text{ cm}^{-3}$ with thicknesses of about 0.05 cm. These wafers were cut into pieces of $1 \times 1 \text{ cm}^2$ in size. They were then irradiated with thermal neutrons at approximately 35°C [29] in the McMaster Nuclear Reactor (MNR). The thermal neutron flux (ϕ) at the position of irradiation was $\approx 1.4 \times 10^{13} \text{ n}/(\text{cm}^2 \cdot \text{sec})$ [29] with a ratio of thermal neutrons to neutrons with energy greater than 0.5 eV of approximately 40 : 1.

Seven samples, S1 to S7, were irradiated for different time intervals varying from one to twenty hours. The production of various impurities is proportional to neutron fluence. The concentration of impurity i , N_i can be estimated from the following expression [29]:

$$N_i = \sigma_{i(\text{effective})} \cdot (P_i \cdot N_{\text{Ge}}) \cdot \phi \cdot t, \quad (3.4a)$$

Figure 3.1 Time evolution of different impurities in NTD Ge. The time $t=0$ is set as the beginning of the neutron irradiation. (a). The relative concentrations of Ga and As are shown. (b). The compensation of the sample is shown. Notice that at $t = t_0$, the concentrations of Ga and As are equal. Before that the sample is n-type, after that the sample is p-type.



where, $\sigma_{i(\text{effective})}$ is the effective neutron capture cross section, p_i is the natural abundance of a particular isotope, N_{Ge} is the atomic density of Ge and t is the time of irradiation. The effective neutron capture cross section, $\sigma_{i(\text{effective})}$, can be obtained from the following expression [29]:

$$\sigma_{i(\text{effective})} = \frac{2}{\sqrt{\pi}}\sigma_i + 7.58 \times 10^{-3}\sigma_i + \frac{[\text{R.I.}]}{48.95}, \quad (3.4b)$$

where σ_i is the neutron capture cross section for impurity i with energy $E_0 = 0.0253$ eV (corresponding to a neutron velocity of 2200 m/s or a temperature of 20°C). The first and second terms in Eq. (3.4b) are due to neutron capture in the thermal and epi-thermal ($0.15\text{eV} < E < 0.5\text{eV}$) regions. The third term is due to resonance capture in the epi-thermal region. Here [R. I.] denotes the Resonance Integral which is found to be 1.5 b (10^{-24} cm²) [30] for ^{70}Ge . Ignoring the small temperature correction and using Eqns. (3.4a) and (3.4b) and data in Table 3.1, the concentration of the Ga impurities is estimated to vary from 1.88×10^{15} cm⁻³ to 3.65×10^{16} cm⁻³ for these NTD Ge samples, as shown in Table 3.2. These samples, all of which have the same compensation ratio long after the irradiation, were used for absorption experiments which investigated the change in absorption with changing concentration.

Except for the sample which is used for the time dependent absorption experiment, samples are kept for more than three months after irradiation before they are used for the absorption experiments. The samples are thinned using 600-grit SiC paper. Opposite surfaces of the samples are made parallel. Both surfaces are mechanically polished using 6 μm and then 1 μm diamond grit paste. The thickness of the samples was determined using a micrometer with an uncertainty of $\pm 0.005\text{mm}$ (see Table 3.2).

Radiation damage of the samples was removed by thermally annealing at 400 °C for six hours in a pure argon atmosphere [10]. All samples were placed into the furnace at a temperature below 100 °C and were taken out only after the furnace had cooled to room temperature.

The square samples were characterized by Hall effect measurements using the usual van der Pauw configuration [31] with magnetic fields of approximately 1 KG. Ohmic contacts were made by alloying indium to the four corners of the samples. This was done by heating with a low powered soldering gun. The room temperature transport properties of samples S1-S7 are shown in Table 3.3. The carrier concentrations, $n = (N_a - N_d)$, and mobility, μ , were calculated from $n = r_H/R_{HE}$, and $\mu = R_H/r_H\rho$ [32]. The Hall coefficient, R_H , and resistivity, ρ , were obtained from the measurements. The Hall factor, r_H , in the weak field limit was found experimentally to be ≈ 1.8 by Morin [33]. The present data is in agreement with the existing transport properties of p-type Ge [34]. The results of the time dependent electrical measurement which will be discussed in Chapter 4 show that the compensation of these samples is 0.286. Hence, the acceptor concentrations, N_a , for these samples are calculated using this value. A comparison of these values of N_a with the Ga concentrations estimated from the nuclear reactions in Table 3.2 shows good agreement. Thus, it can be concluded that Ga is the largest majority impurity in these samples.

Sample S5 is used for the time dependent absorption experiment. This sample was annealed three days after the start of the irradiation using the same procedure as described above. The waiting period is necessary because the total activity of the sample must be below 15 mCi [35] before it can be handled safely. The annealing done at this early stage does not

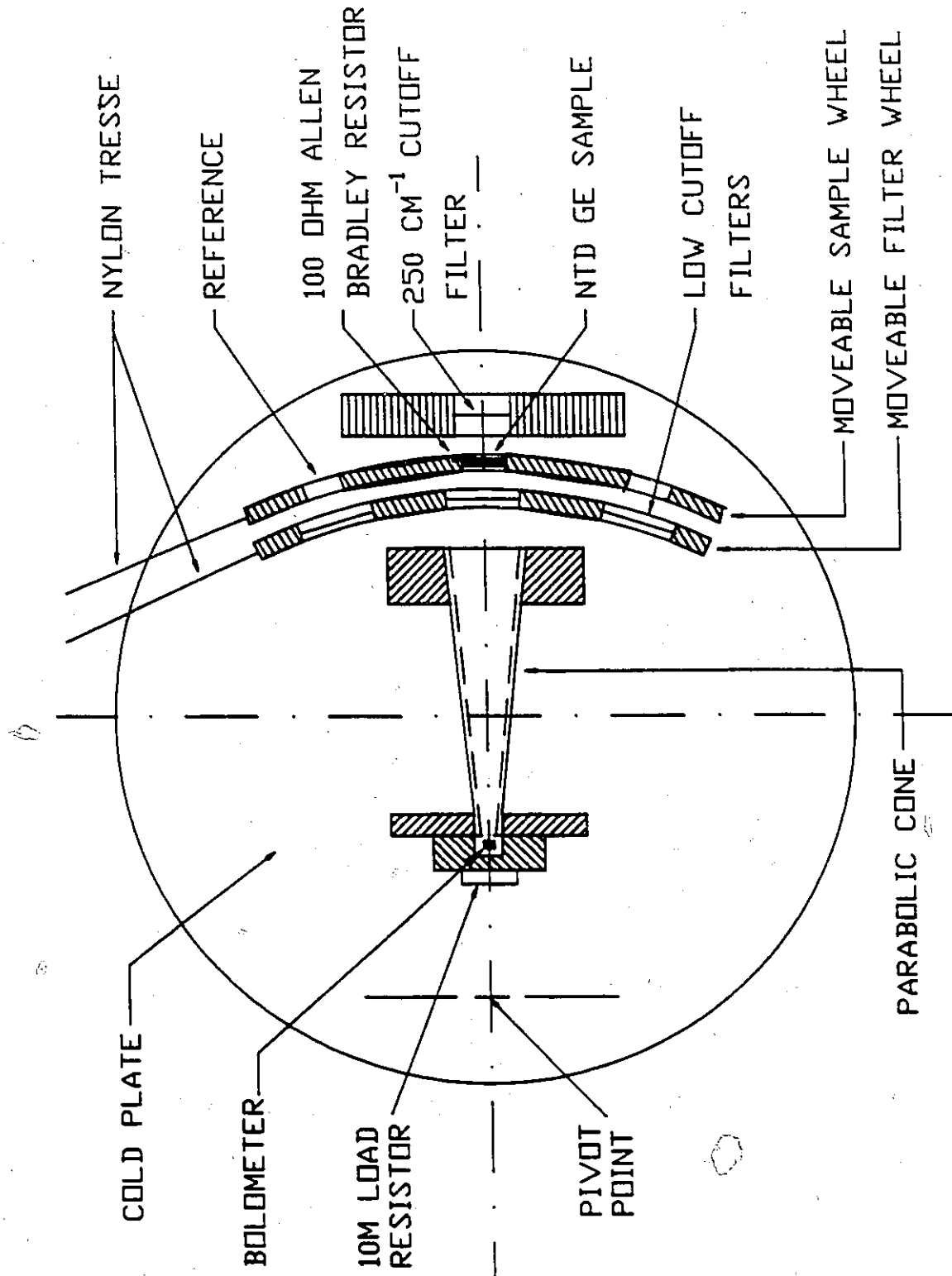
TABLE 3.2. Physical Data for NTD Ge Samples

Sample	Irradiation Time (hrs.)	Fluence (10^{17}cm^{-2})	Ga Concentration (10^{15}cm^{-3})	Thickness (mm)
S1	1	0.5	1.7	0.475
S2	2	1.0	3.4	0.490
S3	4	2.0	6.8	0.440
S4	8	4.0	14	0.469
S5	10	5.0	17	0.499
S6	16	8.1	27	0.489
S7	20	10	34	0.366

TABLE 3.3. Hall Measurement Data for NTD Ge Samples

Sample	Resistivity ($\Omega\text{ cm}$)	Hall Mobility ($\text{cm}^2/\text{V sec}$)	($N_a - N_d$) (10^{15}cm^{-3})	N_a (10^{15}cm^{-3})
S1	2.53	1840	1.34	1.88
S2	1.54	1740	2.32	3.25
S3	0.823	1520	4.97	6.96
S4	0.458	1370	9.92	13.9
S5	0.335	1200	15.5	21.7
S6	0.286	1150	19.1	26.7
S7	0.223	1080	26.1	36.5

Figure 3.2 Top view of the arrangement in the cold working surface of the cryostat. The moveable wheels can be rotated around the pivot point. The wheels are positioned from outside the dewar by adjusting the nylon tresse attached to one end of the wheel. The other end is attached to a spring.



affect the quality of the sample as shown by its high Hall hole mobility. This is in agreement with previous results [36] which indicate that the formation of defects is mainly due to the radiation damage which can be removed by annealing.

3.4 THE FIR TRANSMISSION EXPERIMENTS

The transmission experiments in the far-infrared are done using Fourier Transform Spectroscopy. A custom built polarizing interferometer (C. Zárate, unpublished) with roof mirrors, a wire grid beam-splitter, and a chopper frequency of 45 Hz was used. The light source was a fused quartz mercury-arc lamp. The FIR light passes through a polypropylene window into the cryostat.

A cryostat manufactured by Infrared Laboratories Inc. [†] with a composite type Si bolometer with an operating temperature of approximately 1.25 K was used. The details of the set up in the cryostat are shown in Fig. 3.2. It shows two moveable wheels operating inside the cold working surface of the cryostat. One of them is used to hold different cold cutoff filters so that they can be changed during the experiment. The other is to hold the sample and the reference. The light that passes through the filter and sample is then collected by a parabolic cone which condenses the light onto the bolometer.

Two stages are involved in filtering the light. Before reaching the sample, the radiation passes through a cold filter made of thick black polyethylene melted to a piece of grey plastic from the lid of a Kodak film canister was put in front of the sample. Its cutoff is approximately 250 cm^{-1} . Both

[†] HD-3(L) dewar, Infrared Laboratories, Tucson, AZ., U. S. A..

excess sample heating and band-edge light were prevented from reaching the sample by using this filter. Second, the radiation passes through one of three cold low pass filters located in the filter wheel before reaching the bolometer. These filters define the cutoff energy of the spectra. They are 0.125 in. thick Pyrex glass, 0.08 in. thick Fluorogold and 0.0625 in. thick quartz with cutoff frequencies of 30, 50, and 120 cm^{-1} respectively. A 0.25 in. thick Pyrex warm filter, which is placed outside the cryostat, was also used in conjunction with the cold filters for spectra with a cutoff of about 15 cm^{-1} . The transmission spectra presented here are obtained by linking spectra with different cutoff filters. All spectra were taken with a resolution of approximately 0.8 cm^{-1} .

The samples are glued to the sample holder by applying a small spot of GE 7031 varnish at one corner of the sample. The sample is placed over a 5 mm diameter opening in the sample holder. An opening with the same diameter as in the sample holder is used as a reference. The temperature of the sample is monitored using a 100 Ohm Allen Bradley resistor placed in thermal contact with the sample. All spectra were taken with the sample temperature at about 3 K.

3.5 DERIVATION OF THE OPTICAL PARAMETERS

The transmittance of a material is determined by its index of refraction, $N = n + ik$. This index, in general, must be complex to account for the absorption within the material. The raw transmittance spectra show strong Fabry-Perot fringes which have to be removed. Following the work of C.M. Randall and R.D. Rawcliffe [37], the external transmission, $T(\nu)$, of a parallel flat-surfaced sample with thickness d , at the wavenumber, ν , can be

expressed as follows:

$$T(\nu) = \tau(\nu) \left(1 + 2 \sum_{l=1}^{\infty} \rho^l \cos(l\theta) \right). \quad (3.5a)$$

A more familiar form is,

$$T(\nu) = \tau(\nu) \frac{(1 - \rho^2)}{(1 + \rho^2 - 2\rho \cos\theta)}. \quad (3.5b)$$

In these expressions,

$$\begin{aligned} \tau(\nu) &= |4N/(N+1)^2|^2 \exp(-\alpha d \cos\beta) / (1 - \rho^2), \\ &= 16(n^2 + k^2) \exp(-\alpha d \cos\beta) / \{[(n+1)^2 + k^2]^2 (1 - \rho^2)\}, \end{aligned} \quad (3.6a)$$

$$\rho = [(n-1)^2 + k^2] \exp(-\alpha d \cos\beta) / [(n+1)^2 + k^2], \quad (3.6b)$$

$$\theta = 4\pi n d \nu \cos\beta + \delta = 4\pi n d \nu \cos\beta + \tan^{-1}[2k/(n^2 + k^2 - 1)], \quad (3.6c)$$

$$\alpha = 4\pi k \nu, \quad (3.6d)$$

where, α is the absorption coefficient, τ is the average transmittance if there are no fringes, δ is the phase shift in reflectance at the surface caused by the imaginary part of the refractive index, ρ is the fraction of the energy which survives two reflections and two transmittances through the body of the sample, and β is the angle of incidence of the radiation. In these experiments, β is assumed to be zero.

In order to evaluate the absorption coefficient of a sample, the refractive index n will first be found from the interference fringes of the transmission spectrum. Since δ is small in these samples and can be neglected as a first approximation, it follows from Eqn. (3.5a) or (3.5b) that the transmittance maximum occurs at,

$$\theta = 4\pi n d \nu = 2\pi m \quad (3.7)$$

where, m is an integer that is of the order of the interference maximum at frequency ν . Since the transmittance is measured down to 4 or 5 cm^{-1} , the value for m is known and the refractive index can be obtained from the maximum of the transmission spectrum according to Eqn. (3.7).

According to the treatment of S. Zwerdling and J. P. Theriault [5], if α and n are essentially constant over the spectral range of one cycle of the interference, the absorption coefficients can be obtained from the average transmittance τ . It can be shown using Eqn. (3.5b) that τ can be obtained from the geometric mean of the maximum and minimum values.

However, since the resolution of the transmission spectra is chosen to be about 0.8 cm^{-1} , only the first signature of the fringes is significant in the interferogram. This implies that only the first cosine term of the series in Eqn. (3.5a) is important. That is, the observed transmission spectrum is given by,

$$T(\nu) = \tau(\nu)(1 + 2 \cdot C \cdot \rho \cos(\theta)), \quad (3.8)$$

where, a parameter, C , is put in front of the cosine term because an apodization function [38] is used before an interferogram is Fourier transformed into a frequency spectrum. In this case, the average transmittance should be the average value of the maximum and minimum values at the frequency corresponding to the average of their frequencies.

The absorption coefficient, α , can be found from the following relationship which is derived from Eqn. 3.6a with β set to zero:

$$\alpha = \frac{1}{d} \ln \left\{ \frac{(1-R)^2 A}{2 \cdot \tau} + \left[\left(\frac{(1-R)^2 A}{2 \cdot \tau} \right)^2 + R^2 \right]^{1/2} \right\}, \quad (3.9)$$

where, $A = (1 + k^2/n^2)$ and

$$R = \frac{(n-1)^2 + k^2}{(n+1)^2 + k^2} \quad (3.10)$$

is the reflectance at a single surface.

The process of finding the absorption coefficient, α , involves an iteration by a computer one frequency at a time. Since k is small compared to n , it is first approximated equal to zero at the initial frequency. $\tau(\nu)$, as described above, is determined from the experimental transmission spectrum by taking the average value of the maximum and minimum values of the fringes observed in the spectrum at the frequency corresponding to the average of their frequencies. The value α is obtained from Eqn. (3.9) and then a non-zero k is found. This process is repeated until the right and left hand sides of Eqn. (3.9) are equal to within $\pm 0.00001\%$. This α will be used as the initial approximation for the next frequency $(\nu + \delta\nu)$.

Once the absorption spectrum is obtained using this procedure, the transmittance is calculated using Eqn. (3.8). The original experimental spectrum will be compared with the calculated one with an appropriate choice of the adjustable parameter C in front of the cosine term. In general, at this stage, the constant parameter C is well fitted to a wide region of frequencies with no large discrepancies between the calculated and experimental transmission spectra. However, the above procedure will smooth a region with a sudden change in absorption or with sharp absorption peaks. In order to obtain a more detailed absorption spectrum at such regions, the experimental transmittance spectrum with the interference fringes will be fitted using Eqn. (3.8) to find a new $\alpha(\nu)$. To a first order approximation, the parameter C is assumed to be constant over the small frequency region which is being fitted. This parameter C is chosen such that the fringe structure is minimized in the resulting absorption spectrum. Then, this value of C combined with Eqn. (3.8) is used to least-squares fit the experimental transmittance

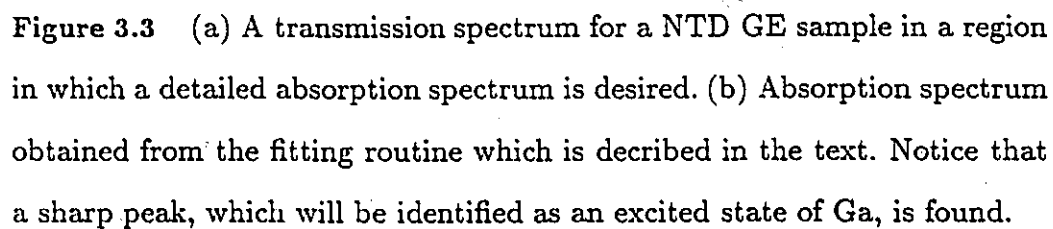
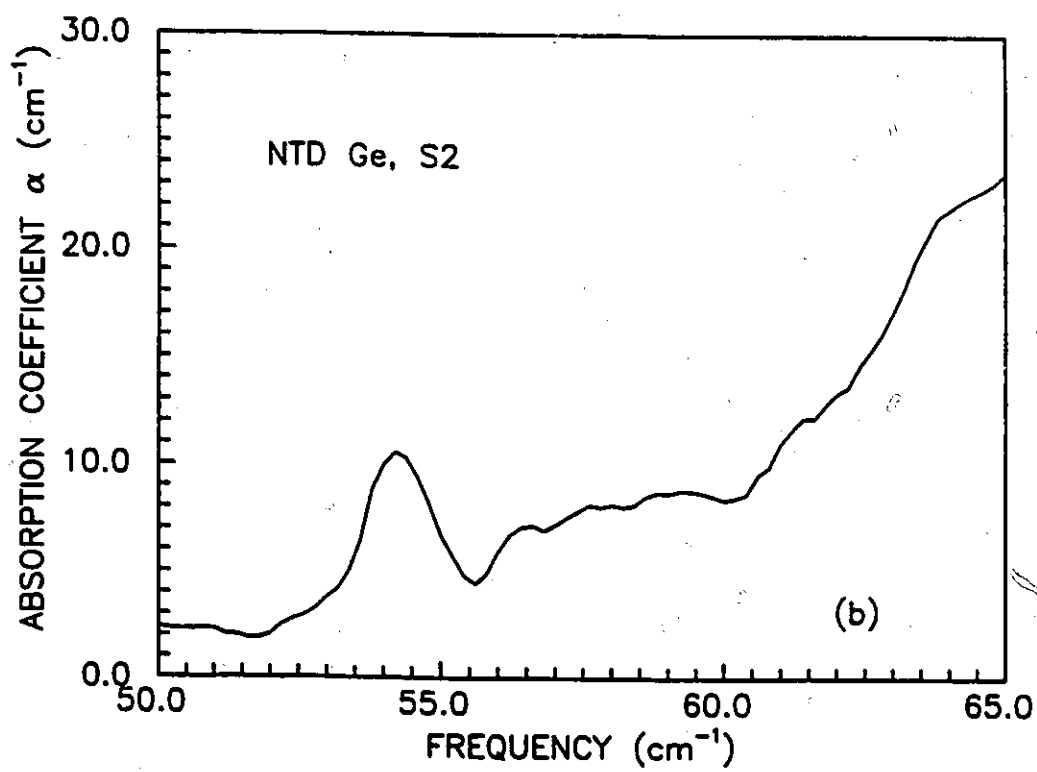
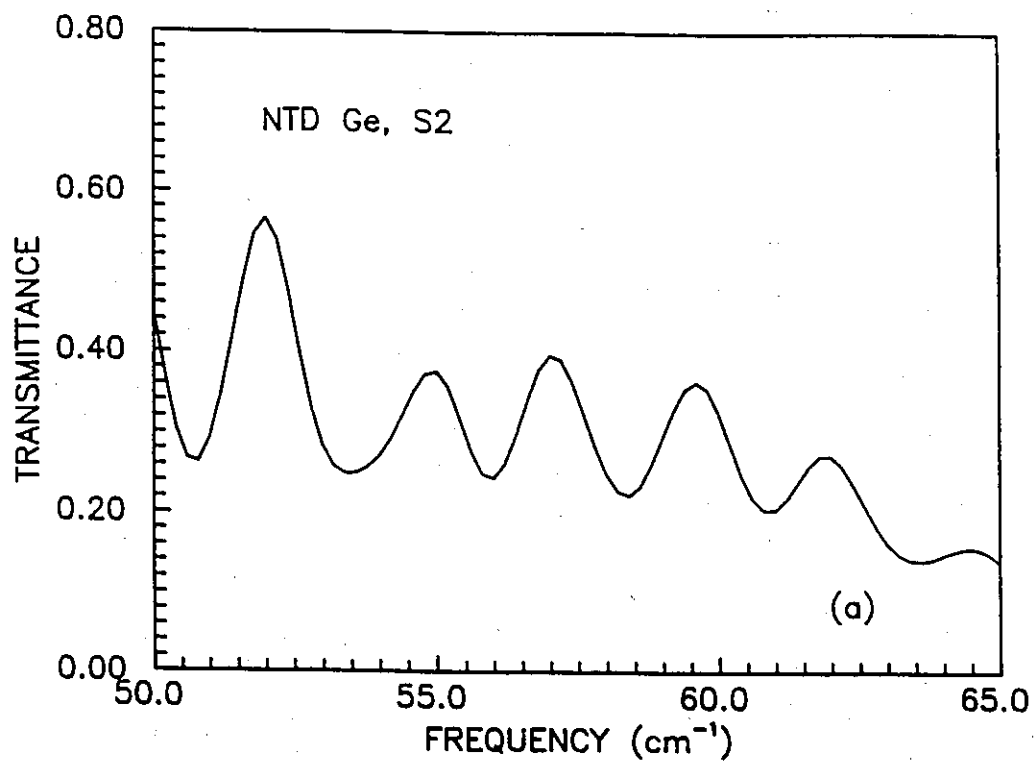


Figure 3.3 (a) A transmission spectrum for a NTD GE sample in a region in which a detailed absorption spectrum is desired. (b) Absorption spectrum obtained from the fitting routine which is described in the text. Notice that a sharp peak, which will be identified as an excited state of Ga, is found.



(with fringes) to find a new $\alpha(\nu)$. The value of $\alpha(\nu)$ derived from the average transmittance is used as a first guess. This procedure gives a more precise value of $\alpha(\nu)$ which ensures that sharp peaks are not missed. For instance, the sharp absorption lines resulting from the excited states of an impurity in the region above 40 cm^{-1} can be found in this manner. This is illustrated in Fig. 3.3.

Chapter 4

RESULTS AND DISCUSSION

4.1 INTRODUCTION

In this chapter, the results of the far-infrared absorption experiments are presented. The results for samples with different neutron irradiations (i.e. different impurity concentrations but the same compensation ratio) will first be presented. These absorption spectra will be compared to the presented theories and previous NTD Ge results. The change of the absorption coefficient due to the increased number of impurities while the compensation ratio remains fixed will also be discussed. The time dependent absorption spectra for sample S5 will be presented in section 4.3. In these spectra, the change of the absorption coefficient due to the increase in the majority impurity with fixed minority impurity concentration is obtained. In addition, the differences in the dependence of the majority concentration between these two series of absorption spectra will be discussed.

4.2 ABSORPTION SPECTRA FOR NTD GE

Figure 4.1 shows the transmission spectra for samples S1-S7 in the frequency region from 4 to 90 cm^{-1} . The interference fringes are due to the plane parallel surfaces of the samples. The real part of the refractive index, n , of these samples is found from these fringes using Eqn. (3.7). The average refractive index of the samples for frequencies from 10 to 50 cm^{-1} is listed in Table 4.1. It is found that the values for low impurity concentration samples (S1, S2, S3 and S4) are lower than the room temperature values reported by Randall and Rawcliffe [37]; their measurements on intrinsic Ge samples with resistivities of 10 and 20 $\Omega\text{-cm}$ give a value for n of about 4.005 in this frequency region. As shown in Table 4.1, the refractive index of a sample increases as the impurity concentration of the sample increases; the refractive index increases from 3.88 for S1 to 4.04 for S7. The higher refractive index for doped Ge compared to intrinsic Ge at 4.2 K is also reported by S. Zwerdling and J. P. Theriault [5].

TABLE 4.1. Refractive Index of NTD Ge at $T=3$ K.

Sample	S1	S2	S3	S4	S5	S6	S7
N_a (10^{15} cm^{-3})	1.88	3.25	6.96	13.9	21.7	26.7	36.5
n	3.88	3.91	3.94	3.95	4.00	4.01	4.04
	± 0.01	± 0.01	± 0.01	± 0.01	± 0.01	± 0.01	± 0.05

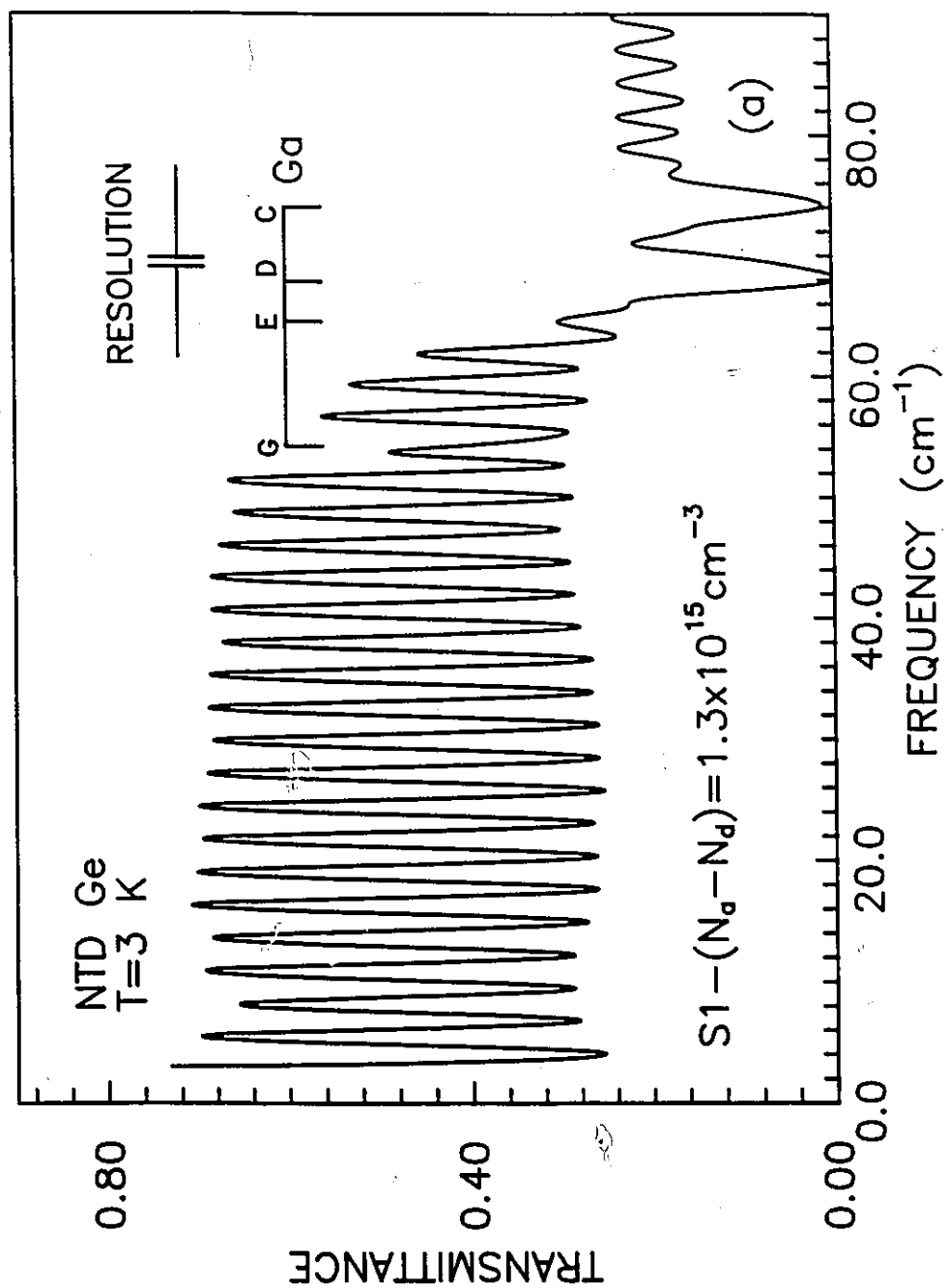
There are two main absorption processes present in these transmission spectra: first, at lower frequencies ($< 50 \text{ cm}^{-1}$), the main absorption mechanism is due to far-infrared photon-induced hopping of a charge carrier

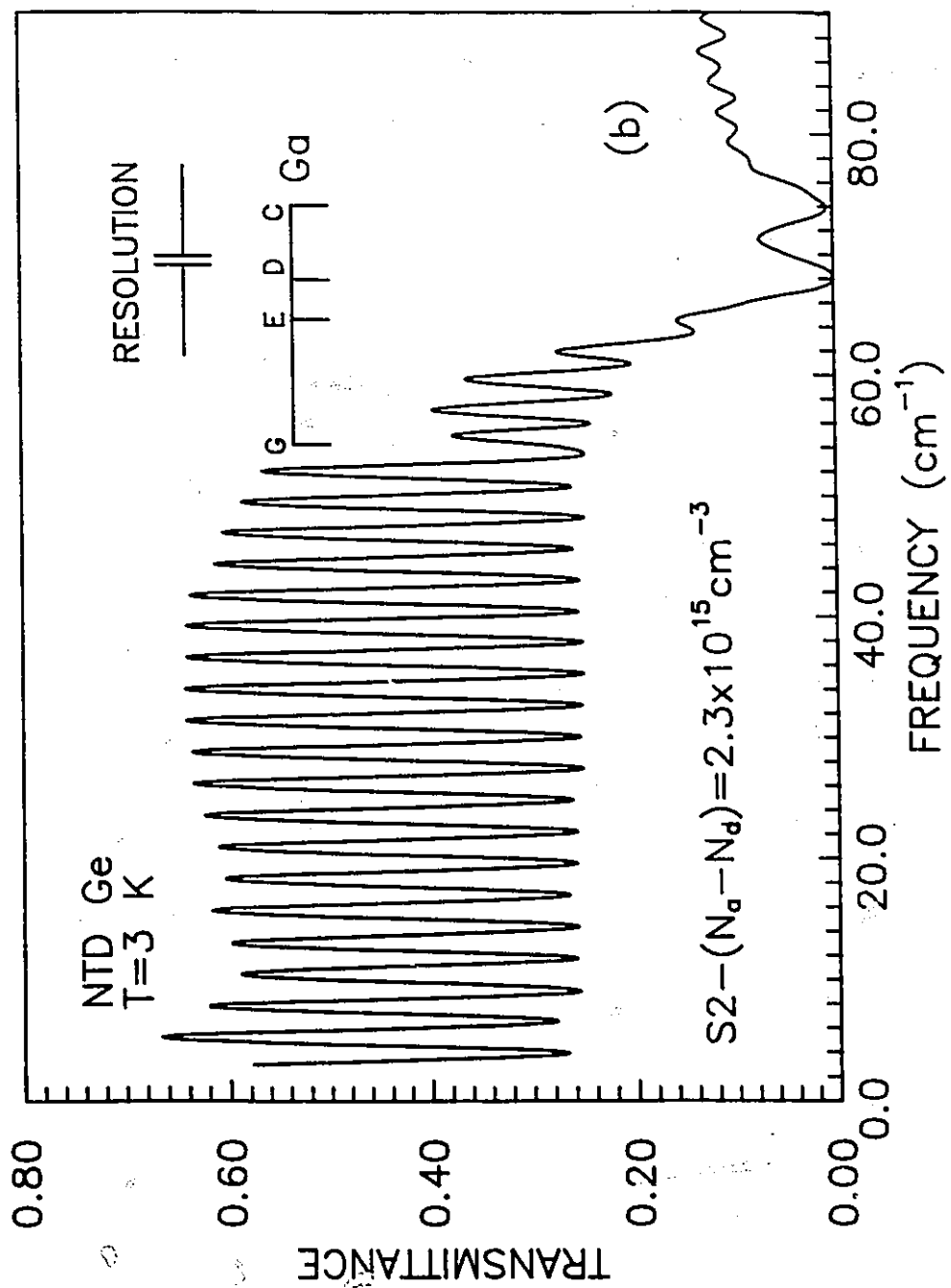
between Ga impurity centers near an ionized donor. Second, the strong absorption region at high frequencies ($> 40 \text{ cm}^{-1}$) is associated with hole transitions from the ground state to excited states of the Ga impurity. A brief description of this latter absorption process will be given before a detailed discussion of the absorption due to the photon-induced hopping process is given.

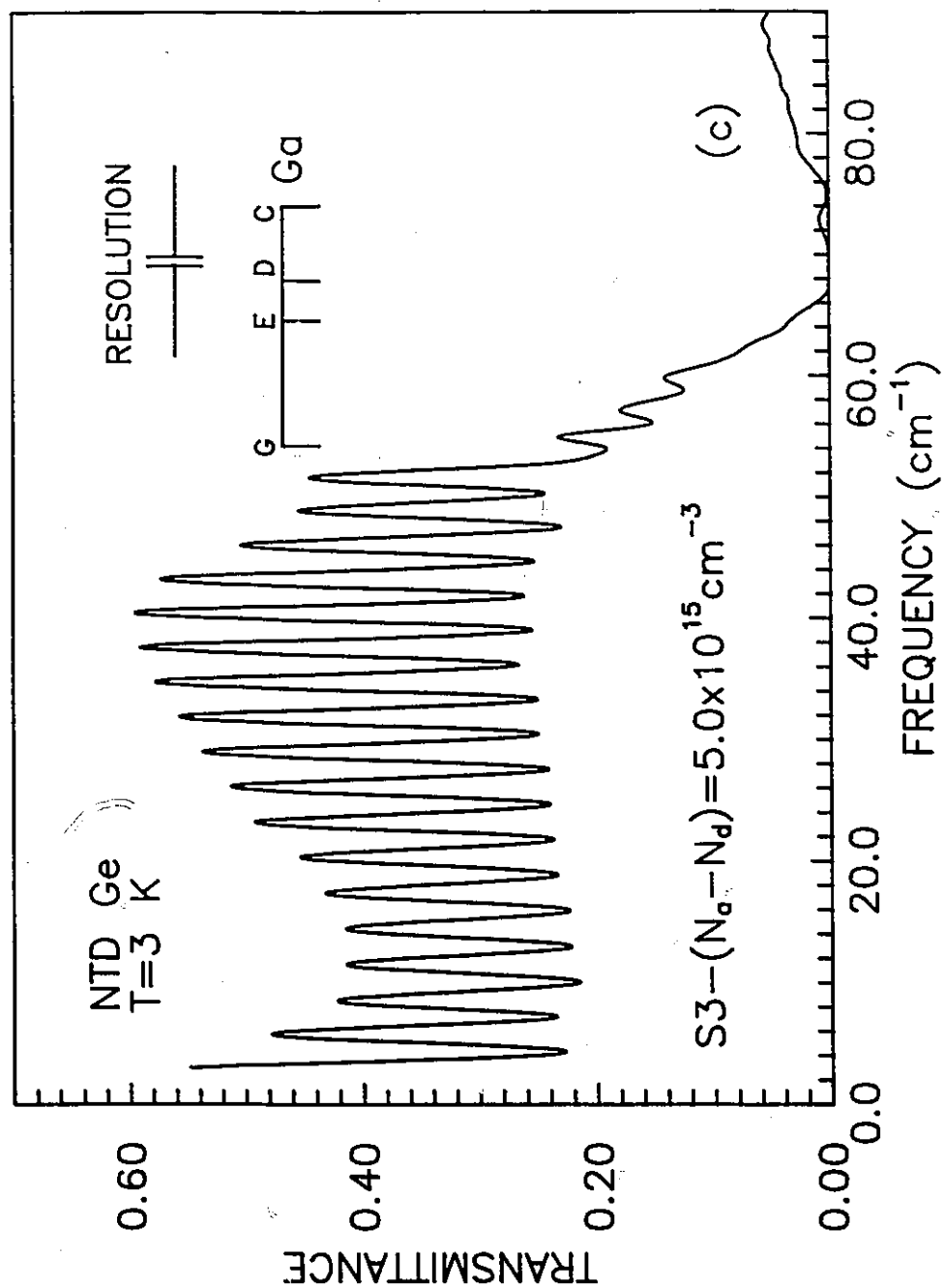
The well-known excited states for the Ga impurities in Ge [39] are labeled in the spectra shown in Figs. 4.1. At low impurity concentrations (S1-S2), it is possible to identify the excited states with the known Ga impurity excited states as shown in Figs. 4.1a-b for S1-S2. However, as the impurity concentration increases, the broadening of the states makes such identification impossible as shown in Figs. 4.1c-g for S3-S7. Fig. 4.2 shows the absorption spectra from $30\text{-}80 \text{ cm}^{-1}$ for samples S1-S7 as obtained from the transmission spectra of Figs. 4.1 using the method described in Section 3.4. At low concentrations, all impurities can be treated as non-interacting impurities which behave like isolated atoms. However, as the impurity concentration increases, it can be shown that the first effect on the isolated impurity is due to nearest-neighbor interactions [40]. The broadening of the lower edges of the sharp lines due to the increasing impurity concentration has been observed for both donors and acceptors in Si and GaAs [40]. It is concluded that the broadening is due to neutral impurity pairs for low impurity concentrations. Because the impurities are randomly distributed, the effect will first arise from pairs which are closer than average. Similar absorptions at the lower energy shoulders of excited states are also observed in these spectra as identified in Fig. 4.2. For instance, the absorption at the shoulder of the lowest state G, D_{G_1} , may be similar to the absorption due to the band

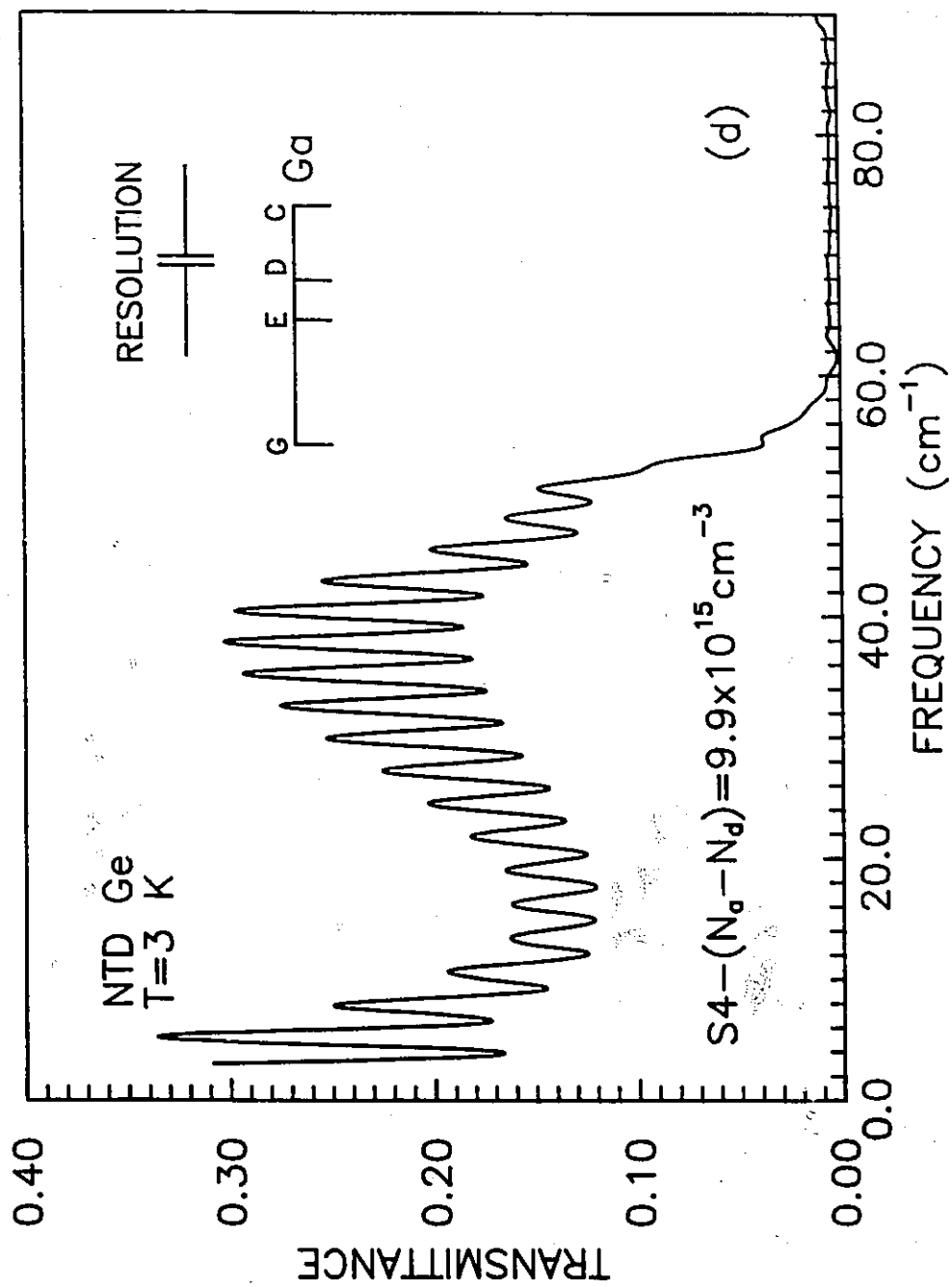
Figure 4.1 Transmission spectra for NTD Ge samples S1-S7 at a temperature of 3 K in the region from 0 – 90 cm^{-1} . The known Ga excited states are included. All spectra have a resolution of approximately 0.8 cm^{-1} .

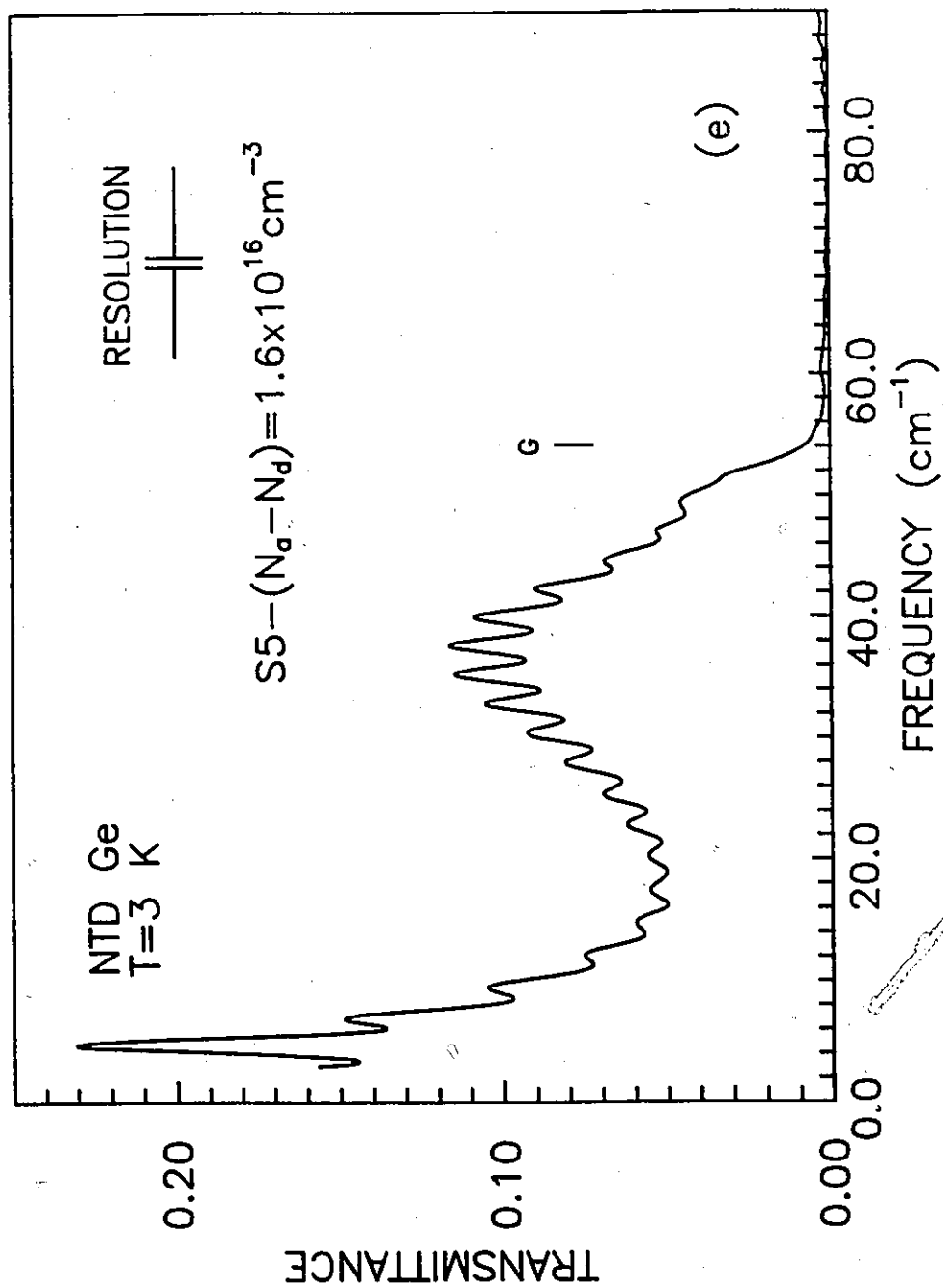


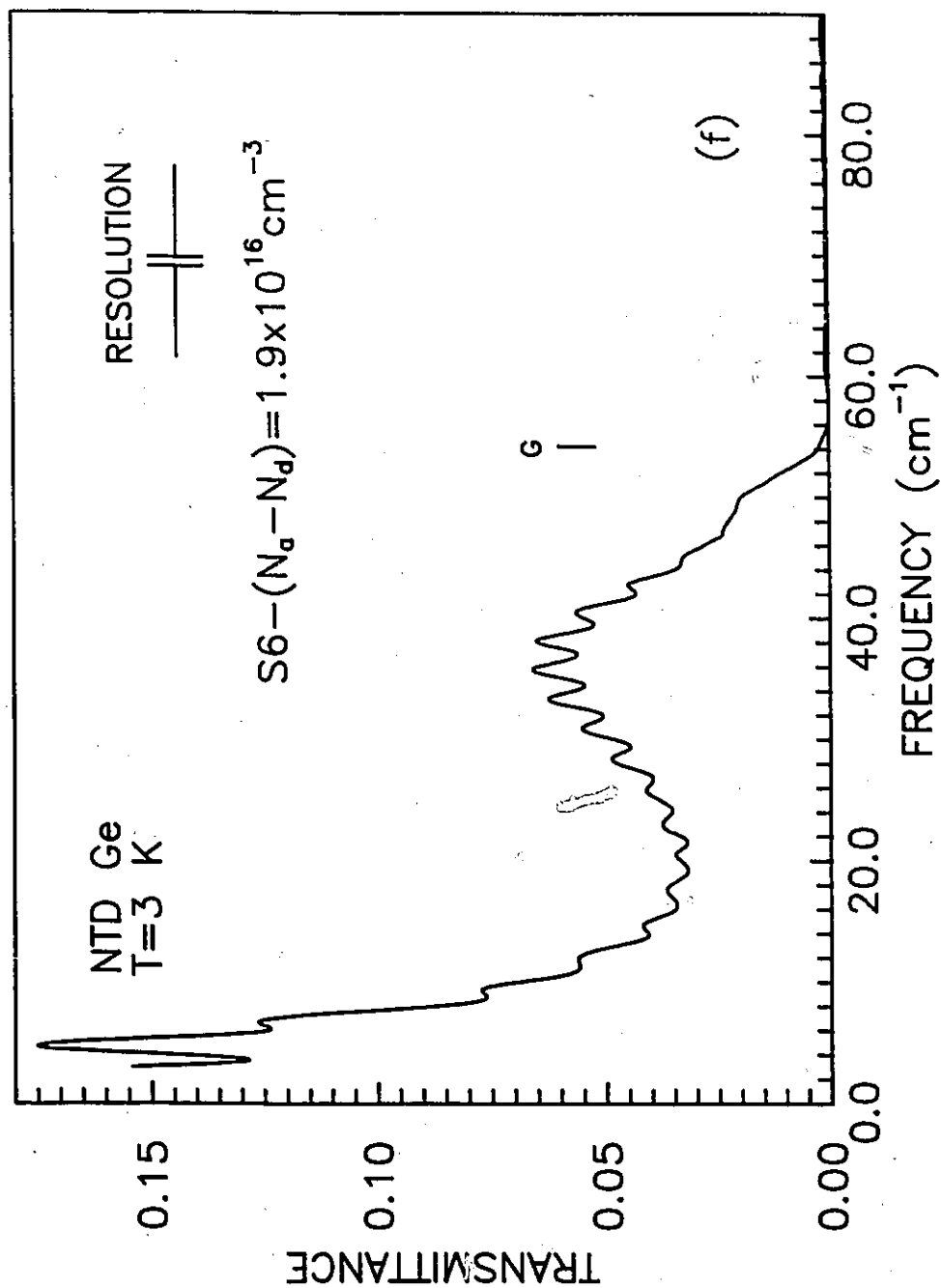


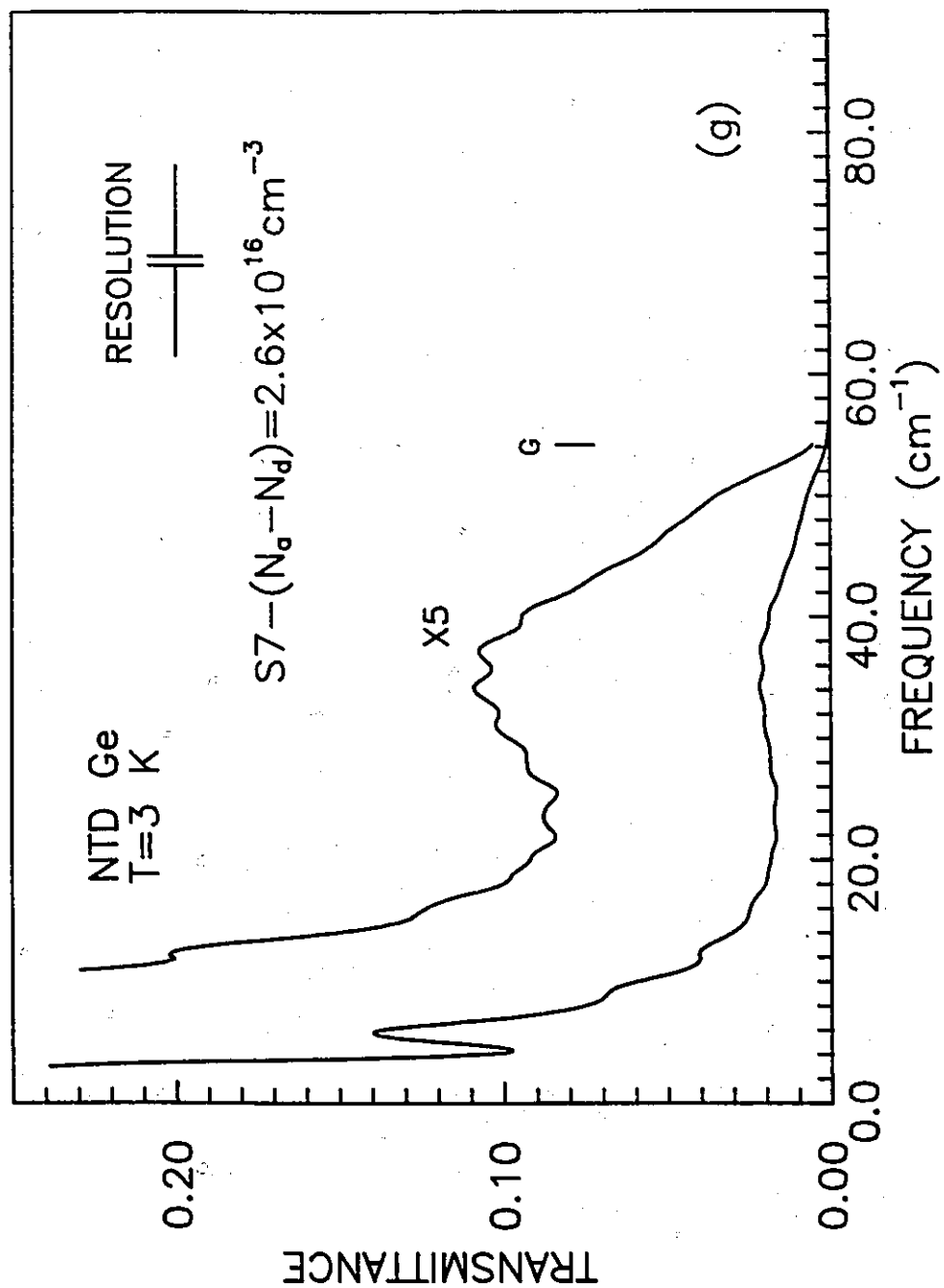










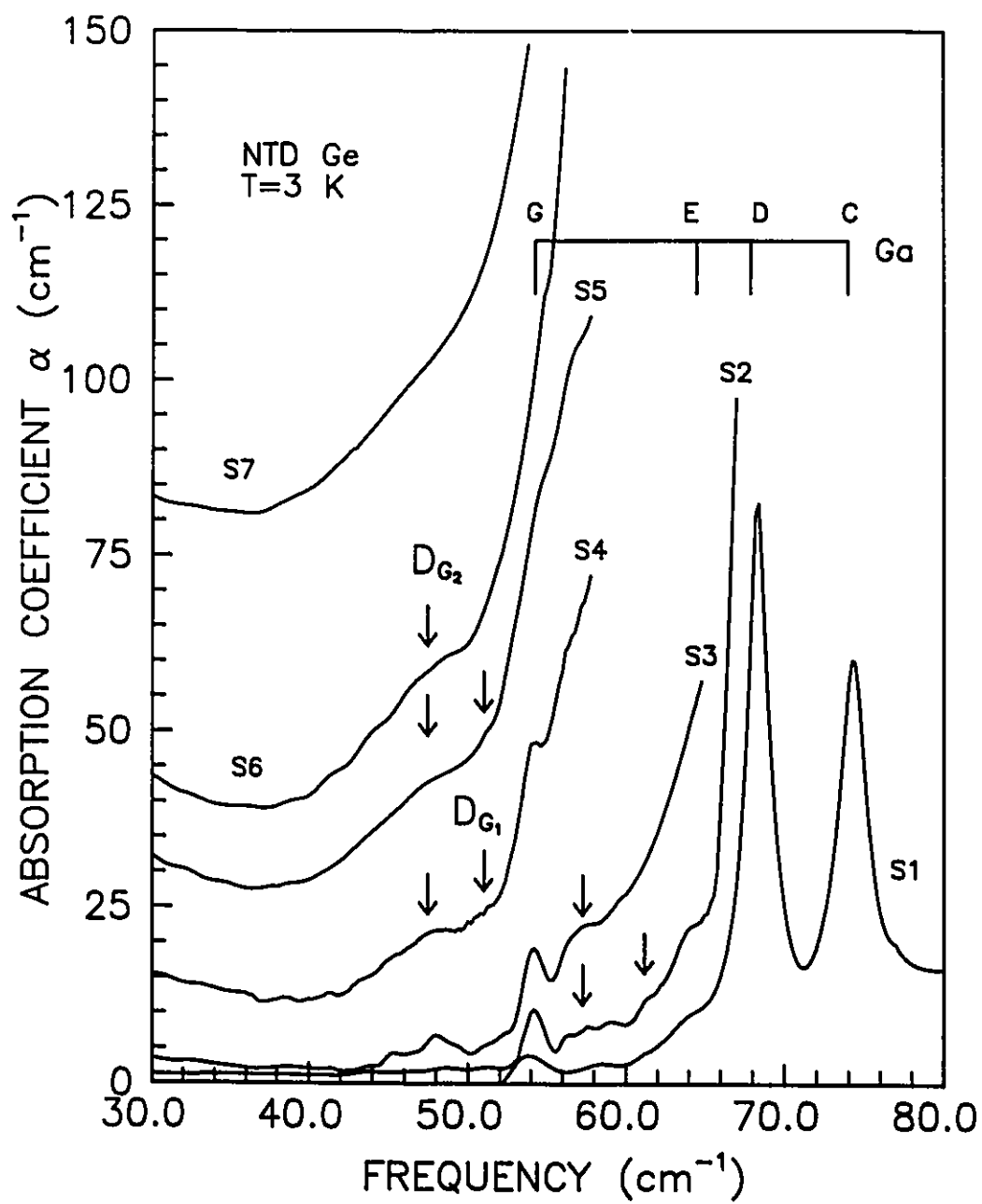


states, $D_{1s}D_{2p_0}$, in P-doped Si. These shoulder absorptions are in fact due to excitations from the $1s$ to the $2p_0$ state of the same donor, but with another donor nearby in the ground state so that the energies of both ground and excited states are reduced. It is also observed that there is another absorption at energies lower than the $D_{1s}D_{2p_0}$ states [40]. This is attributed to the charge-transfer excitation forming D^+D^- with a considerable reduction in the energy of the excited state because of the Coulomb attraction. This excitation has been referred to as an exciton state located in the Hubbard band gap between D^- and D^+ states. The lowest absorption shoulder, D_{G_2} , may be due to the same charge-transfer excitation. This is not the same as the photon-induced hopping absorption discussed later because these pairs are neutral.

As the impurity concentration keeps increasing, the impurities will get closer to one another, thus forming triples and then clusters [40]. The effect of increasing the impurity concentration is to increase the number of larger clusters. The absorption edge is dominated by the localized states within random clusters of impurities with densities greater than the average. The cluster will give rise to the absorption at low energies. This effect is clearly demonstrated in these spectra. The absorption starts at lower frequencies as the concentration of the Ga impurity increases. It is noted that the absorption shoulder due to pair absorptions is not visible in the S7 spectrum.

Now, let us discuss the absorption due to photon-induced hopping. Fig. 4.3 shows the absorption spectra from $4\text{--}60\text{ cm}^{-1}$ for samples S2-S7. Broad absorptions are observed for samples S2-S7. However, the absorption in this frequency region is negligible for sample S1. This indicates

Figure 4.2 Absorption spectra for samples S1-S7 in the region from 30-80 cm^{-1} . These spectra are obtained from the transmission spectra in Figs. 4.1. The main absorption process in this region is due to the excitation of a neutral Ga impurity. The arrows indicate those absorptions due to neutral pairs with random separation.



that the number of localized pairs is small at such low Ga concentration ($1.9 \times 10^{15} \text{ cm}^{-3}$). This is in agreement with the sharp lines observed for the excited states of Ga in this sample.

The absorption coefficient for all frequencies in this region increases as the samples' impurity concentration increases. The absorption coefficient at the maximum ($\alpha(\omega_{\max})$) of the broad absorption curve increases from 2 cm^{-1} for S2 to 87 cm^{-1} for S7. The frequency of this maximum absorption (ω_{\max}) also shifts to higher frequencies as the impurity concentration increases. The change is from 10 cm^{-1} for S2 to 23.8 cm^{-1} for S7. These results are listed in Table 4.2. Figs. 4.4a and 4.4b plot ω_{\max} and $\alpha(\omega_{\max})$ versus the net carrier concentration $(N_a - N_d) = (1 - K) \cdot N_a$. The data on these graphs are least-squares fit to a power-law function $y = a \cdot (N_a - N_d)^n$. It is found that the power dependence for ω_{\max} and $\alpha(\omega_{\max})$ are $n=0.37$ and 1.44 respectively. However, the absorption due to excitations of impurity centers has not been separated from the experimentally determined absorption spectra and hence, contributes to the absorption even at the frequency of the maximum. This is more serious for the high concentration samples because such absorption starts at lower frequencies. This is especially significant for sample S7; therefore, another best fit is done for the $\alpha(\omega_{\max})$ data without the data point from S7. It is found that $n=1.31$ instead of 1.44 in this case. It is interesting to compare these results with the Blinowski and Mycielski theory. From the predicted n-type Si absorption spectra in Fig. 2.4, it is found that the frequency of the maximum absorption is proportional to $N_d^{0.41}$ ($n = 0.41$) and that the absorption at the maximum is proportional to $N_d^{1.36}$ ($n = 1.36$). These values are close to the experimental values for p-type NTD Ge presented here ($n=0.37$ and 1.31).

Figure 4.3 Absorption spectra for samples S1-S7 in the region from 0 – 60 cm^{-1} . The dashed lines are obtained from the transmission spectra. The solid lines are fits to a polynomial function for frequencies from 4 – 32 cm^{-1} . The main absorption process in this region is due to the photon-induced hopping of a charge carrier between pairs situated near an ionized donor.

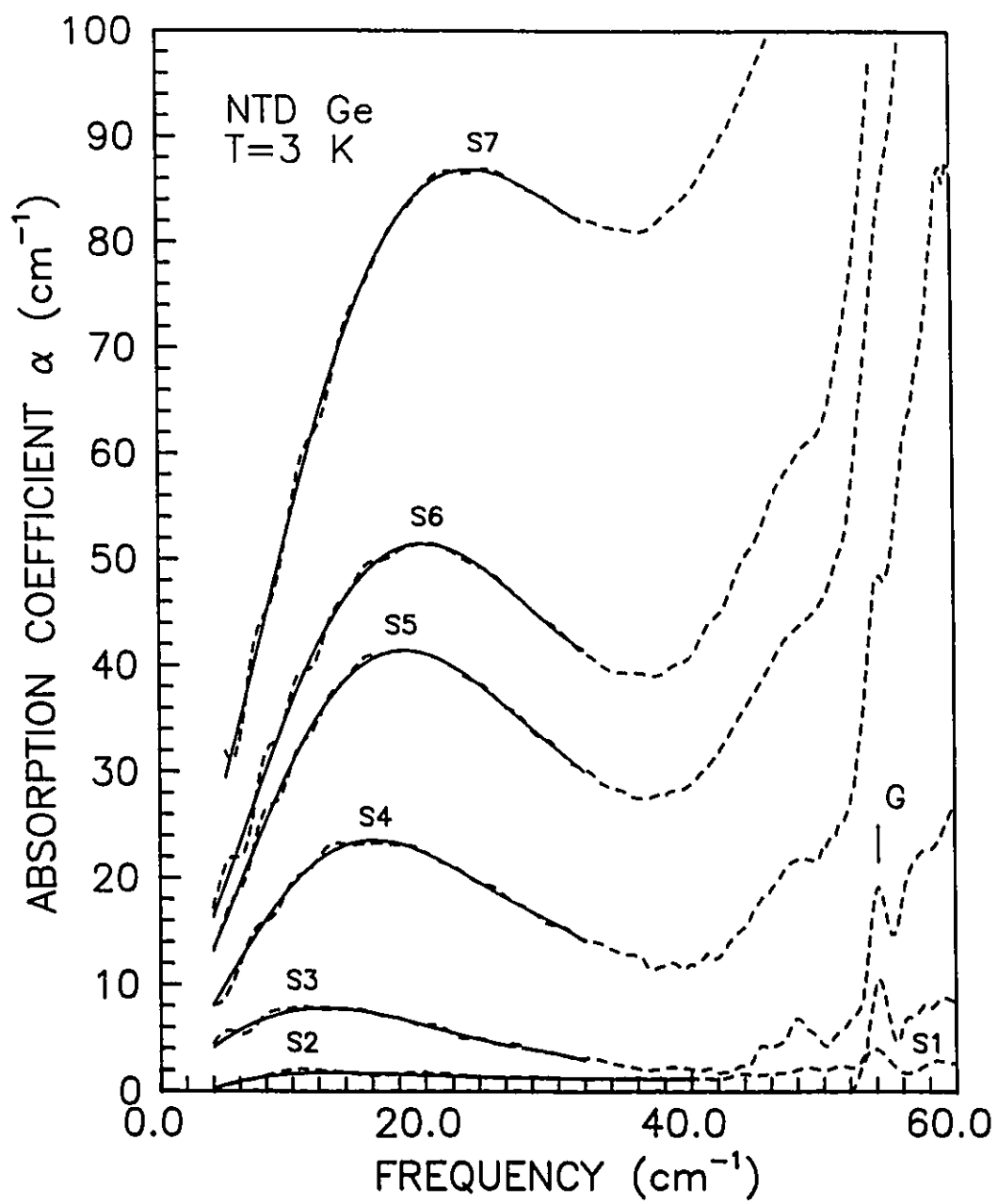


TABLE 4.2. ω_{\max} and $\alpha(\omega_{\max})$ of the Absorptions

Sample	S1	S2	S3	S4	S5	S6	S7
$\omega_{\max}(\text{cm}^{-1})$		10.0	12.0	16.2	18.6	20.2	23.6
$\alpha(\omega_{\max})(\text{cm}^{-1})$	0	1.8	7.9	23.6	41.4	51.3	57.0

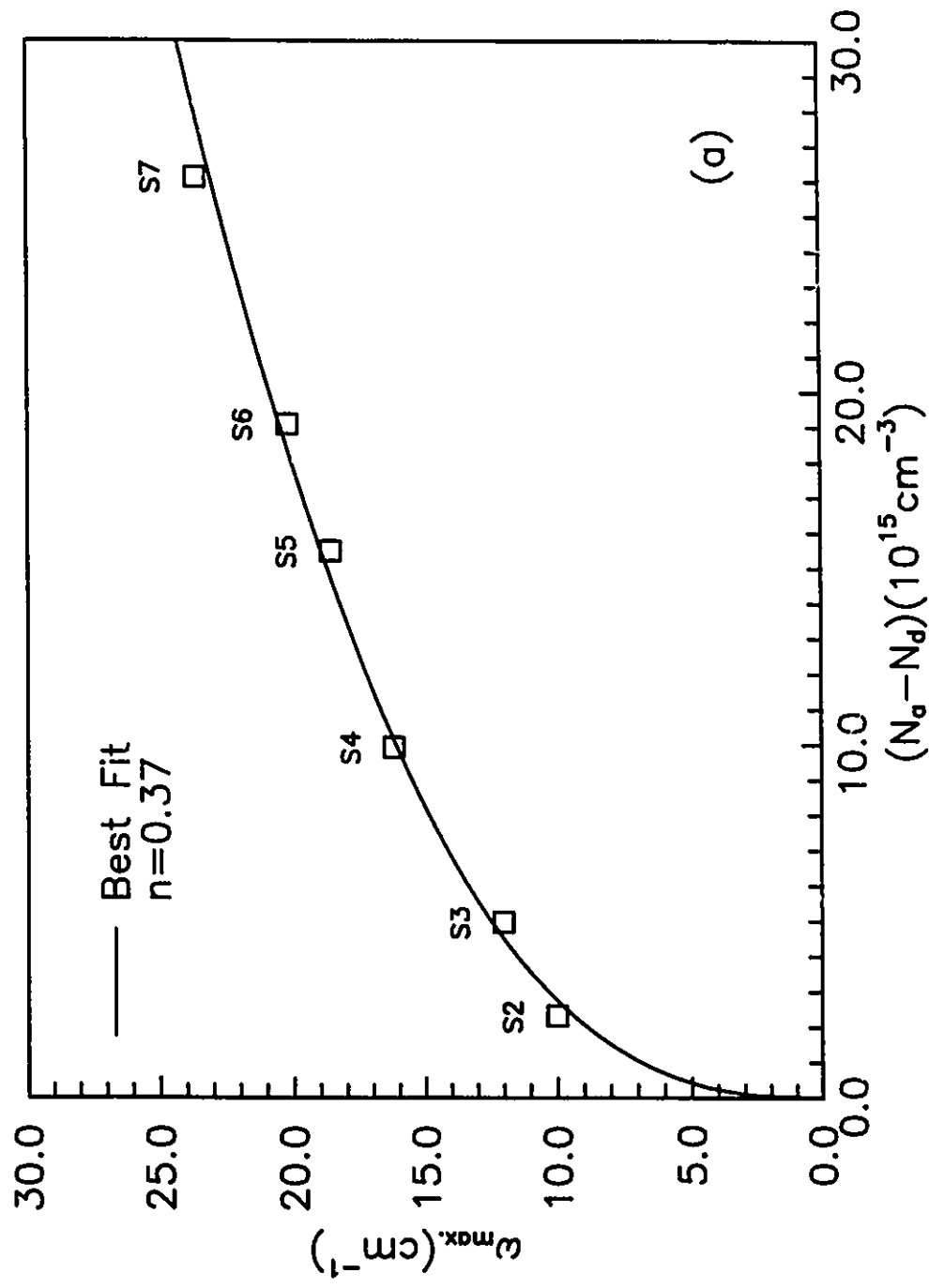
According to Eqn. (2.20), the frequencies of the maximum ω_{\max} are predicted to be proportional to $N_a^{2/3} r_w$, where r_w is the distance between the pairs which satisfies Eqn. (2.7) at ω_{\max} . Experimental results show that ω_{\max} is proportional to $N_a^{0.37}$. Therefore, r_w is proportional to $\approx N_a^{-0.3}$. That means that the value of r_w at the maximum is roughly proportional to the average distance between majority impurities, $N_a^{-1/3}$, which is the characteristic scale of the system.

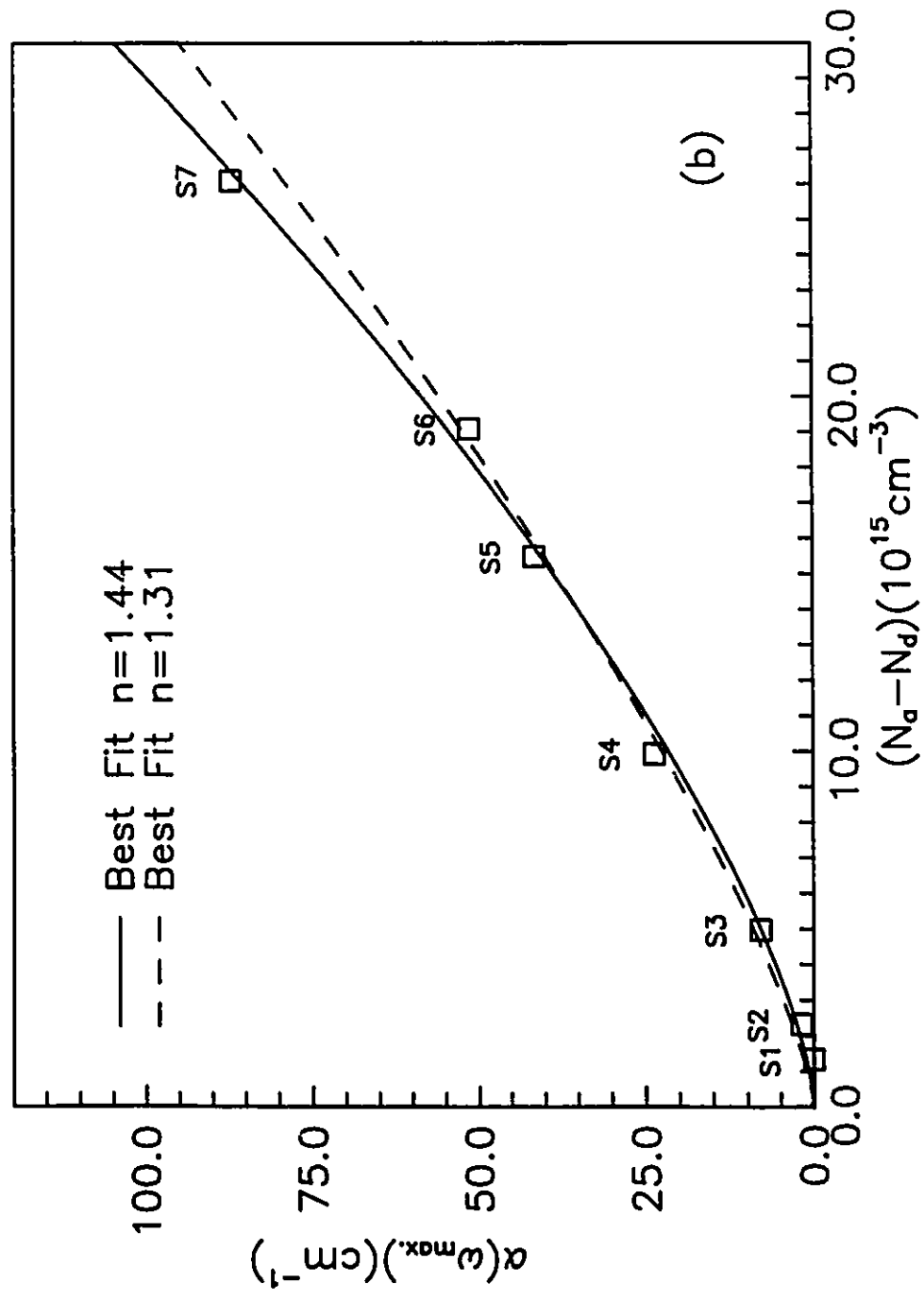
Least-squares fits to a linear function are done for the low frequency region of the spectra as shown in Fig. 4.5. The best fit lines are extended to zero frequency. The values of the y-intercept are 0.75, -0.04, 1.0, 1.5, and 4.9 cm^{-1} for samples S3, S4, S5, S6 and S7 respectively. These values correspond to the absorption coefficients at zero frequency. It is noted that the absorption coefficient $\alpha(\omega)$ can be deduced from the conductivity $\sigma(\omega)$ as follows [41]:

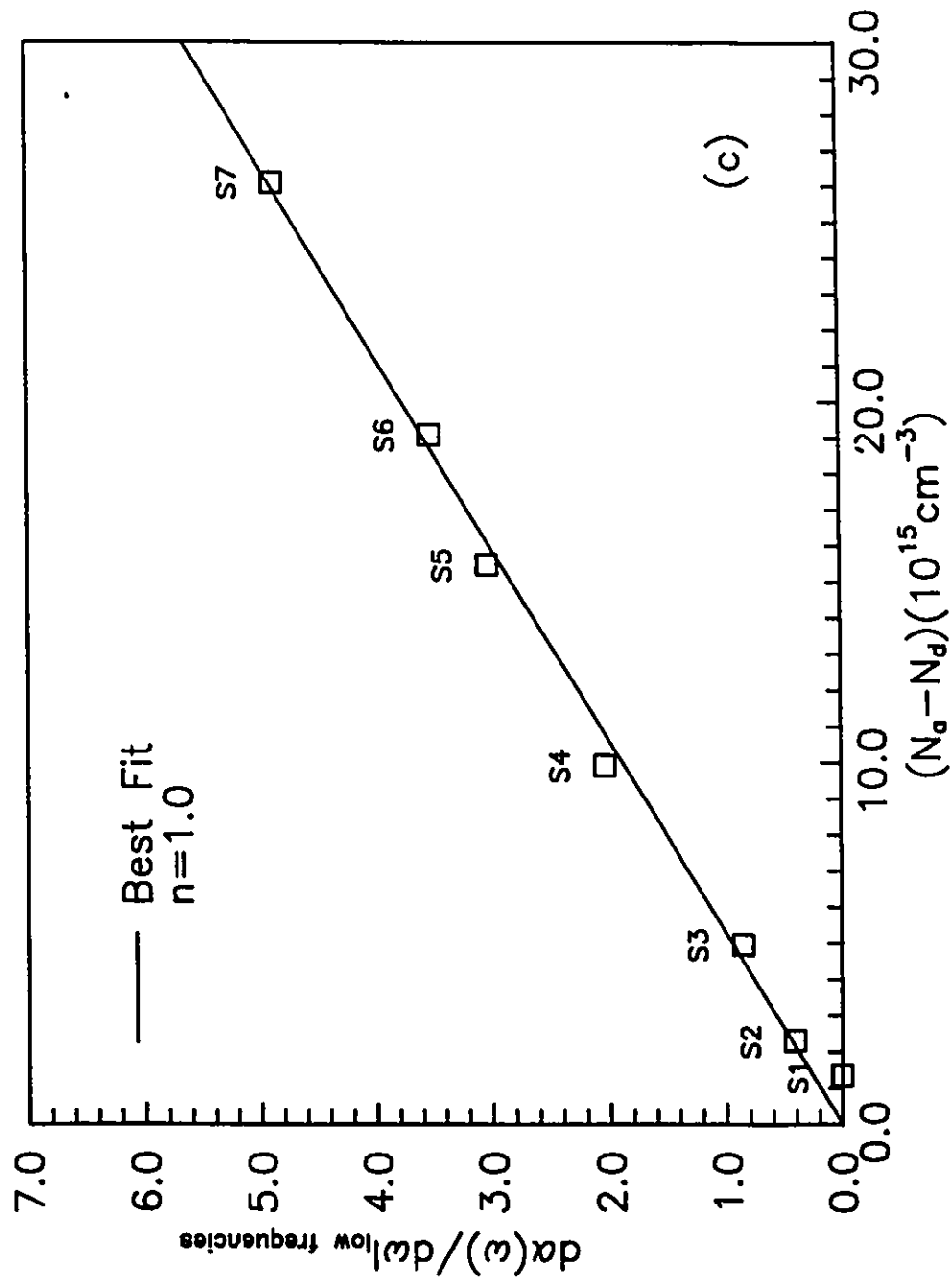
$$\alpha(\omega) = \frac{4\pi\sigma(\omega)}{nc}, \quad (4.1)$$

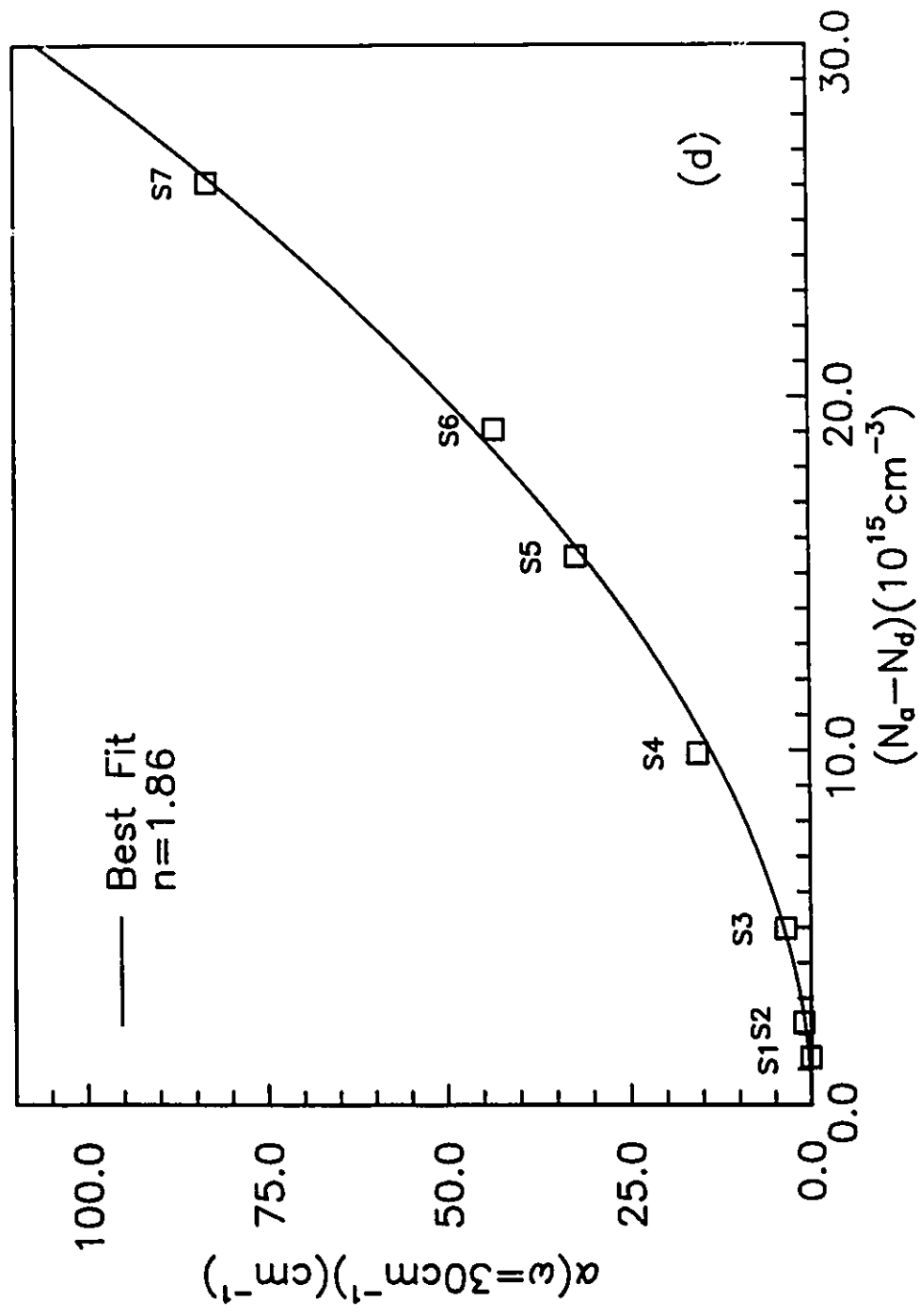
where, n is the refractive index and c is the speed of light. Substituting the value of $n=4$ for Ge gives the relationship $\alpha(\omega) = 94.2\sigma(\omega)$, where $\alpha(\omega)$ is in cm^{-1} and $\sigma(\omega)$ is in $\Omega^{-1}\text{cm}^{-1}$. The d.c. resistivities at $T=3$ K for samples S3, S4, S5, S6, and S7 are approximately 7×10^3 , 320, 110, 80, and 20 Ωcm respectively. Hence, the absorptions at zero frequency (i.e., $\alpha(0)$) are 0.01,

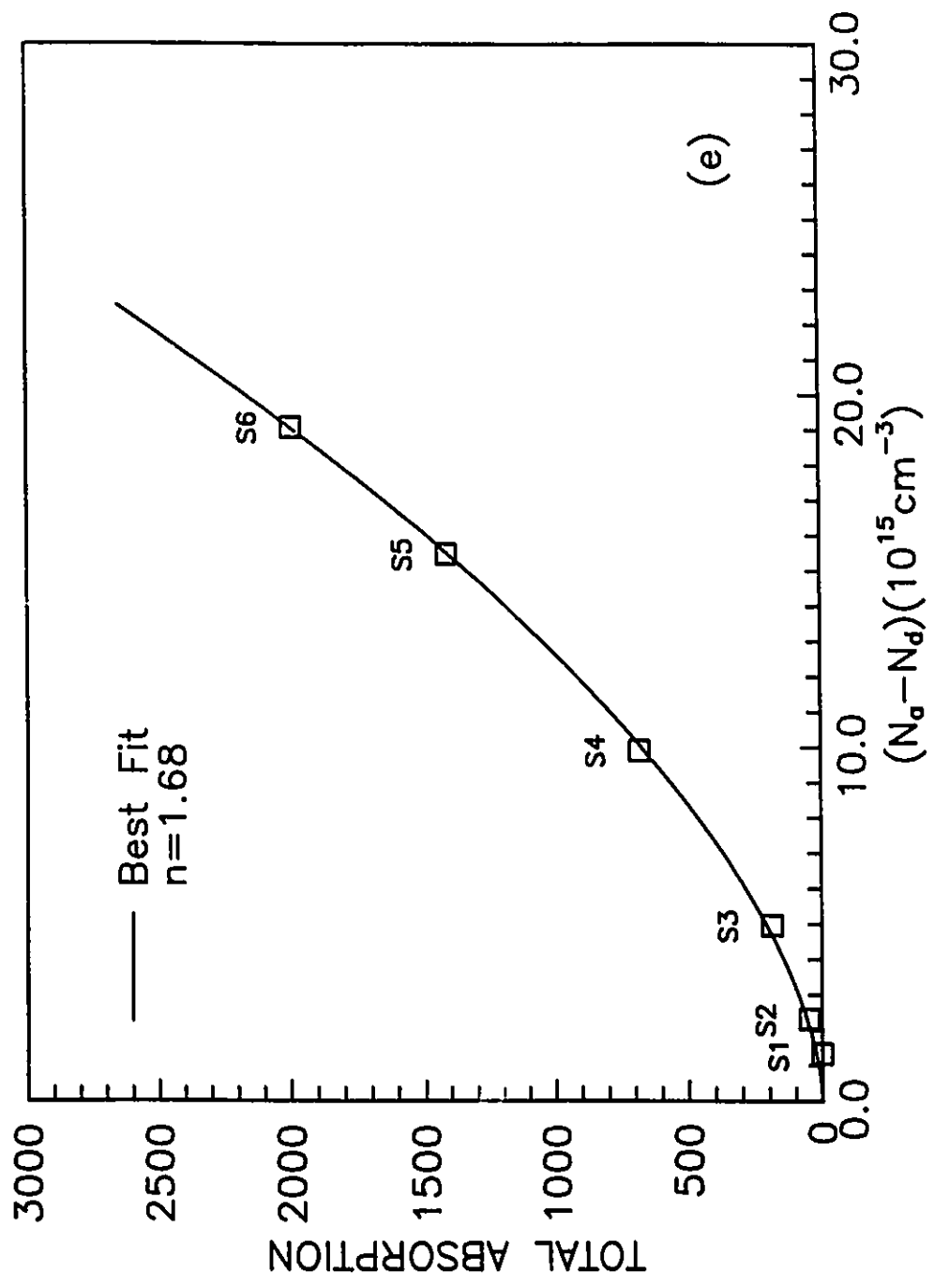
Figure 4.4 General properties of the absorption spectra in Fig. 4.3 versus impurity concentration: (a) the frequency of maximum absorption, ω_{\max} , (b) the absorption coefficient at the maximum, $\alpha(\omega_{\max})$, (the dashed line is the best fit without the data point S7) (c) the slope of the spectra at low frequencies, $d\alpha/d\omega|_{\text{low } \omega}$, (d) the absorption coefficient at 30 cm^{-1} , $\alpha(30\text{cm}^{-1})$, and (e) the estimated total absorption due to the photon-induced hopping process. The solid lines shown are least-squares fits to the power-law function $y = a \cdot (N_{\text{a}} - N_{\text{d}})^n$.











(e)

0.3, 0.9, 1.2, and 4.7 cm^{-1} . These values are consistent with those obtained from the extrapolated linear function fits shown in Fig. 4.5. This suggests that at low frequencies, the absorption is approximately proportional to frequency.

The linear part of the absorption spectrum extends to higher frequencies as the impurity concentration increases. This linear frequency dependent absorption at low frequencies is different from the predicted spectra for n-type Si as shown in Fig. 2.4. The difference may be due to many reasons; for instance, at low frequencies, the absorption is proportional to ωr_ω^3 where r_ω decreases as ω increases for the hydrogen-like model (see Eqn. (2.7)). The behavior of ωr_ω^3 is clearly demonstrated in the low frequency region of the theoretical spectra shown in Fig. 2.4. However, if r_ω at low frequencies is less dependent on frequency than what is predicted by the hydrogen-like model, then the absorption will behave more linearly with frequency at low frequencies. Another possible explanation arises from the fact that the degree of compensation in NTD Ge is not small ($K > 0.2$). It can be shown that the Coulomb gap is of the order of the impurity band [12] and cannot be ignored in the low energy regime. In this case, the absorption at low frequencies should obey the expression in Eqn. (2.18b). The dependence of absorption on frequency is ω/r_ω ; hence, the dependence on r_ω is weaker. It is noted that the dependence on r_ω is changed from r_ω^3 to $1/r_\omega$ due to the existence of the Coulomb gap. Although the linear frequency dependent absorption is not clearly predicted from any theory, the possibility of having a weaker r_ω dependence is demonstrated. There are also dipole-dipole interactions which have been ignored in the above discussion, and which contribute a factor which depends logarithmically on the frequency.

Figure 4.5 The experimental absorption spectra V1,V2 and V3 obtained by Vavilov *et al.*. The present results S3-S7 are shown together for comparison. Note that the longer dashed lines are the least-squares fits of linear functions at low frequencies. The "|" on the spectra denotes the upper limit of frequencies used for the linear fits. The values of the y-intercepts for these linear fitted lines are consistent with the values obtained from the d.c. resistivity measurements (see text) except S3. The linear part of spectrum S3 probably occurs at lower frequencies ($< 4 \text{ cm}^{-1}$) so that the extrapolated y-intercept from the linear fit is too large in comparison with the value obtained from the d.c. measurement.

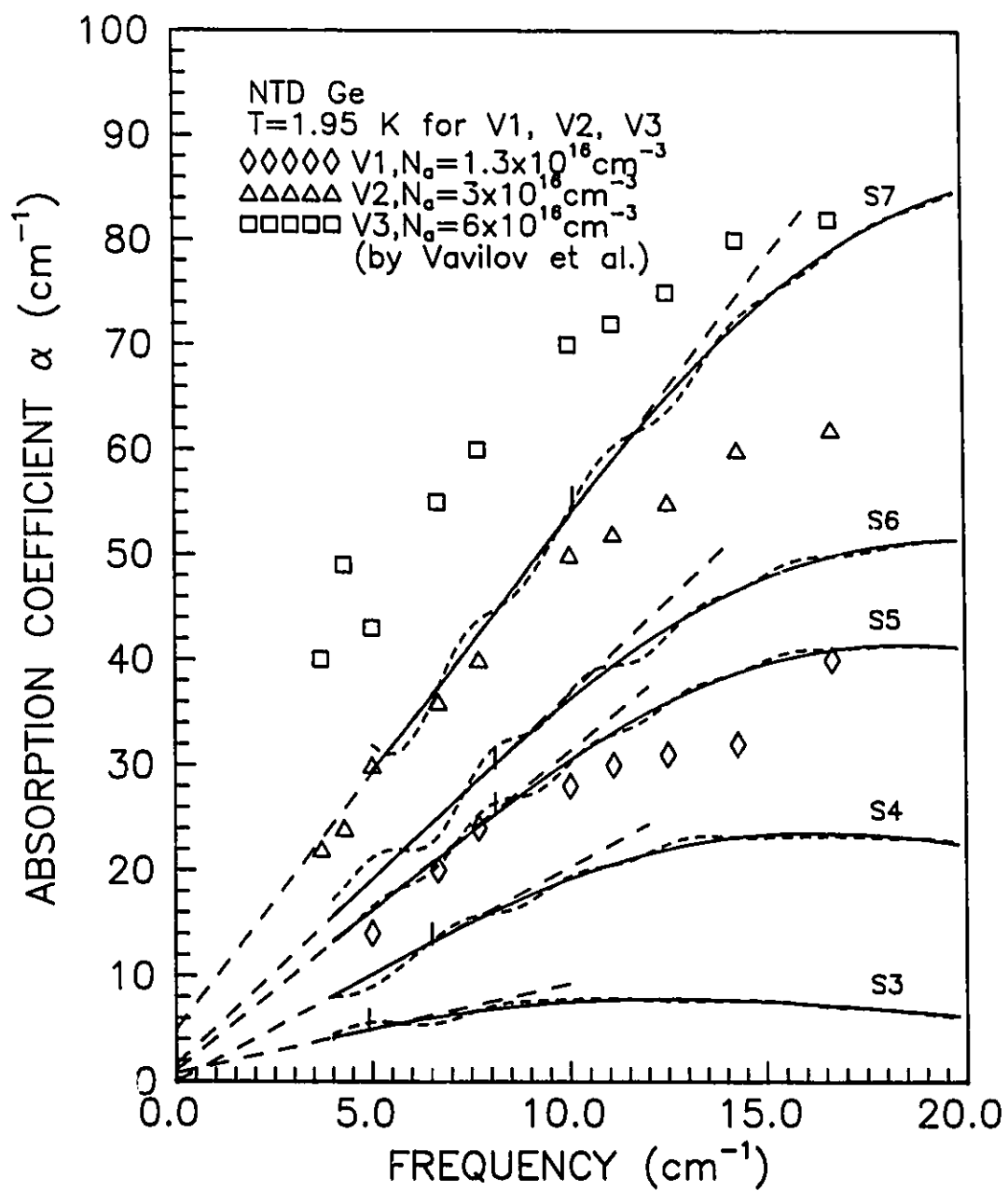


Figure 4.4c plots the slopes of these linear fitted lines at low frequencies ($d\alpha/d\omega|_{\text{low } \omega}$) versus carrier concentration. The best fit curve to the power-law function for these data is obtained for the power $n=1.0$. The theoretical slope of the absorption spectrum at $\omega = 0$ can be obtained from Eqn. (2.18a) and it is found to be proportional to $N_a^{4/3}$ (i.e., $n=4/3$). One of the factors contributing to this difference may be that the theoretical value is obtained for $T=0$ K; whereas, the experimental value is obtained at $T=3$ K. The non-zero temperature will have the largest effect on the absorption spectrum at low frequencies (i.e., $\hbar\omega < kT$).

The absorption of the samples at $\omega = 30 \text{ cm}^{-1}$ ($\alpha(30\text{cm}^{-1})$) is plotted in Fig. 4.4d, the best fit line being obtained for the power $n=1.86$. In the high frequency limit, it is theoretically found that the absorption is proportional to N_a^2 as in Eqn. (2.19). The absorption in the region $22\text{-}32 \text{ cm}^{-1}$ is found to vary almost linearly with the frequency. The theory predicts that it is roughly proportional to r_ω^4 .

Finally, the total absorption, which is defined as the area under the broad absorption for the hopping process, can be estimated from the spectra. The low frequency absorption ($< 4 \text{ cm}^{-1}$) is estimated by extending the linear fitted line of the spectrum. Similarly, the high frequency absorption is estimated by extending the absorption curve in the linear region of the spectrum ($22\text{-}32 \text{ cm}^{-1}$) to high frequencies. The results are plotted in Fig. 4.4e. S7 is not included in the best fit due to the large error which is caused by the strongly overlapping Ga impurity absorption. It is found that the best fit line is obtained for the power $n=1.68$.

Figure 4.5 shows absorption spectra V1, V2 and V3 which were experimentally obtained by Vavilov *et al.* [7] for NTD Ge with different impurity

concentrations. It is evident that their V1 and V2 absorption spectra are similar to the presented spectra S5 and S7 in the low frequency region. Their V1 essentially overlaps S5 within the experimental uncertainty at frequencies below 10 cm^{-1} and V2 is only slightly below S7. The acceptor concentrations of V1 and V2 are 1.3 and $3 \times 10^{16} \text{ cm}^{-3}$ respectively, which compare with 2.2 and $3.7 \times 10^{16} \text{ cm}^{-3}$ for S5 and S7 respectively. Thus, the present results are in good agreement with Vavilov *et al.*'s results particularly at low frequencies. However, at high frequencies, a discrepancy exists between the two works. The absorption coefficient of S5 and S7 is higher than that of V1 and V2 for frequencies above 10 cm^{-1} .

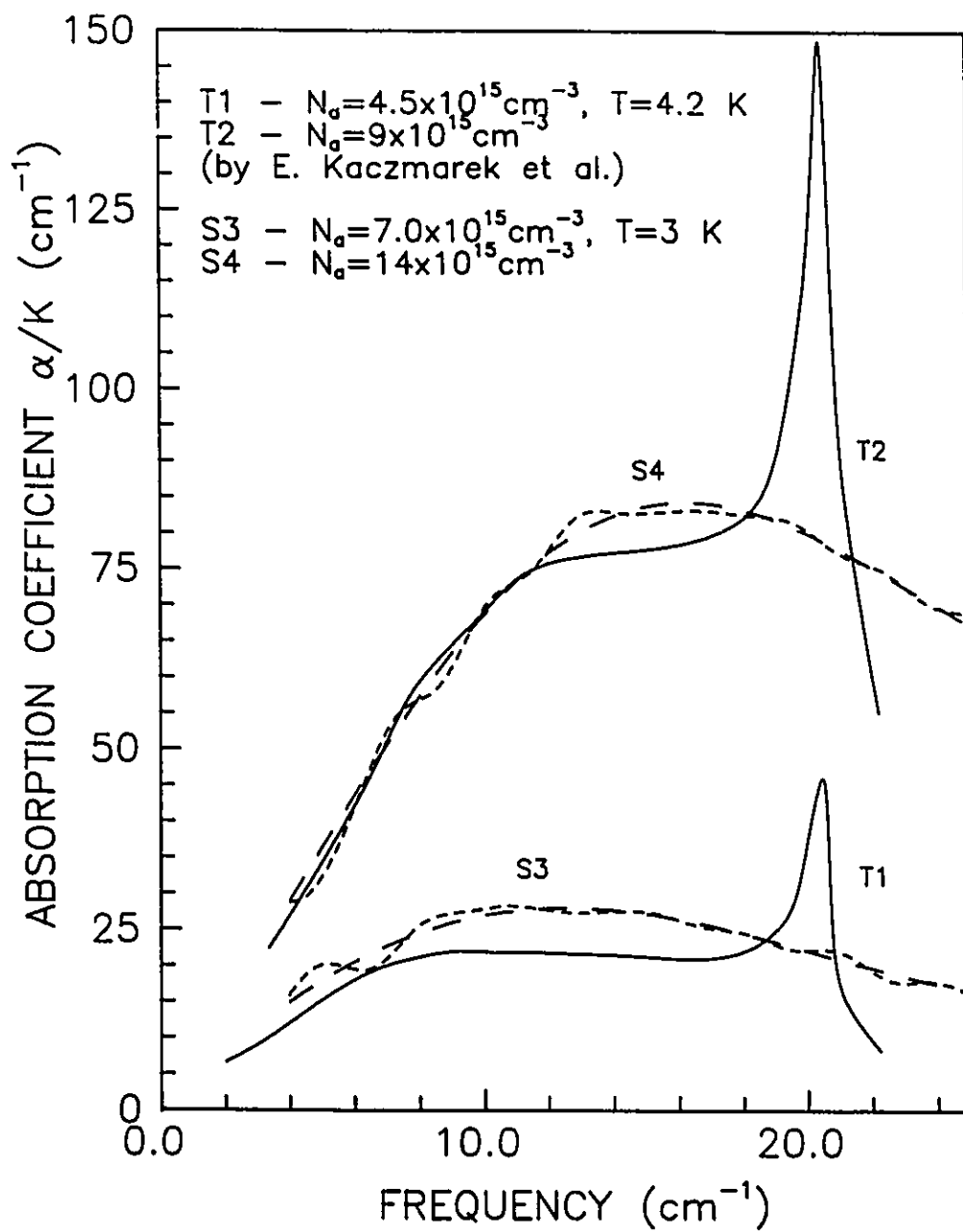
Figure 4.6 shows the theoretical absorption spectra T1 and T2 found by E. Kaczmarek and Z. W. Gortel [8] with N_a equal to 4.5 and $9 \times 10^{15} \text{ cm}^{-3}$ respectively. The absorption coefficient per unit compensation, α/K , is plotted since the theoretical spectra are calculated with the assumption that $K < 0.2$ and in this case α/K is independent of K . Absorption spectra S3 and S4 ($K = 0.286$) are shown for the purpose of comparison. It is first noticed that the theoretically predicted sharp peak is not observed. It is also found that the theoretical absorption curve T2 ($N_a = 9 \times 10^{15} \text{ cm}^{-3}$), is similar to S4 ($N_a = 14 \times 10^{15} \text{ cm}^{-3}$). Without considering the difference in N_a , the theoretical spectrum T2 is in excellent agreement with S4 for frequencies below 12 cm^{-1} . The theoretical absorption curve T1 ($N_a = 4.5 \times 10^{15} \text{ cm}^{-3}$), is close to, but below S3 ($N_a = 7 \times 10^{15} \text{ cm}^{-3}$). The general shape of these two spectra is similar for frequencies below 7 cm^{-1} . Considering that the theoretical curves (T1 and T2) do not have any adjustable parameters, these results show good agreement with the experimental spectra at low frequencies. However, when the concentration of acceptors, N_a , is taken into consideration, it

is concluded that the magnitude of the predicted absorption is higher than the experimental value at low frequencies. The discrepancy may be due to two reasons: first, the function $F(\Omega, r)$ is not properly described by the much simplified form in Eqn. (2.13). As discussed earlier, the compensation of the NTD Ge samples is 0.286, and therefore the Coulomb gap cannot be ignored. The number of states at low frequencies is limited by the existence of the Coulomb gap; therefore, $F(\Omega, r)$ in Eqn. (2.13) is overestimated in the low frequency region. Second, the energy overlap integral is not as strong as that obtained by E. Kaczmarek *et al.* [8] using the Schechter envelope function.

As shown in Fig. 4.6, there is very little agreement between experiment and theory at higher frequencies. The theoretical curves predict that ω_{\max} occurs at lower frequencies than that obtained experimentally. For instance, the maxima for T1 and T2 occur at about 8 and 11 cm^{-1} , compared to 12 and 16.3 cm^{-1} for S3 and S4. The theoretical spectra change very slowly with respect to frequency after these maxima until the sharp peak occurring at about 20 cm^{-1} . The absorption falls rapidly after this peak. None of these features are observed in the experimental spectra.

E. Kaczmarek *et al.* [8] have provided some comments on the possibility of the non-existence of their predicted sharp peak. First, the non-existence of the sharp peak may be due to some factor not taken into account in the theory, such as angular dependence of the resonance energies, which may give rise to a peak which is much broader than predicted. Second, it is possible that the Schechter envelope functions used in the theory do not properly describe the behavior of holes at such distances from the impurity which are important in this theory. The Schechter functions are constructed to give good agreement between the calculated and experimental values of the

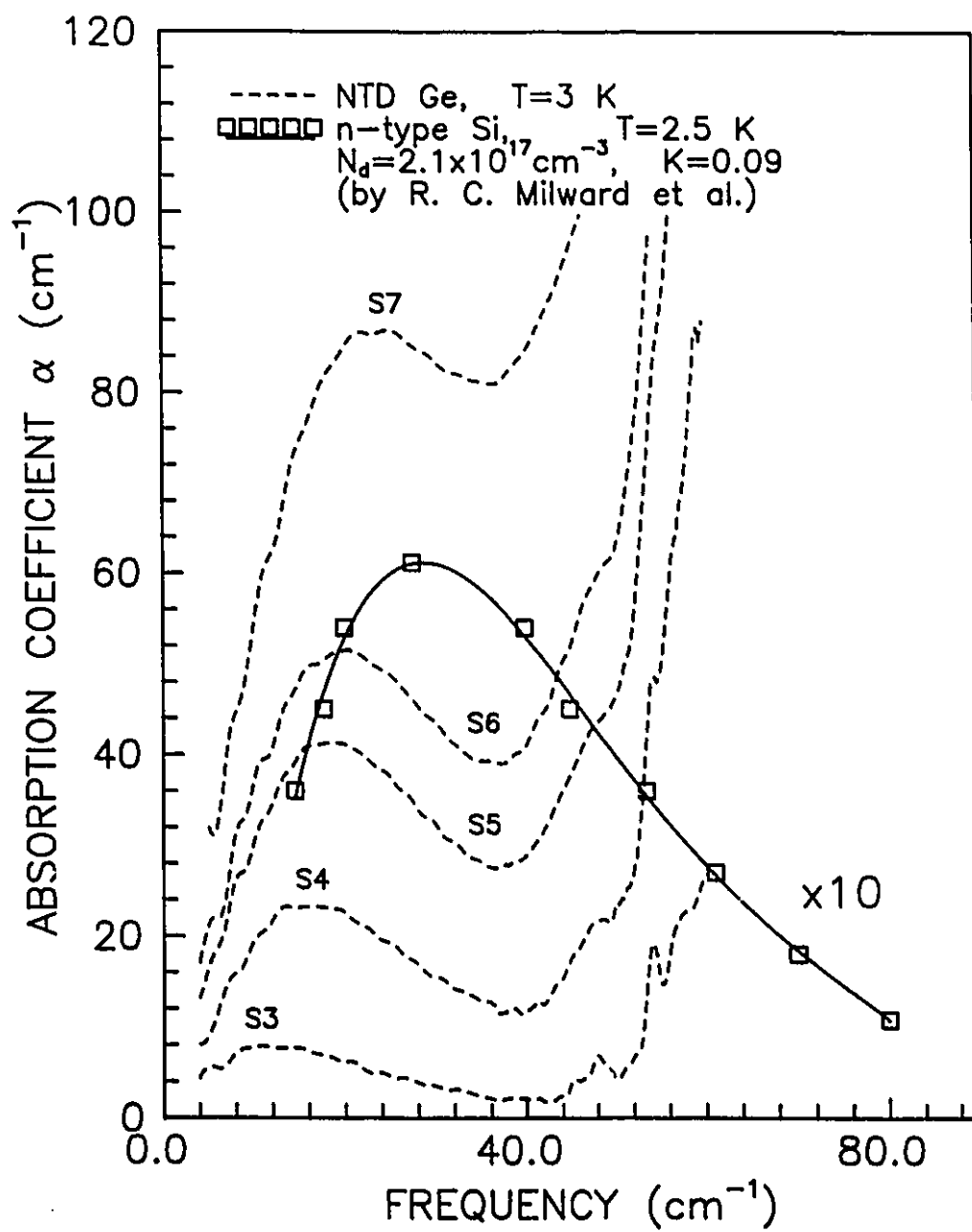
Figure 4.6 The relative absorption coefficient α/K versus frequency for the theoretical spectra T1 and T2 obtained by E. Kaczmarek *et al.* for p-type Ge with $K < 0.2$ in the region from $2 - 22 \text{ cm}^{-1}$. The present results S3-S4 ($K=0.286$) are shown together for comparison.



ground-state energy of the isolated acceptor. Therefore, the Schechter function describes satisfactorily the behavior of the hole situated not far from the acceptor. On the other hand, it is known that this function makes the set of effective mass equations internally inconsistent in an asymptotic limit as $r \rightarrow \infty$. Therefore, it is possible that this function is not suitable to describe the behavior of the hole at intermediate values of r , which are important for a hopping theory.

Figure 4.7 shows the absorption spectrum of compensated n-type Si obtained by L. J. Neuringer *et al.* [2] in the region between 15 and 80 cm^{-1} . This sample has $N_d = 2.1 \times 10^{17} \text{ cm}^{-3}$ and $K=0.09$. The absorption coefficient for the Si spectrum has been multiplied by 10. It is clear that the absorption coefficient for n-type Si is much weaker than that for NTD Ge. However, the general shape of the absorption spectra of the NTD Ge samples is very similar to that of the n-type Si sample. These results contradict the previous belief that the frequency dependence of the absorption coefficient is less pronounced in p-type than in n-type materials. It is clear that at higher frequencies the shape of the NTD Ge spectra is closer to the n-type Si spectrum than to the theoretically predicted spectra shown in Fig. 4.6. It is also found (Figs. 4.4 a and b) that the general behavior of the broad absorption maxima of these p-type NTD Ge samples is similar to that of theoretically predicted n-type Si spectra. This observation, together with the fact that there is no evidence for a sharp absorption peak, indicates that the presence of the d-like contributions in the Schechter envelope function are not as important as the theory predicted. The weaker contribution probably implies a smaller absorption coefficient. This is also consistent with the lower observed absorption than this theory predicts. The similar shape of the NTD

Figure 4.7 Comparison of the present absorption spectra for NTD Ge samples to that of the n-type Si sample with $N_d = 2.1 \times 10^{17} \text{ cm}^{-3}$, and $K=0.09$ as obtained by L. J. Neuringer *et al.*. Note that the absorption coefficient of the Si sample is enlarged by a factor of 10.



Ge and n-type Si spectra beyond the maximum absorption may indicate that the form of interactions (the energy overlap integral and quantum effects etc.) are similar at high frequencies. However, explaining the much higher absorption coefficient for p-type Ge may require more than simply using different parameters in the hydrogen-like envelope wavefunction to describe an acceptor. The correct order of magnitude of the absorption coefficients predicted by the theory of Kaczmarek et al. [8] indicates that the Schechter envelope wavefunction is a good starting point.

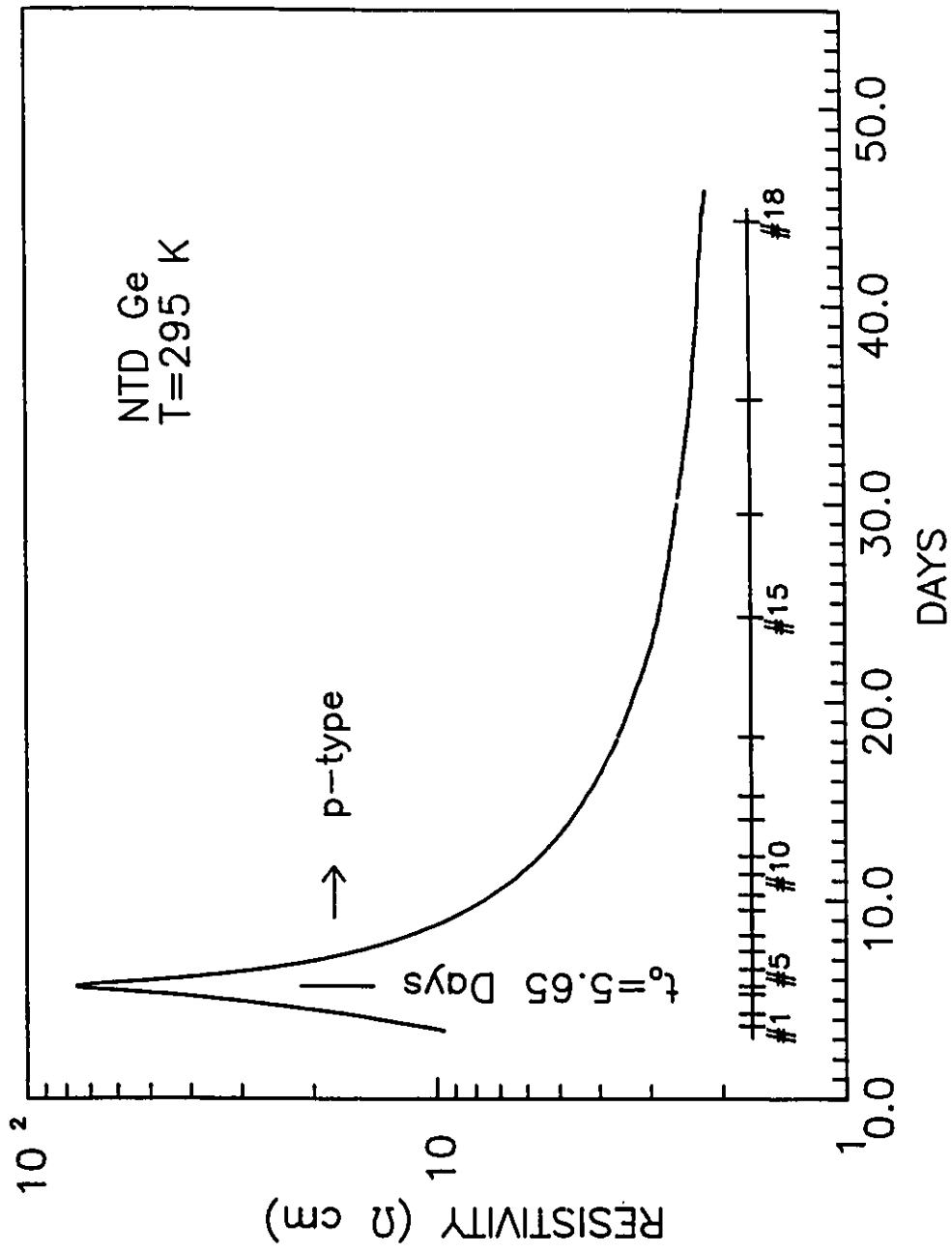
Considering the complexity of the problems, some failure of the theory is not really a surprise particularly at high frequencies where quantum effects become more important.

4.3 TIME DEPENDENT SPECTRA FOR NTD GE

This section presents the results of an investigation of the dynamical change of absorption due to the evolution of Ga impurities. This is accomplished by performing a series of time dependent absorption experiments shortly after irradiation of a sample. Sample S5, which was irradiated for 10 hrs., was used for this experiment.

In order to monitor the change of the sample, an extra sample was prepared simultaneously with S5 so that it could be used concurrently for a resistivity measurement. This measurement was done using a four point probe configuration [42] at room temperature. Fig. 4.8 shows the change of resistivity with respect to time for this sample. Zero time is defined as the time when the irradiation began. It is clearly seen that the resistivity of the sample first increases, and then peaks at $t_0 = 5.65$ days, followed by an asymptotic decrease to its steady-state value. As discussed in Section

Figure 4.8 The time dependent resistivity for NTD Ge. Note that the total compensation ($K = N_a/N_d = 1$) occurs at time $t_o = 5.65$ days. The unit of the resistivity shown is not absolute.

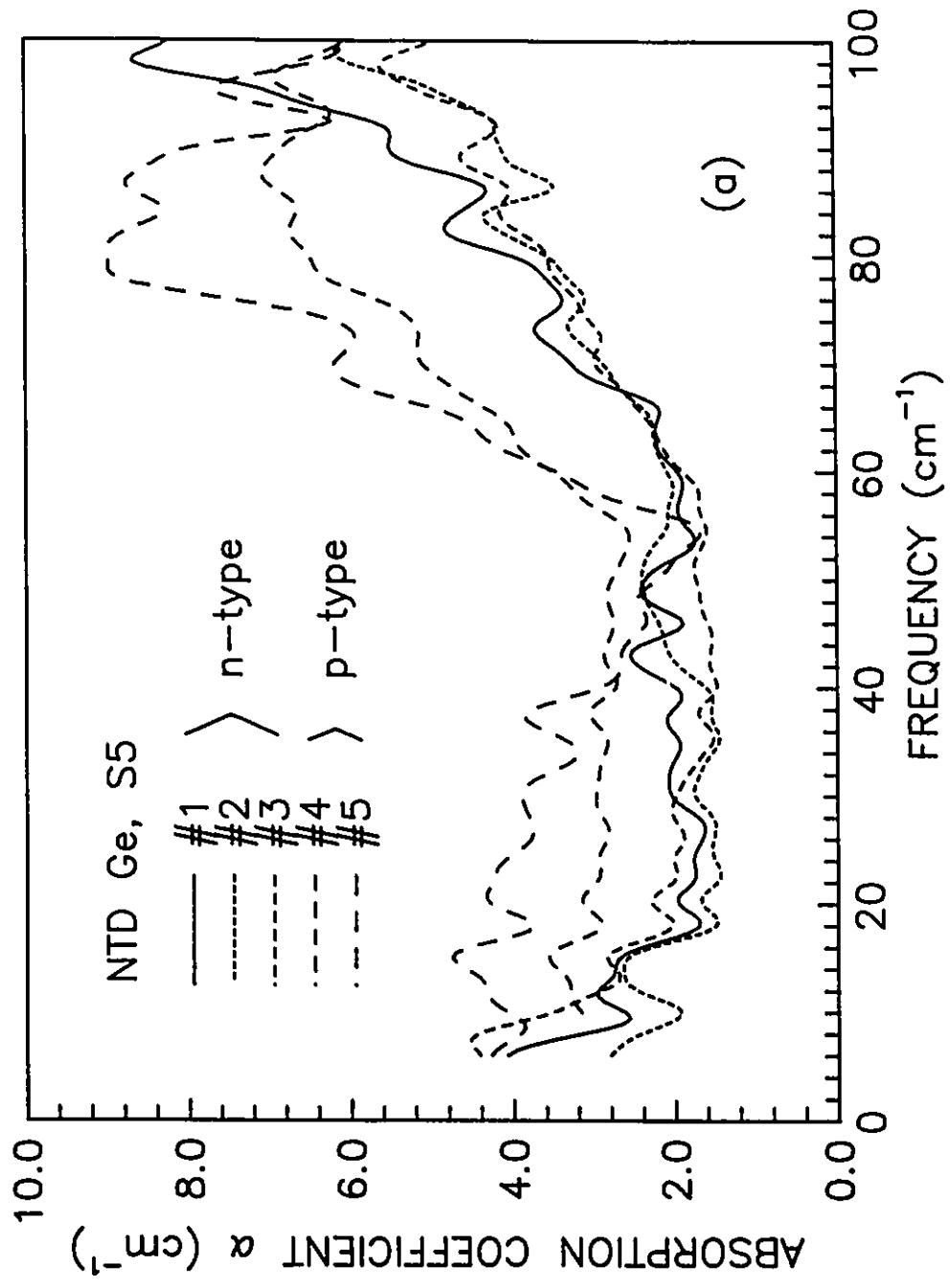


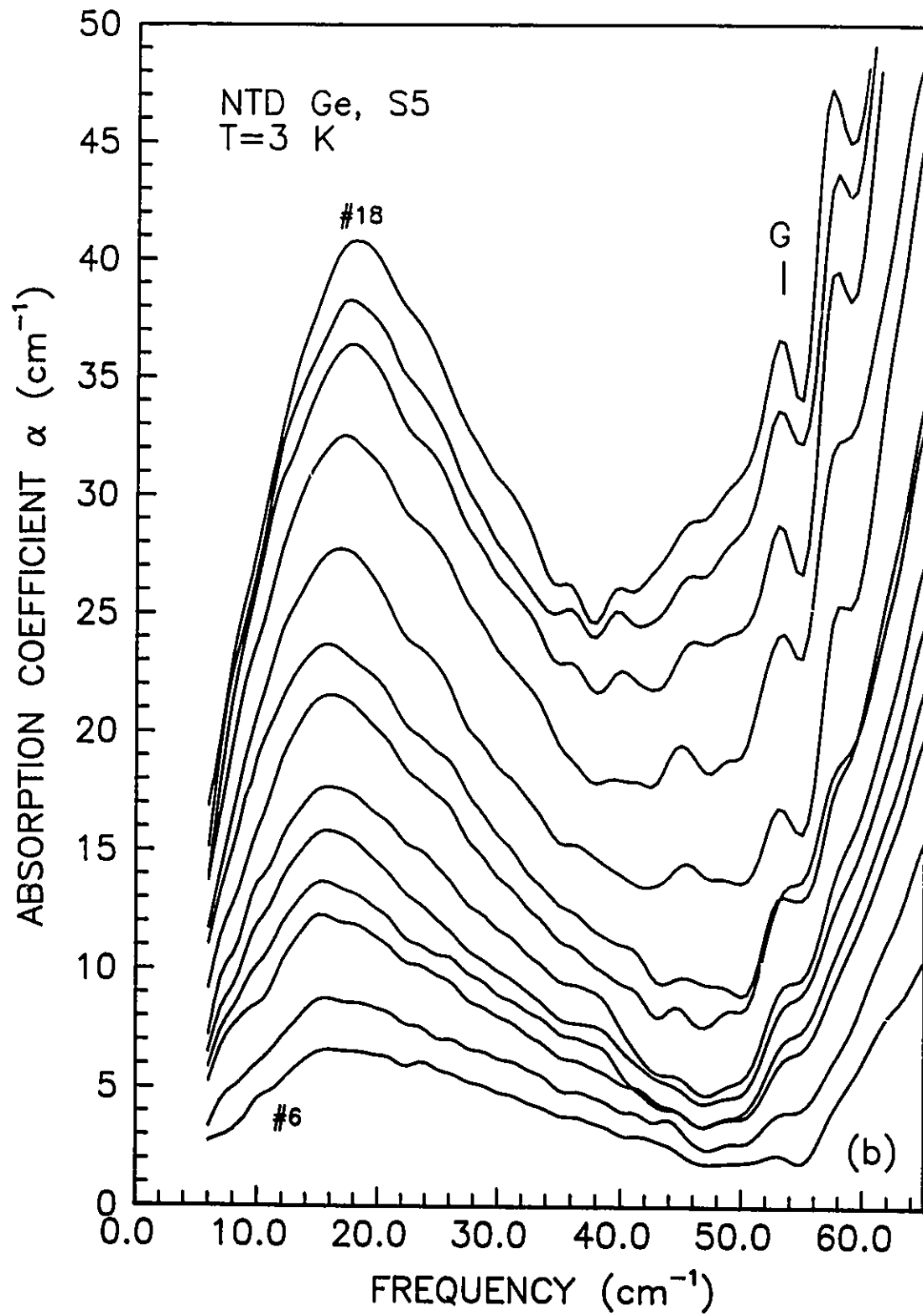
3.2, the donor concentration, N_d , reaches its saturated value shortly after the irradiation, and the sample is n-type for $t \leq t_0$. During this period of time, the Ga acceptor will act as a minority impurity and its increasing concentration, N_a , will effectively decrease the number of electron carriers which are mainly contributed by the donor. Therefore, the resistivity of the sample will increase as more Ga is created until it reaches a maximum resistivity at which $N_a = N_d$. This occurs at time $t = t_0$ as shown in the figure. After t_0 , the Ge sample becomes p-type, and the resistivity starts to decrease because the number of hole carriers, due to the increasing Ga impurity increases.

Using the decay half-life of 11.2 days for Ga and $t_0 = 5.65$ days, the concentration of Ga at t_0 can be found from Eqn. (3.3b). The compensation ratio, which can be obtained from $N_a(t_0)/N_a(t \rightarrow \infty)$ because $N_a(t_0) \approx N_d(t \rightarrow \infty)$, is found to be 0.286. This is in good agreement with previous results [28].

The series of absorption experiments are numbered in Fig. 4.8. Figure 4.9a shows the absorption spectra of experiment nos.1 to 5. The absorption spectra nos.1 to 3 are obtained at the times 3.7, 4.3, and 5.3 days. The sample is n-type when these three measurements were made. The concentration of donors is $6.2 \times 10^{15} \text{ cm}^{-3} (0.286 \times N_a)$, while the compensation, $K(t) = (N_a(t)/N_d)$, for these spectra is 0.68, 0.78, and 0.95 respectively. Spectra nos.4 and 5 are obtained at times 5.7 and 6.5 days, shortly after the sample is converted to a p-type material at day 5.65. The compensation, $K(t)$, for these two spectra is 0.99 and 0.89 respectively with fixed N_d . It is clear that the far-infrared absorption for n-type Ge differs appreciably from that of p-type. For instance, the absorption above 50 cm^{-1} , is mainly due to the transition from the ground state to excited states of an impurity. It

Figure 4.9 Time dependent absorption spectra for the NTD Ge sample S5. (a) Spectra nos.1 to 5 are presented in the region $0\text{--}100\text{ cm}^{-1}$. Note that there is a considerable difference between the n-type spectra (nos.1-3) and the p-type spectra (nos.4-5). (b) The spectra nos.6 to 18 are presented in the region from $6\text{--}65\text{ cm}^{-1}$.





should be noticed that the absorption due to the As impurity in spectra nos.2 and 3 is small compared to no.1. This is a result of the fact that more electrons are compensated by the increasing Ga concentration. When the sample turns p-type, the absorption of the impurity, which will be due to the Ga impurity, starts at lower frequencies ($\approx 55 \text{ cm}^{-1}$). This difference can be explained by the different absorption spectra of Ga and As impurities in Ge [39, 43]. The ionization energies for Ga and As are about 88.7 and 104.8 cm^{-1} respectively [33].

The absorption below 50 cm^{-1} is mainly due to photon-induced hopping of a charge carrier between impurity centers. In the spectra nos.1-3, the absorption is weak in the region between 20 and 60 cm^{-1} and starts to increase towards lower frequencies. Therefore, it is concluded that absorption due to photon-induced hopping in n-type Ge occurs mainly for frequencies below 10 cm^{-1} . As the sample turns p-type, the absorption suddenly increases for frequencies below 50 cm^{-1} and the maximum of a broad absorption starts to develop at a frequency above 10 cm^{-1} . This can be seen in Fig. 4.9b. Compared to the p-type Ge absorption spectra, the absorption for n-type Ge is much weaker and occurs at lower frequencies. These conclusions are in agreement with previous results [4, 5].

Figure 4.9b shows absorption spectra nos.6 to 18 which were obtained during the period between day 7.5 and day 44.3. The compensation, $K(t) = (N_d/N_a(t))$, varies from 0.79 to 0.31 respectively. This figure shows an increasing absorption coefficient, wherein the position of the maximum absorption shifts to higher frequencies with respect to the time. These changes result from the increasing Ga impurity concentration.

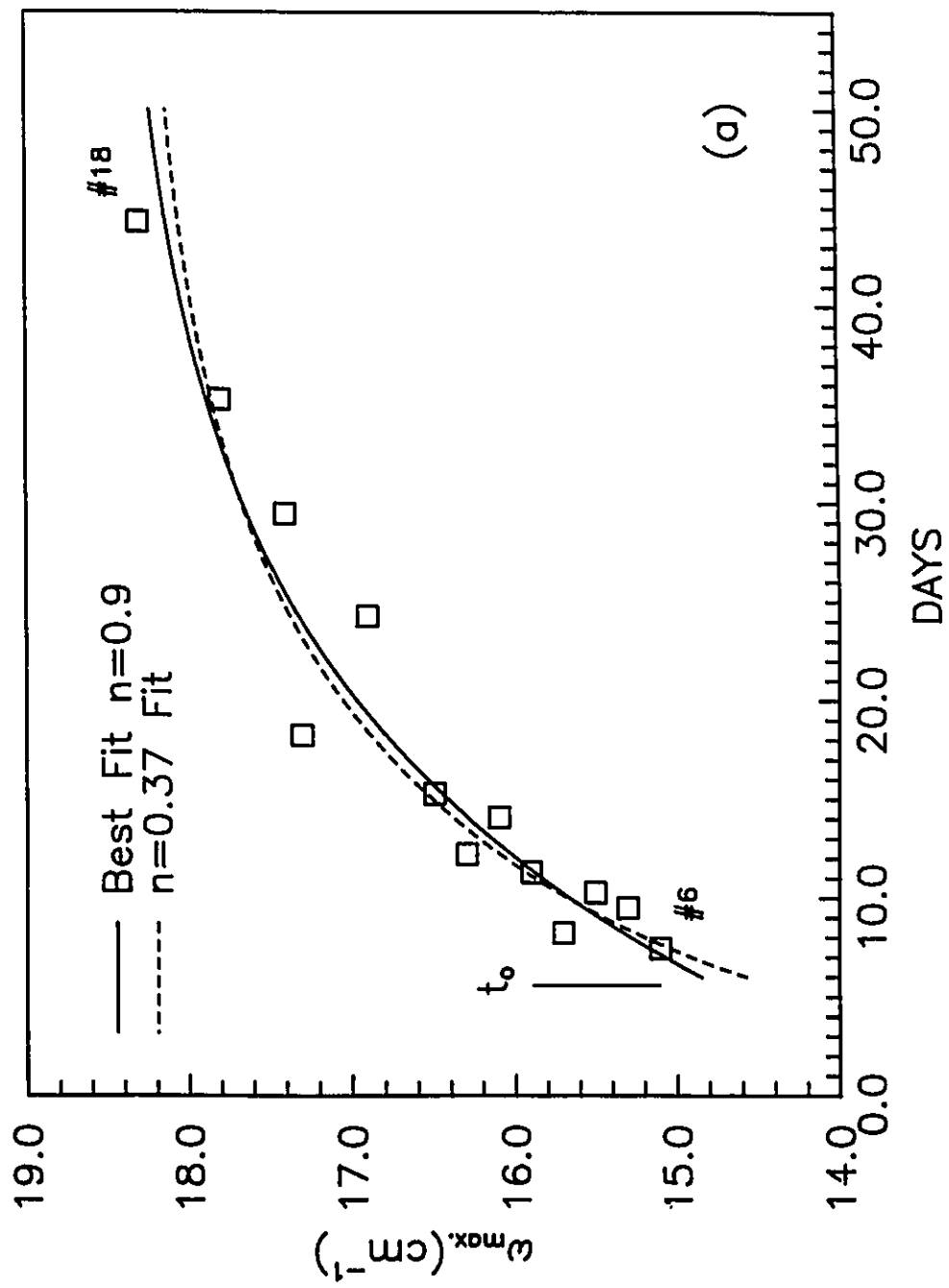
A series of graphs shown in Fig. 4.10 illustrate the changes in the absorption properties with respect to the time. The plotted data shown in these figures are obtained only after the broad absorption peaks of spectra nos. 6 to 18 are fit to a polynomial function. These changes in the absorption properties are due to the time evolution of Ga in the sample. That is, the changes correspond to the change of the majority impurity concentration, N_a , for a fixed minority concentration. To see how the absorption properties change with respect to N_a , these results are treated in a manner similar to those in Section 4.2, whereby various results are least-squares fit to the power-law function $y = a(N_a)^n + b$, where N_a is first obtained using Eqn. (3.3b) with a half-life of 11.2 days. It is found that the power dependence on N_a of ω_{\max} , $\alpha(\omega_{\max})$, $d\alpha/d\omega|_{\text{low } \omega}$, $\alpha(30\text{cm}^{-1})$ and the total absorption is 0.9, 0.48, 0.19, 0.98 and 0.84 respectively as shown in Fig. 4.10.

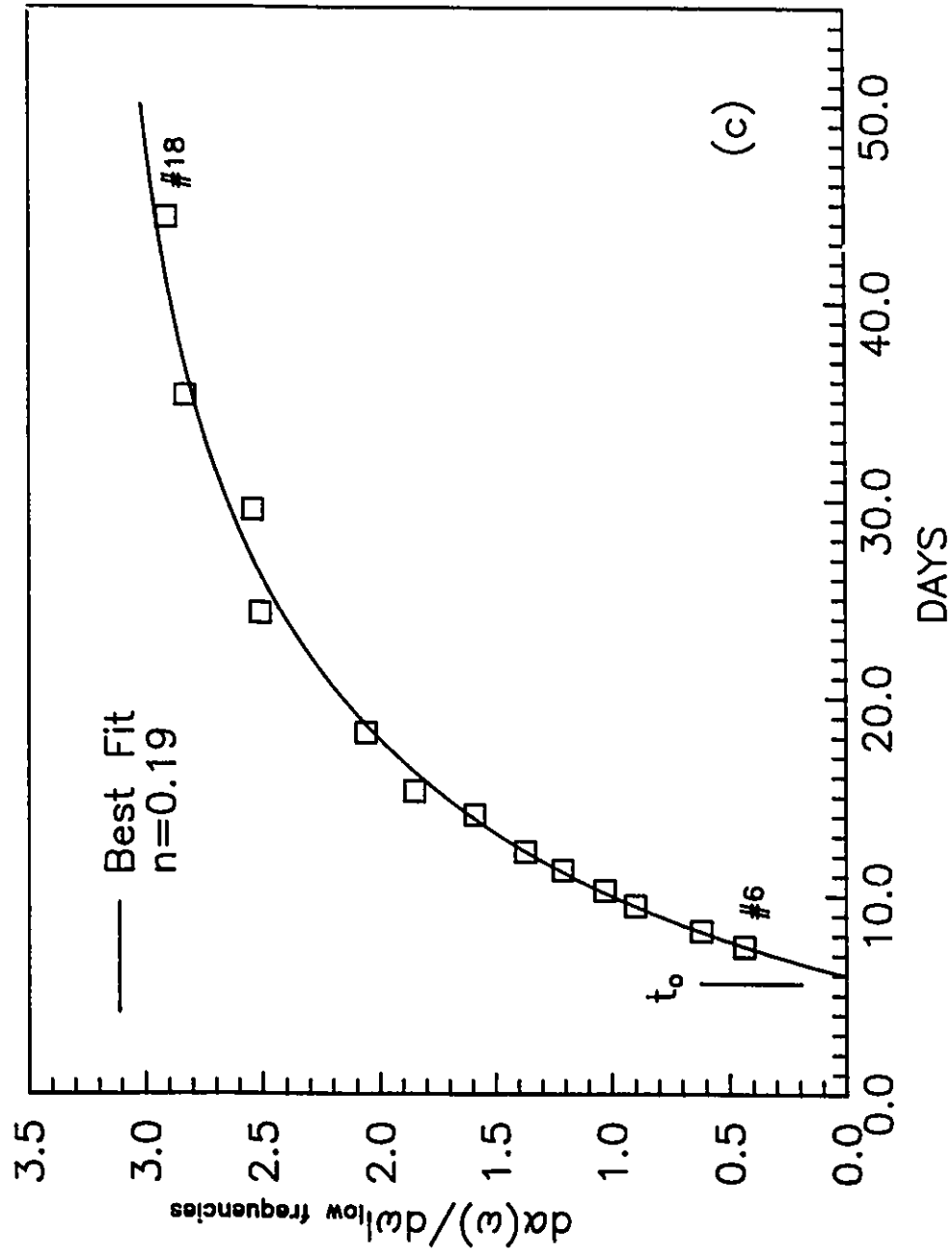
The differences between the absorption characteristics of samples with different impurity concentrations, but with the same compensation and those with different majority impurity concentrations, but with fixed minority impurity concentration are shown in Table 4.3. The $\alpha(\omega_{\max})$, $d\alpha/d\omega|_{\text{low } \omega}$, $\alpha(30\text{cm}^{-1})$ and the total absorption are all related to the absorption coefficient of the sample. The power factor of these properties on impurity concentration in samples with different concentration but fixed compensation is higher than that of the samples with fixed N_a and varied N_a . The differences are 0.83, 0.81, 0.88, and 0.84 respectively. All of these differences involve a factor close to one. According to the Blinowski and Mycielski theory, the absorption is proportional to the concentration of the minority impurity for $K < 0.2$. Therefore, the difference between the values of the power, n , needed

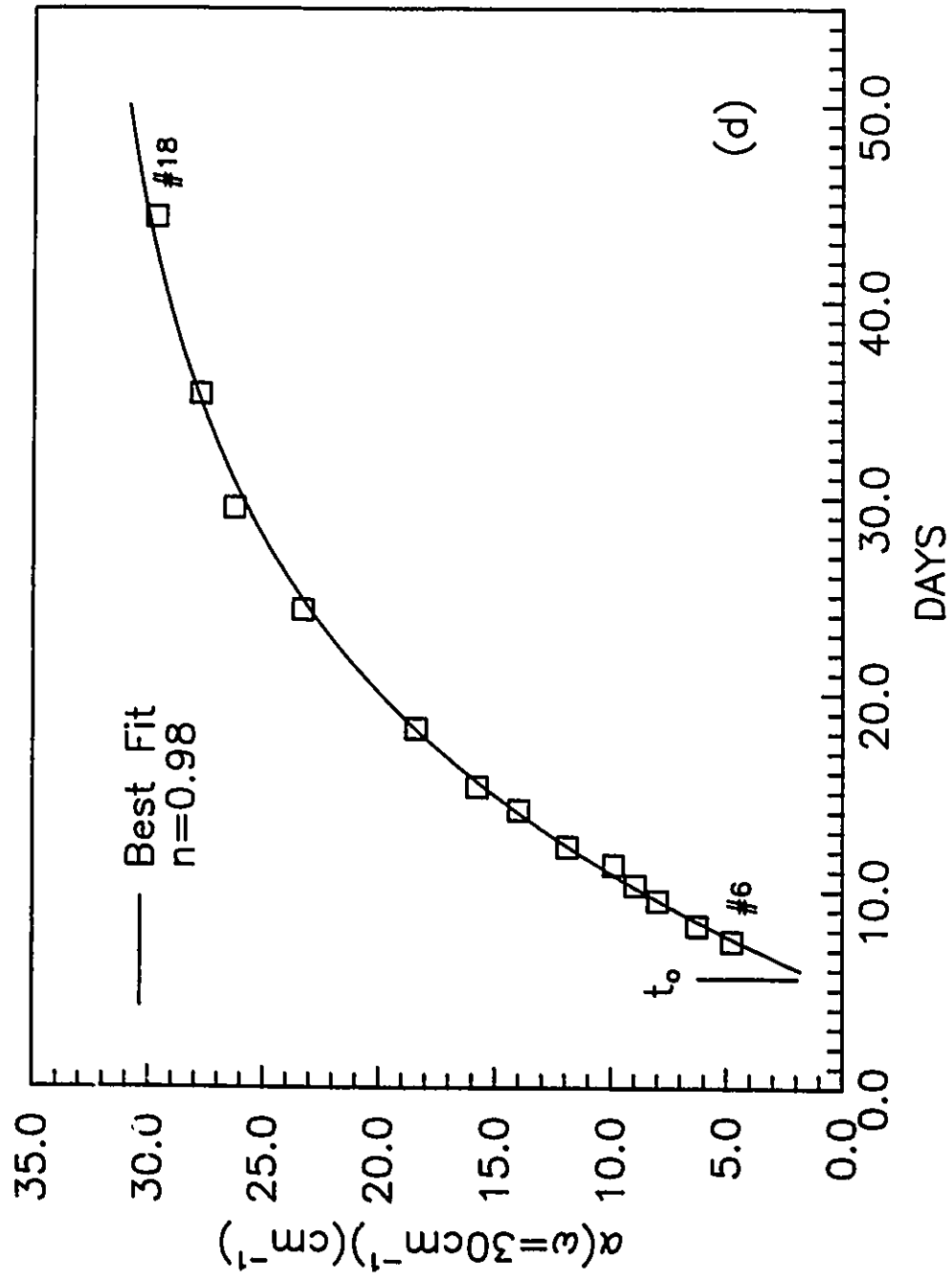
to fit the data describing $\alpha(\omega_{\max})$ of the broad absorption should be one because in one case N_d is fixed and for the other case N_d varies as KN_a . The present experimental value is 0.83. Similarly, if $f(K)$, in Eqn. (2.18a), is independent of K , then a difference of one in the value of n should also be obtained for the dependence of the slope of the spectra as $\omega \rightarrow 0$ and for the absorption at high frequencies. (see Eqn. (2.19)). The present results are 0.81 for $d\alpha/d\omega|_{\text{low } \omega}$ and 0.88 (evaluated at 30 cm^{-1}) respectively. It is clear that the assumption that the function, $F(\Omega, r)$, depends only linearly on the minority impurity concentration and that $f(K)$ is independent of K cannot hold for the time dependent absorption spectra because K is always larger than 0.286. Thus, the present results support the theory based on the localized pair model.

According to Eqn. (2.20), the frequency at which the maximum of the absorption occurs depends only on the majority impurity concentration. This implies that the dependence of N_a on the maximum should be the same for these two types of absorption spectra. However, there is large uncertainty involved in the results for the time dependent spectra as shown in Fig. 4.10a. For instance, the best fit line with $n=0.9$ is not much better than the fit with $n=0.37$ as shown in Fig. 4.10a. No conclusion can be made for the frequency of the absorption maximum from these results.

Figure 4.10 General properties of the absorption spectra in Fig. 4.9b versus time: (a) the frequency of maximum absorption, ω_{\max} , (b) the absorption coefficient at the maximum, $\alpha(\omega_{\max})$, (c) the slope of the spectra at low frequencies, $d\alpha/d\omega|_{\text{low } \omega}$, (d) the absorption coefficient at 30 cm^{-1} , $\alpha(30 \text{ cm}^{-1})$, and (e) the estimated total absorption due to the photon-induced hopping process. Data are least-squares fit with the function $y = a(N_s)^n + b$. The time at which the sample is totally compensated is denoted by t_o in these graphs.







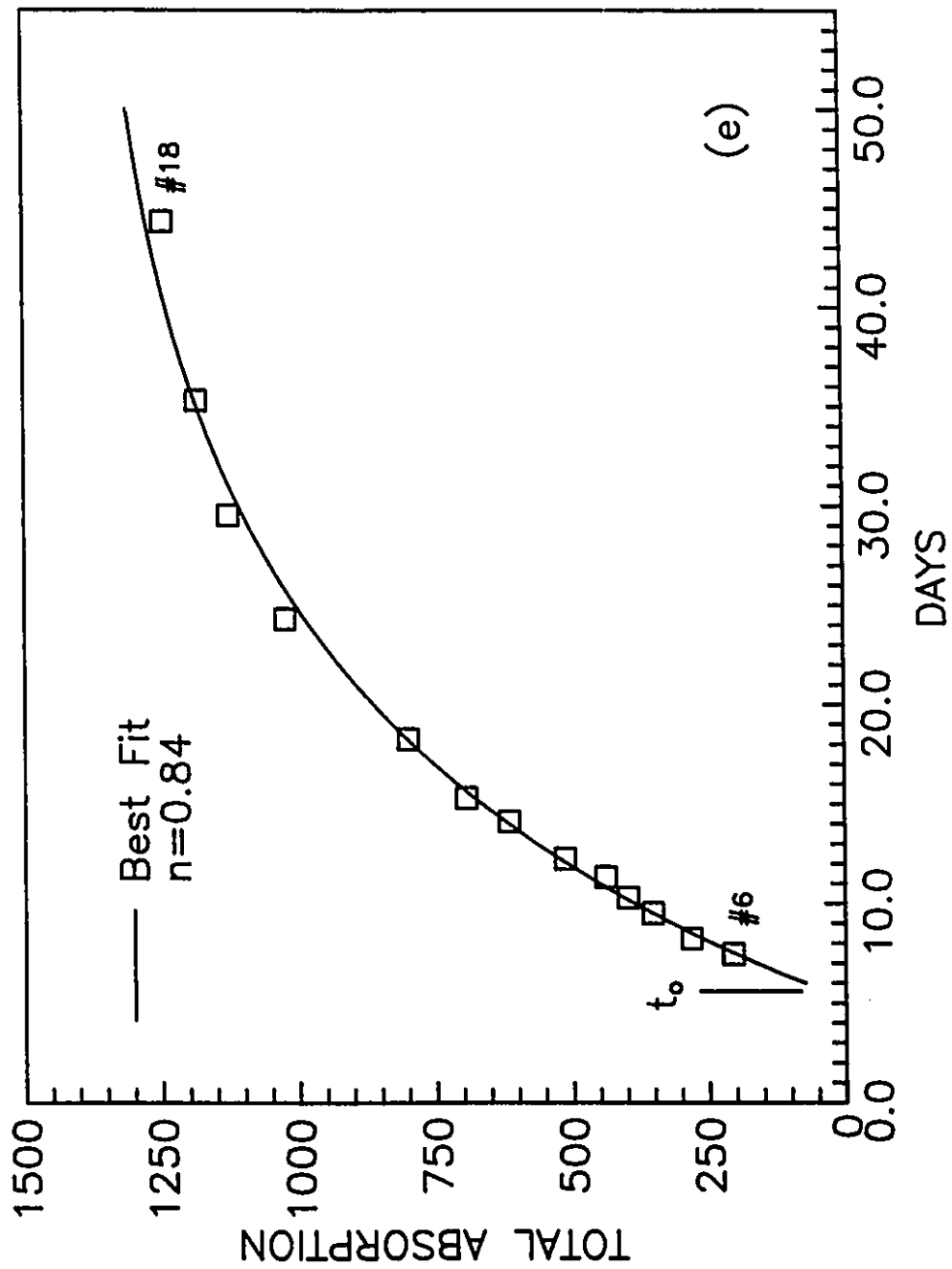


TABLE 4.3. Properties of Absorption Spectra for NTD Ge

N_a^n	ω_{\max}	$\alpha(\omega_{\max})$	$d\alpha/d\omega _{\text{low}\omega}$	$\alpha(30 \text{ cm}^{-1})$	Total absorption
n, (K=fixed)	0.37	1.31	1.00	1.86	1.68
n, (N_d =fixed)	0.9(?)	0.48	0.19	0.98	0.84
Difference	-0.53(?)	0.83	0.81	0.88	0.84

4.4 CONCLUSIONS

In this chapter, far-infrared absorption of photon-induced hopping in compensated p-type Ge at 3 K has been presented for samples prepared by neutron transmutation doping. Two types of experiments were performed. In the first, the change in absorption due to different carrier concentrations with fixed compensation (found to be 0.286 from the time-dependent resistivity measurement) was investigated. The spectra for samples with $(N_a - N_d)$ ranging from 2.3 to $26 \times 10^{15} \text{ cm}^{-3}$ show a broad absorption with the maximum occurring at a frequency between 10 and 24 cm^{-1} . The absorption coefficient of this maximum ranges between 2 and 87 cm^{-1} . Such absorption is negligible for the sample with $(N_a - N_d) = 1.3 \times 10^{15} \text{ cm}^{-3}$. In the second, the time dependence of the absorption spectra due to the evolution of the Ga impurity was investigated. The absorption and the frequency of its maximum increase asymptotically with respect to time. The maximum absorption changes from 6.5 to 40 cm^{-1} and the frequency of its maximum changes from 15 to 18.3 cm^{-1} during the post-irradiation period from day 7.5 to 44.3.

From the results of the far-infrared absorption experiments, it is clear that the overall behavior is consistent with the theory based on the localized

model. For instance, (i) the absorption coefficient increases with increasing impurity concentration, and (ii) there exists a broad absorption peak whose maximum shifts to higher frequencies as the majority impurity increases.

A power-law function fit was used to characterize the general behavior of the experimental spectra due to a change in the majority impurity concentration. The values of the powers derived from the experimental spectra, in general, agree with those obtained from theory. For example, the experimental results derived from samples with different impurity concentrations, but with fixed compensation show that the frequencies of, and the absorption coefficient at, the absorption maxima varies with the majority impurity concentration as $N_a^{0.37}$ and $N_a^{1.31}$. These values are close to the values $N_d^{0.41}$ and $N_d^{1.36}$ obtained from the numerical calculation for n-type Si spectra based on the Blinowski and Mycielski theory. The slope of the low frequency spectra varies as $N_a^{1.0}$ at $T=3$ K which is to be compared with the theoretical result $N_a^{4/3}$ obtained at zero frequency and $T=0$ K. Also, the absorption at 30 cm^{-1} varies as $N_a^{1.86}$ which is compared to the theoretical result of N_a^2 at high frequencies.

Similarly, the results derived from the time dependent absorption experiments can be fit to the power-law function. The time dependent Ga concentration is calculated from the known decay process. In this case, the absorption spectrum changes due to the increasing majority impurity (Ga) concentration (N_a). Comparing the power dependence on N_a of $\alpha(\omega_{\max})$, $d\alpha/d\omega|_{\text{low } \omega}$, $\alpha(30\text{cm}^{-1})$ and the total absorption to the fixed compensation case, shows that these dependences on N_a are approximately smaller by a power of one. This indicates that the absorption coefficient is almost proportional to the concentration of minority impurities because $N_d (= KN_a)$

is fixed in this case. Once again, this conclusion agrees with the Blinowski and Mycielski theory based on the localized pair model (see $F(\Omega, r)$ in Eqns. (2.13)). It is interesting to note that the power-law functions are fit to the time dependent absorption spectra whose compensation ratio varies from $K = 0.8$ to 0.3 . The function $F(\Omega, r)$ in this case is no longer simply proportional to the minority impurity concentration because $K > 0.2$. This may explain, in part, why the differences in the power "n" are consistently smaller than one for those properties related to the absorption as shown in Table 4.3.

The present spectra are in agreement with previous NTD Ge absorption experiments performed by Vavilov *et al.* for frequencies below 10 cm^{-1} . However, at high frequencies, a discrepancy exists between the two works. The absorption coefficient of the present spectra is higher than that of Vavilov *et al.* for frequencies above 10 cm^{-1} .

A comparison of these results with the theory of Kaczmarek *et al.* for p-type materials shows reasonable agreement at low frequencies but even at these frequencies the predicted absorption coefficient is somewhat too high. However, this agreement is still quite impressive considering of the fact that their theory does not involve any adjustable parameters. The agreement is mainly due to the use of the Schechter envelope functions instead of hydrogen-like functions to describe the ground state of an acceptor. At high frequencies, there are several discrepancies between their theory and the present results. The general shapes of the spectra are different; specifically, the predicted sharp peak is not observed. Part of the difference may be due to the inadequate description of a hole situated in an intermediate distance from an acceptor as a result of using the Schechter envelope function.

Hence, the present work certainly confirms the previous conclusions that the absorption coefficient for p-type Ge is much higher and that its maximum occurs at higher frequencies than that of n-type Ge. However, this work cannot agree with the previous belief that the dependence of the absorption coefficient on frequency is less pronounced for p-type than for n-type Ge. In fact, when the present p-type Ge absorption spectra are compared with the n-type Si spectrum obtained by Milward *et al.*, it is concluded that the general shape of the spectra is quite similar although n-type Si has a much weaker absorption and the absorption is at higher frequencies. It is speculated that at the high frequency region, the interactions between p-type and n-type impurities are very similar. It is noted that in this region the theory for p-type materials based on the Schechter function, does not agree with the experimental results. Similarly, the theory for n-type materials based on the hydrogen-like function does not agree with the experimental results discussed in Section 2.4. The discrepancies in both cases between theoretical and experimental results may have the same origin: the fact that quantum effects cannot be ignored in the high frequency region. Quantum effects may also play a common role in both n- and p-type absorptions at high frequencies.

A linear function is fit to the low frequency region of the spectrum. The absorption coefficient at $\omega = 0$ is extrapolated from the linear fit. It is found that this value is consistent with the value obtained from the d.c. resistivity measurement. It is concluded that the absorption is approximately proportional to frequency in the low frequency region. This simple linear relationship between the absorption coefficient and the frequency is quite surprising. Some possible explanations are pointed out: (i) the dependence

of r_ω on frequency is weak at low frequencies, and (ii) this linear behavior may be due to the existence of the Coulomb gap which limits the density of states at low energies.

It is clear that the understanding of the interactions in disordered systems is still far from complete. Far-infrared absorption experiments can certainly contribute to the understanding of certain aspects of such complex systems. Based on the results of this research, it is clear that some work on describing the interactions between acceptors is needed although the Schechter envelope function is certainly a good starting point. Further theoretical investigations are needed to include the quantum effects which are important at high frequencies. Further absorption experiments for frequencies below 5 cm^{-1} , which is the low frequency limit of the present work, would be useful to confirm the proposed linear relationship. If this simple linear relationship is confirmed, then its understanding may provide some insight into the fundamental nature of these systems.

Chapter 5

Photothermal Ionization Spectroscopy of Selectively Boron-Doped $\text{Ge}(x)\text{Si}(1-x)/\text{Si}$ Strained-layer Heterostructures

5.1 INTRODUCTION

Recent progress in high-quality epitaxial growth of $\text{Ge}_x\text{Si}_{(1-x)}/\text{Si}$ strained layers using molecular-beam epitaxy (MBE) has offered the possibility of achieving desirable optical and electronic properties for device applications [45]. It is well-known that at sufficiently low temperatures, most of the electronic properties of a semiconductor are determined by shallow impurities. Thus, a technique which may be used to analyze the composition of impurities as well as their properties is desirable. Optical spectroscopy is the best suited method for such an investigation because highly resolved spectra can identify different impurities in the samples. In addition, it is known that the dielectric constant, the anisotropic effective mass tensor and the band structure of a material are factors which play a significant role in

the description of the energy levels of an impurity. Therefore, the spectrum of the excited states of an impurity will provide a lot of information about the structure of a material. However, optical absorption spectroscopy cannot be used because of the negligible absorption of such a thin layer.

Photothermal Ionization Spectroscopy (PTIS) [46] is a powerful technique because it is both sensitive and spectroscopic. As will be briefly discussed in section 5.2, this technique is well suited for an investigation of impurities in a thin epitaxial film where the optical absorption is negligible. In addition, compensating impurities can also be detected by neutralizing them with band-edge light ($\hbar\omega > E_{\text{gap}}$). In this research, the possibility of using the PTIS technique to probe the shallow impurities in selectively B-doped $\text{Ge}_x\text{Si}_{(1-x)}/\text{Si}$ strained-layer heterostructures is demonstrated.

Three samples, S211, S222, and S210, obtained from N. R. C. [†], consisting of a $\text{Ge}_x\text{Si}_{(1-x)}$ layer sandwiched between undoped Si and heavily B-doped Si layers, were studied using PTIS. The samples' specifications are shown in Table 5.1. The general characteristics of selectively-doped heterostructures are introduced in section 5.3. The experimental set up used to perform the PTIS measurements is described in section 5.4. The PTIS spectra presented here are obtained under various experimental conditions: with and without band-edge light and by varying the temperature of, and voltage applied to, the sample. In addition, the transport properties; resistivity, carrier concentration, and Hall mobility of these samples are investigated. Since these measurements are not the main focus of this research only the salient features will be discussed in section 5.5. Sample S211 displays a two dimensional hole gas (2-DHG) [47] behavior at the $\text{Ge}_x\text{Si}_{(1-x)}/\text{Si}$ interface.

[†] National Research Council of Canada

This sample does not show a strong photoresponse. This is probably due to the number of photogenerated carriers being small in comparison with the number of residual hole carriers. Conversely, samples S210 and S222 show a strong photoresponse. As a result, the PTIS spectra discussed in section 5.6 will concentrate on these two samples.

TABLE 5.1. Structural Data for the Selectively B-Doped $\text{Ge}_x\text{Si}_{(1-x)}$ /Si Strained-Layer Heterostructures. The following layers were grown on $1\text{ }\mu\text{m}$ of undoped Si deposited on the n-type substrate.

Sample	Si(B) Layer	Si Layer	$\text{Ge}_x\text{Si}_{(1-x)}$ thickness	Si (nm)	Si(B)	x
S210 ^a	510	35	310	65	430	0.04
S211 ^b	150	15	92	25	120	0.087
S222 ^b	150	15	328	25	120	0.046

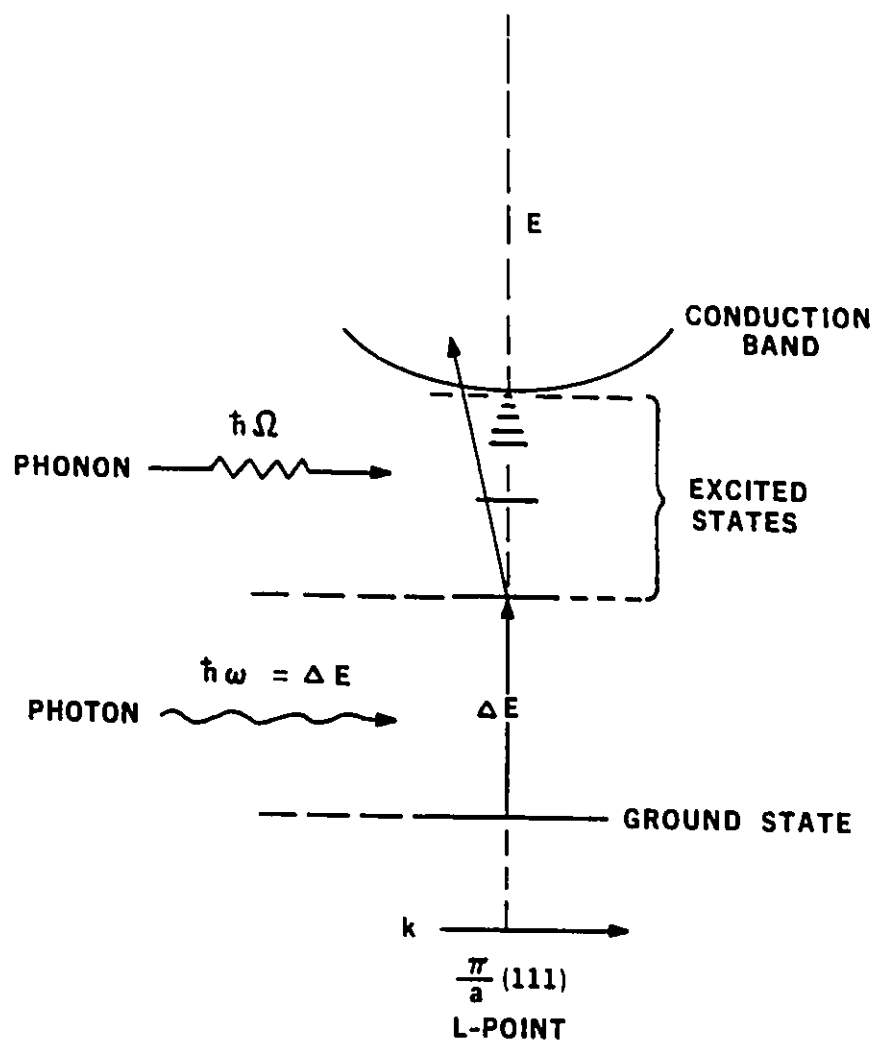
^a Boron dopant concentration $2 \times 10^{17}\text{ cm}^{-3}$.

^b Boron dopant concentration $5 \times 10^{17}\text{ cm}^{-3}$.

5.2 PTIS TECHNIQUE

What is the PTIS technique? The technique of PTIS involves the generation of sharp lines in the photoconductive (PC) response of a sample radiated by FIR radiation as the result of photothermal ionization (PTI) of an impurity. The PTIS measurement is performed at low temperature so that the impurity is not yet thermally ionized to an allowed band. For instance, the PTI spectra of boron (B) or phosphorus (P) impurities in Si are usually

Figure 5.1 The two-step ionization process which is the basis of PTIS. This figure was adopted from E. E. Haller for a donor impurity [48].

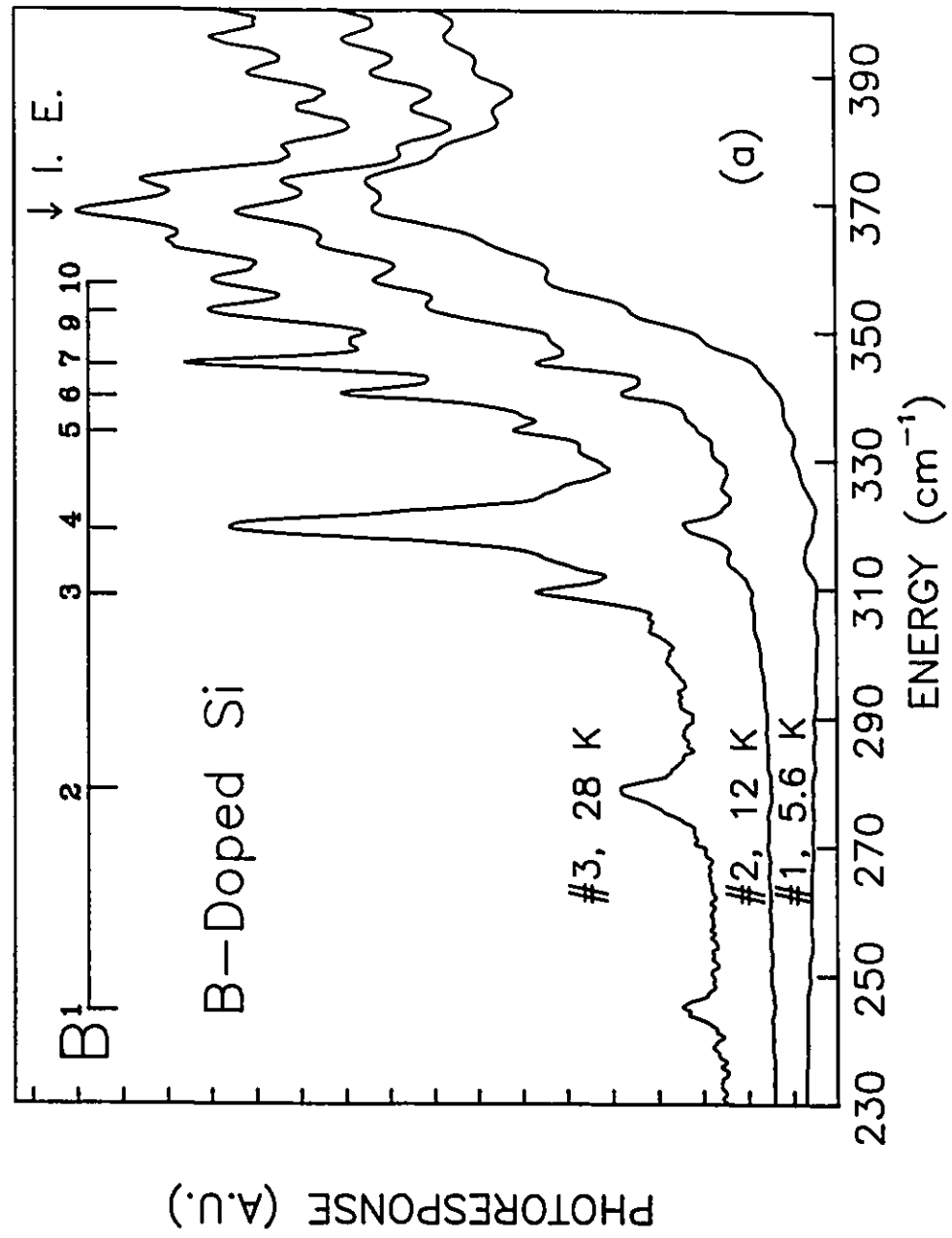


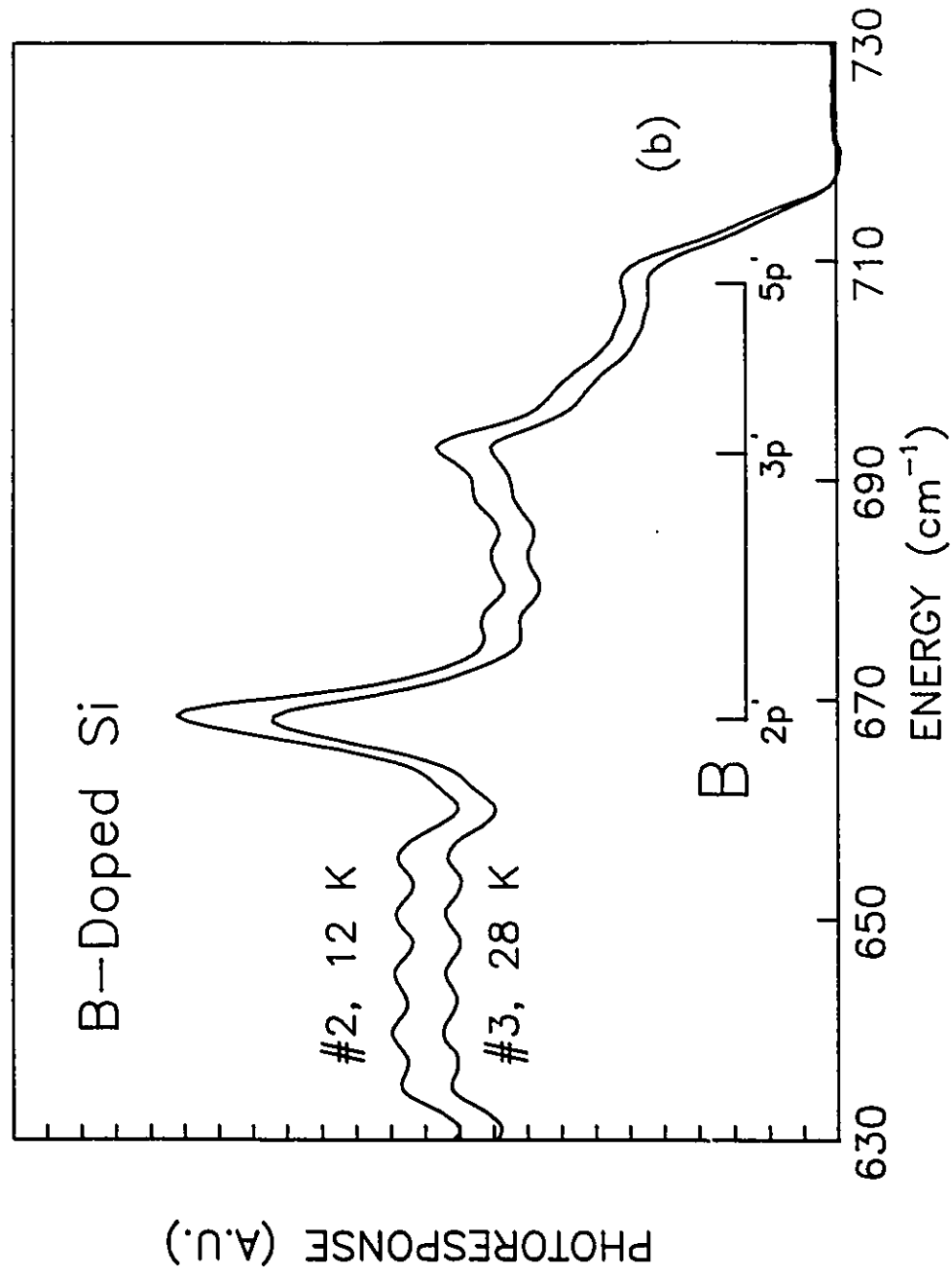
obtained at a temperature below 28 K. PTIS is a two-step process: the absorption of a photon causes the transfer of a bound electron or hole from the ground state to one of the excited states and this is followed by a transfer to an allowed band by the absorption of lattice phonons as illustrated in Fig. 5.1. This explanation is supported by the temperature dependence of the spectrum shown in Fig. 5.2a.

To demonstrate the PTIS technique, the Photothermal Ionization (PTI) spectra for a commercial grade B-doped Si wafer [†] are shown in Fig. 5.2a. The spectra were obtained at three different temperatures: 5.6, 12 and 28 K. Different voltages ranging from 2 volts to 10 volts have been applied to the sample with no significant change except in the overall signal level. At low temperature such as spectrum no. 1, the low excited states of the impurities do not show up. However, as the temperature increases, the low excited states appear and as the temperature increases further, the low excited states become more prominent as shown in spectrum no. 3. At low temperatures, only photon energies close to the ionization energy of the impurity will have a photoresponse. Holes in the low lying excited states have no photoresponse because there are few phonons available to excite the holes to the valence band. However, when the temperature is increased, more phonons are available and the excited electrons in low lying excited states have a higher probability of being excited by phonons to the valence band. Therefore, they will contribute to the photoresponse. The observed boron transition lines are due to the $P_{3/2}$ valence band and are found to be in agreement with results reported previously [49, 50].

[†] From a room temperature 4-point probe resistivity measurement, the net carrier concentration is estimated to be $|N_a - N_d| = 2 \times 10^{15} \text{ cm}^{-3}$.

Figure 5.2 PTI spectra for B-doped Si at various temperatures without band-edge light: no. 1 at 5.6 K, no. 2 at 12 K and no. 3 at 28 K. The energy region from 230 to 400 cm^{-1} is shown in (a). The observed peaks can be identified as the boron excited states from the $P_{3/2}$ valence band. The ionization energy (I. E.) of boron in Si is identified. The interference fringes which are especially visible in the region 375-400 cm^{-1} are due to multiple reflections of the FIR radiation in the parallel flat-surfaced sample. (b) The PTI spectra no. 2 and no. 3 in the region from 630 to 730 cm^{-1} are shown. The observed peaks can be identified as the boron excited states from the $P_{3/2}$ valence band. The PC signal fall-off at higher energy is due to the polyethylene cutoff filter and the strong absorption band in the Mylar beamsplitter at 725 cm^{-1} . The unit for the photoconductive response is arbitrary.



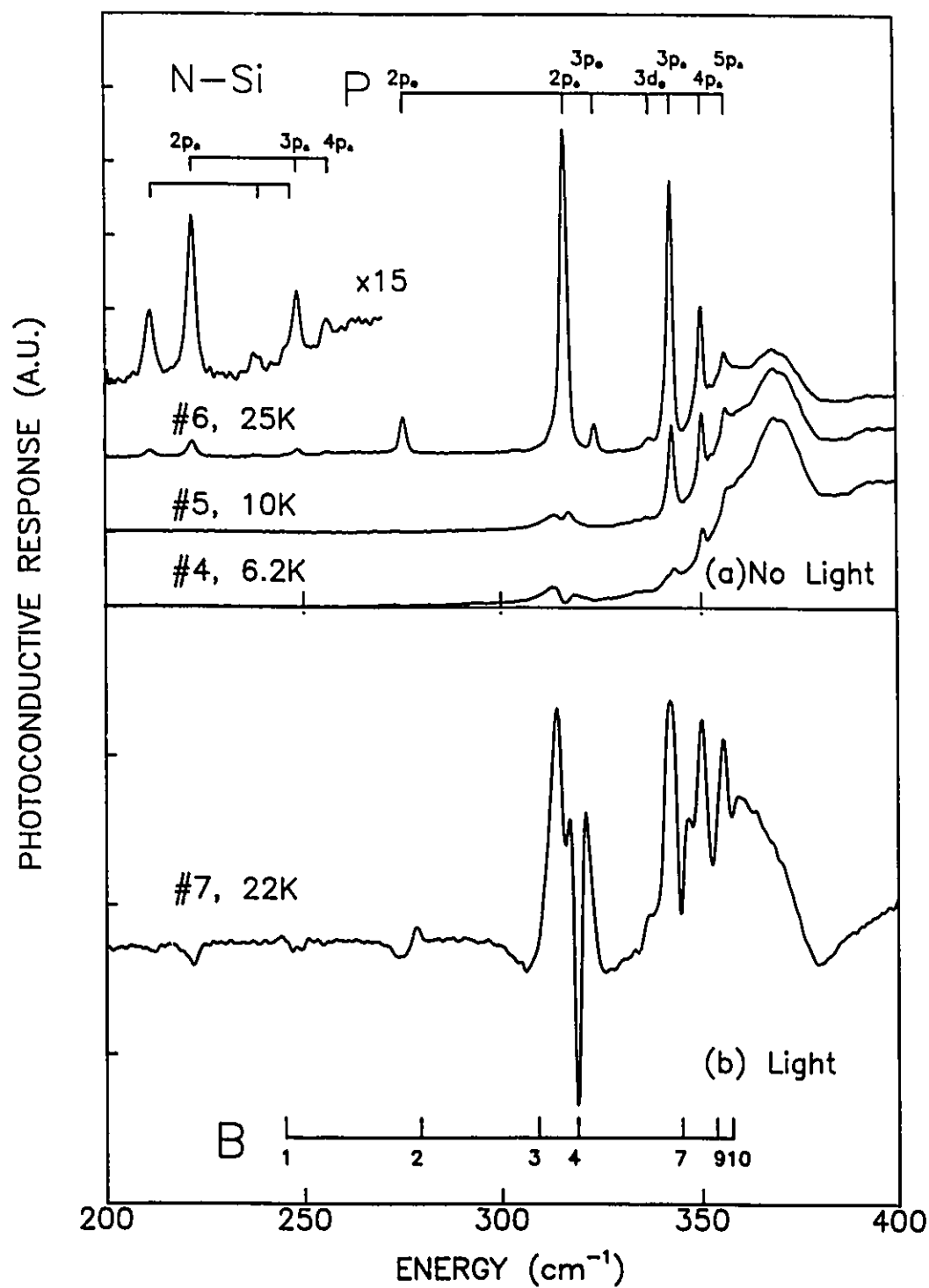


The photoreponse of spectra nos. 2 and 3 in the frequency region from 630 to 730 cm^{-1} is shown in Fig. 5.2b. It is found that the observed peaks in these spectra correspond to the excited states of the split-off $P_{1/2}$ valence band. The two lines labelled 2p' and 3p' are in agreement with previous absorption experiments [50]. Unlike the transition lines from the $P_{3/2}$ valence band, these lines are observed at low temperatures and their relative strengths are more or less temperature independent since a phonon is no longer needed to excite the excited hole into the valence band.

At this point, it may be useful to investigate the PTI spectrum of the n-type Si substrate which is used to grow the samples. The impurity concentration of the substrate is estimated from the room temperature resistivity measurement to be $(N_d - N_a) \approx 2 \times 10^{14} \text{ cm}^{-3}$. Fig. 5.3a shows the photothermal ionization (PTI) spectra of the substrate, obtained by removing the epitaxial layer, for three different temperatures. A comparison of spectrum no. 6 to the well-established spectra of impurity excited states found in bulk Si shows that the majority impurity is P [48, 50]. Weak peaks are observed in the spectral range extending from 200 to 270 cm^{-1} . Although, they may be identified as shallow donors, their origins are not fully understood.

At low temperature, all minority impurities are ionized. It is not possible to obtain a photoresponse from the ionized impurities. Therefore, the minority impurities cannot be observed in a PTI spectrum under normal conditions. However, when band-edge light is used to neutralize the ionized impurities, the photoresponse from the minority impurities can be observed [52]. The spectrum in Fig. 5.3b is obtained with additional illumination of the band-edge light for the same n-type Si substrate at a temperature of 22 K. It shows positive peaks which are identified as the P impurity states as in Fig.

Figure 5.3 Photoconductivity spectra for the n-type Si substrate. (a) The spectra are obtained at various temperatures, without band-edge light and applied voltages between 2 and 3 volts: no. 4 at 6.2 K, no. 5 at 10.0 K and no. 6 at 25 K. The expanded portion of no. 6 between 200-270 cm^{-1} shows the presence of two shallow donors. (b) The spectrum no. 7 is obtained in the presence of band-edge light at 22 K and an applied voltage of 0.5 V. The unit for the photoconductive response is arbitrary.



5.3a. However, there exist a series of negative peaks, which are usually associated with compensated impurities as reported previously [49, 52]. That is, in PTI spectra, the minority impurity usually appears as a negative PC response (i.e. negative photoconductivity). The cause of this phenomenon is not yet settled. However, it was first suggested that the enhancement of electron-hole recombination from the compensated carriers causes this effect [52]. Recently some alternate models have been developed for PTIS under band-edge light illumination [53, 54]. By comparing the known impurity transition lines with these negative peaks, it is concluded that the dominant minority impurity in the substrate is B. There is a strong photoresponse in the region between 310 and 320 cm^{-1} for which the origin has not been determined. Thus, through the use of band-edge light, the PTIS can probe both majority and minority impurities in a sample.

PTIS provides a very sensitive measurement of the excitation energies of various impurities in semiconducting materials. It has been shown [46] that the PTI response is proportional to the relative change of the carrier concentration [46], but not on the total number of photothermally ionized carriers. Therefore, its sensitivity does not depend on the concentration of impurities in the sample. PTIS can be performed on a sample with negligible absorption. In theory, impurity concentration as low as 1 impurity in 10^{16} atoms of Ge can be detected. Similarly, one can conclude that the photoresponse depends on the relative change of conductivity under FIR illumination, but does not depend on the thickness of the sample. Therefore, PTIS provides the opportunity to probe extremely thin films in which optical absorption is negligible. It has been used successfully to investigate impurities in n-type gallium arsenide epitaxial films grown on high-resistivity substrates [46]. Besides the

excellent sensitivity of the PTIS technique, it has been demonstrated that the highly resolved spectra can identify different impurities in the materials.

5.3 SELECTIVELY BORON-DOPED $\text{Ge}_x\text{Si}_{(1-x)}/\text{Si}$ STRAINED-LAYER HETEROSTRUCTURES

The samples have the usual physical structure of selectively doped single quantum wells [55]. These samples (S211, S222, and S210), which consist of a $\text{Ge}_x\text{Si}_{(1-x)}$ layer sandwiched between undoped Si and heavily B-doped Si layers, were grown on an n-type (100)-Si substrate. The samples' specifications are described in Table 5.1.

The $\text{Ge}_x\text{Si}_{(1-x)}$ strained layer has a smaller band gap than that of the Si layer [45]. The band-gap in the $\text{Ge}_x\text{Si}_{(1-x)}$ strained layer is determined by the Ge content, x , as shown in Fig. 5.4a. It has been shown that the band-gap discontinuity in the $\text{Ge}_x\text{Si}_{(1-x)}/\text{Si}$ interface occurs mainly in the valence band. If the acceptor energy in the Si layer is above the edge of the valence band of the $\text{Ge}_x\text{Si}_{(1-x)}$ layer, then the alignment of the Fermi levels in an equilibrium state requires that the holes diffuse from the Si to the undoped $\text{Ge}_x\text{Si}_{(1-x)}$ layer. This results in a negatively charged depletion region in the Si layer. At the interface, on the $\text{Ge}_x\text{Si}_{(1-x)}$ side, the transferred holes provide the positive charge required to balance the negative charge in the Si layer. The space charge localized near the heterojunction sets up a very strong electric field which in turn causes pronounced band bending, particularly in the $\text{Ge}_x\text{Si}_{(1-x)}$ layer. This is shown in Fig. 5.4b. Such strong band bending forms a quasitriangular potential well in the $\text{Ge}_x\text{Si}_{(1-x)}$ layer which will confine the holes. The effective thickness of the triangular potential well is substantially less than the carrier de Broglie wavelength. Consequently, the holes in this

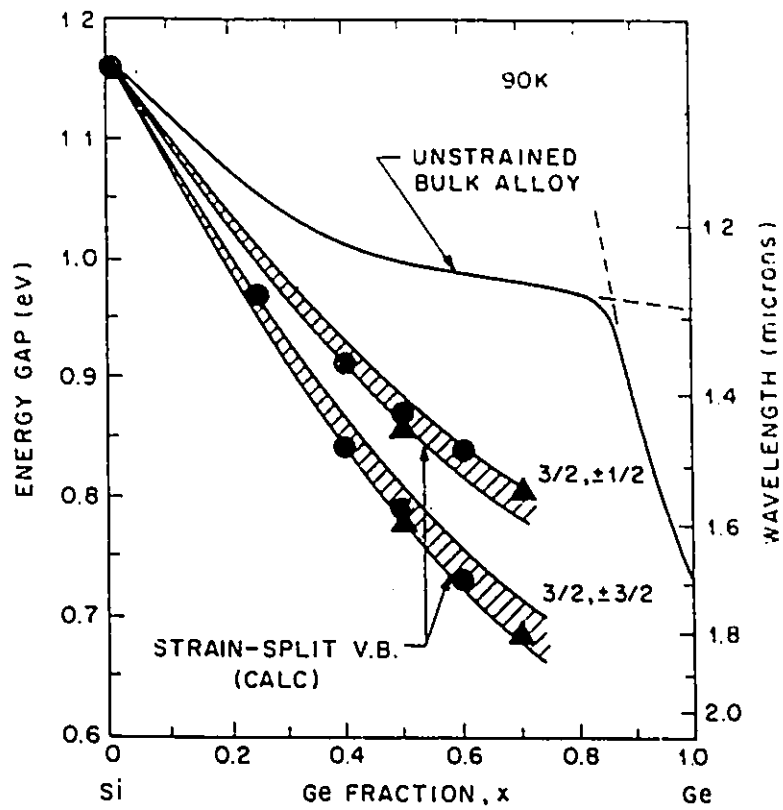
quasitriangular potential well will behave dynamically as a two-dimensional hole gas (2-DHG).

It has been observed that the hole mobility is greatly enhanced in selectively-doped heterostructures at low temperatures. It is known that ionized impurity scattering is the dominant limitation on carrier mobility, particularly at low temperatures. However, the hole carriers in the $\text{Ge}_x\text{Si}_{(1-x)}$ layer are spatially separated from the ionized acceptors in the Si layer by the undoped Si layer resulting in a significant reduction in ionized impurity scattering, thus improving low temperature mobility. It will be shown in section 5.5 that if the discontinuity in the valence band edge is sufficiently large, then the hole carrier concentration does not show the usual freezeout behavior of doped semiconductors at low temperatures. This is attributed to the existence of lower energy states in the $\text{Ge}_x\text{Si}_{(1-x)}$ layer than the boron energy states in the Si layer.

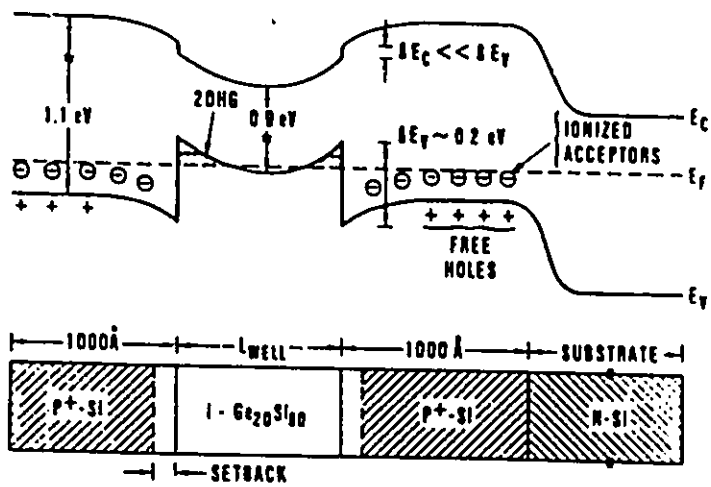
5.4 EXPERIMENTAL

In order to perform these measurements, it is necessary to attach ohmic contacts to the samples. This is achieved by evaporating two strips of metal onto the surface of the sample. The size of the gap between the strips is approximately 1.05 mm. Al contacts are used for the selectively B-doped $\text{Ge}_x\text{Si}_{(1-x)}$ /Si epitaxial layer and B-doped Si, while a Au-Sb alloy (with 0.1% Sb) contacts are used for the n-type Si substrate [33]. After evaporation, the sample is placed into a furnace preheated to approximately 200 °C. The temperature is then increased to 550 °C for the Al-Si contacts and 400 °C for the Au-Sb-Si contacts. After 10 to 15 minutes, the annealing process is

Figure 5.4 (a) The energy gap for the $\text{Ge}_x\text{Si}_{(1-x)}$ strained layer grown on a Si(001) substrate for different contents of Ge, x . The data was obtained at 90 K. The double points at the same x value correspond to a splitting of the upper ($J = 3/2$) valence band. The unstrained bulk alloy data are also shown. (b) Typical band diagram for selectively p-doped $\text{Ge}_x\text{Si}_{(1-x)}/\text{Si}$ strained-layer heterostructures having $x = 0.2$. Both diagrams have been adopted from a paper by R. People [45].



(a)



(b)

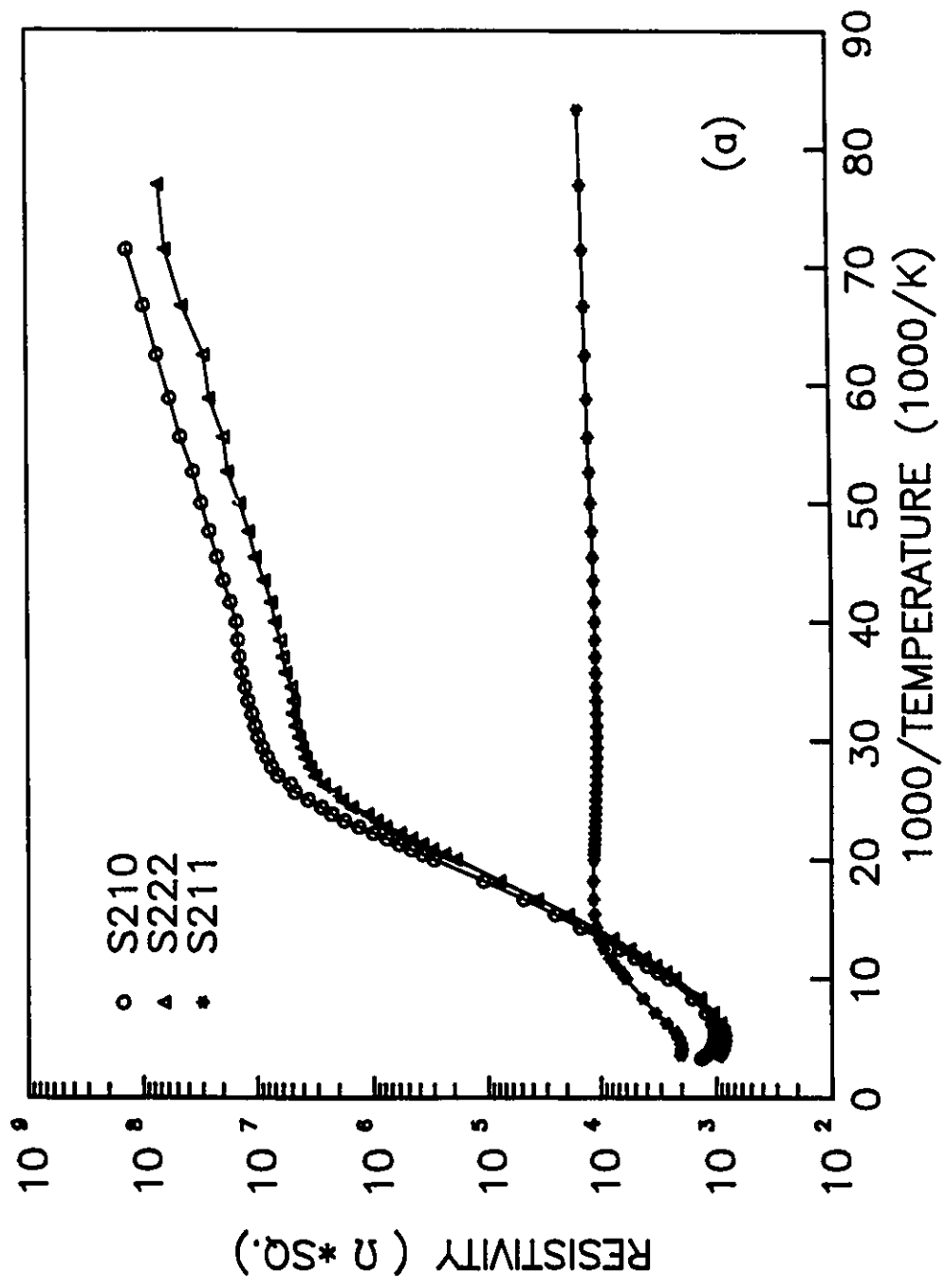
terminated by allowing the sample to cool to room temperature. The sample is exposed to flowing argon gas during the entire annealing process.

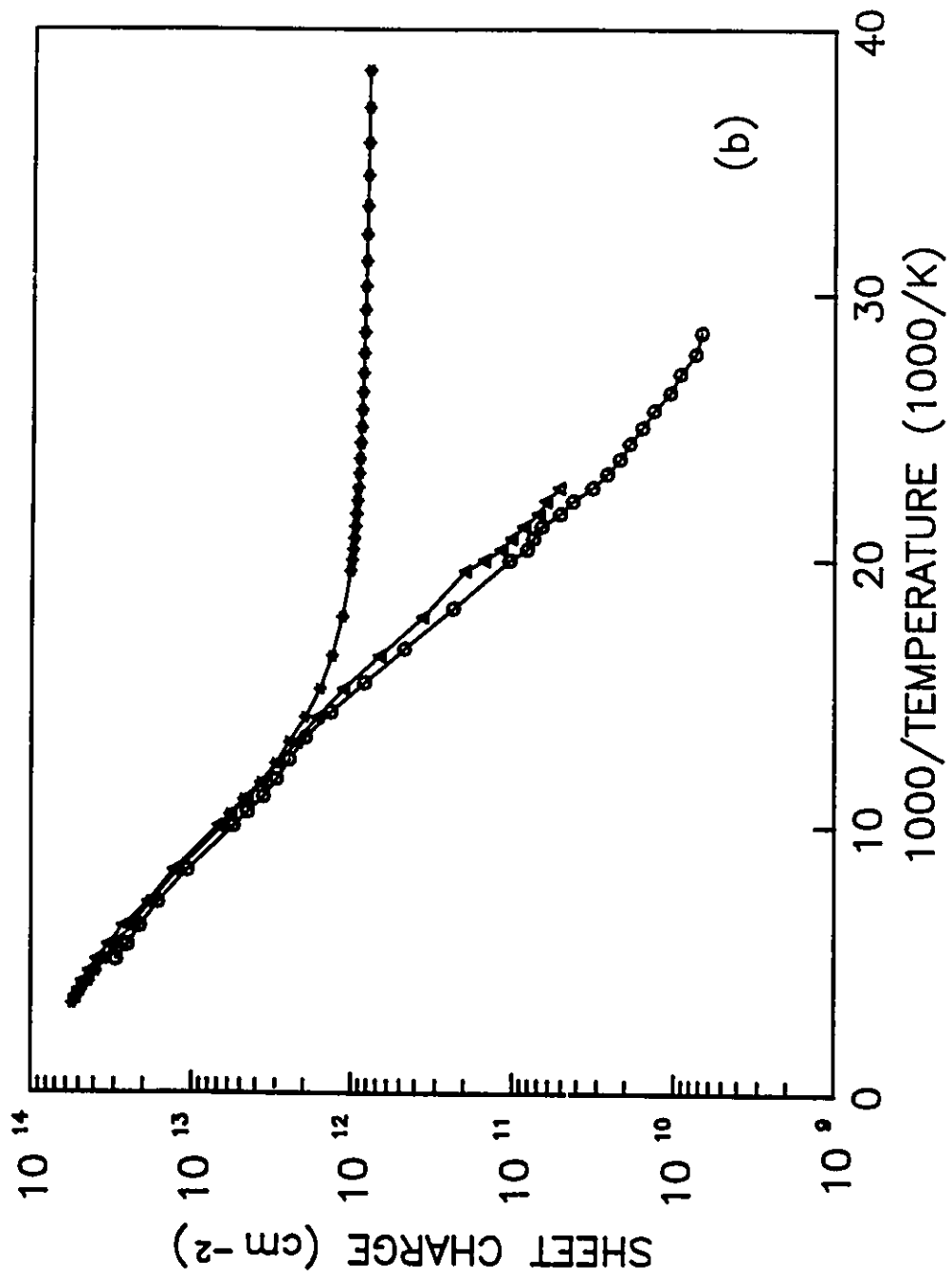
The PTIS spectra are obtained by using a far-infrared Michelson interferometer with a resolution of 1 cm^{-1} . The radiation leaving the interferometer enters a cryostat manufactured by Infrared Laboratories Inc. (see Fig. 3.2), wherein the bolometer is replaced by the sample being investigated. The light is focused onto the sample by a parabolic cone with an exit aperture of 2.2 mm. The light source and filtering are dictated by the experiment. The spectra without band-edge light are obtained using either a mercury-arc or a tungsten halogen lamp with an ac power supply in conjunction with a cold black polyethylene cutoff filter. When band-edge light is present, an unfiltered tungsten halogen light source with a dc power supply is used. The leads are attached to the sample with silver paint. The temperature of the sample is adjusted with a constantan wire heater. It is monitored with a silicon diode temperature sensor placed in thermal contact with the sample.

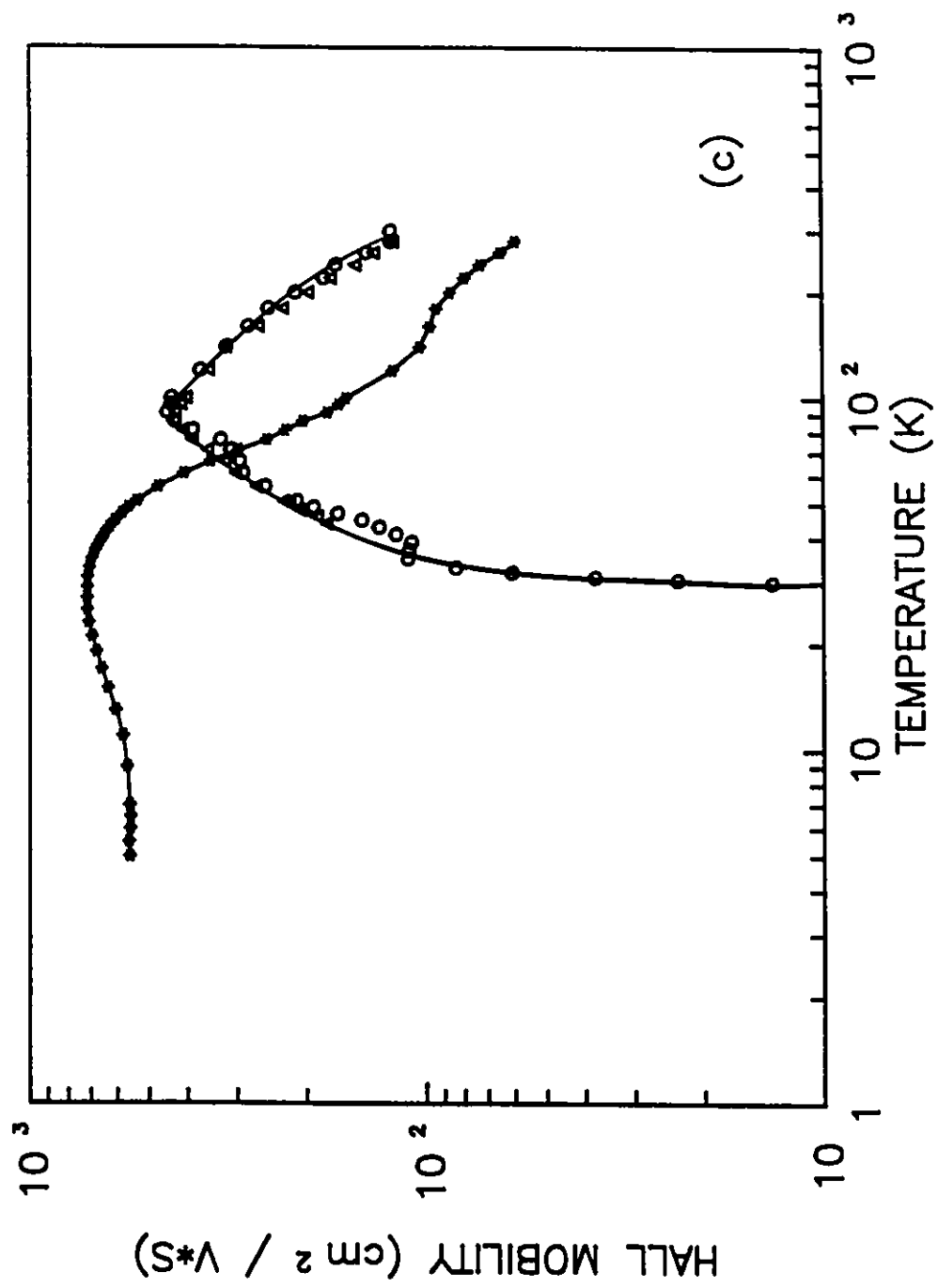
5.5 TRANSPORT PROPERTIES

The transport properties of these samples were investigated by Hall measurements using the standard van der Pauw technique. Fig. 5.5 shows the temperature dependence of the resistivity (a), sheet carrier density (b) and Hall hole mobility (c) of samples S210, S211 and S222. From this figure, it is evident that sample S211 exhibits, (i) a sheet carrier density which does not exhibit the usual freezeout behavior but instead saturates at a level of $6 \times 10^{11}\text{ cm}^{-2}$ at 4.2 K, (ii) a peak Hall mobility of $720\text{ cm}^2 \cdot \text{V}^{-1} \cdot \text{s}^{-1}$, which is anomalously high for a dopant level of 10^{18} cm^{-3} found in bulk Si, and (iii) the absence of a strong fall-off in mobility at low temperatures due to ionized

Figure 5.5 Transport properties for samples S211, S210 and S222: (a) resistivity vs $1000/\text{temperature}$, (b) sheet charge density vs $1000/\text{temperature}$ and (c) Hall hole mobility vs temperature. Note that only S211 demonstrates a 2-DHG behaviour.







impurity scattering. This behavior is consistent with the presence of a two-dimensional hole gas (2-DHG) at the $\text{Ge}_x\text{Si}_{(1-x)}/\text{Si}$ interface as discussed in section 5.3.

From the low temperature mobility of sample S211, it is concluded that its mobility is limited by $\approx 10^{16}\text{cm}^{-3}$ ionized impurities in the $\text{Ge}_x\text{Si}_{(1-x)}$ alloy layers [56]. At room temperature, the mobility of this sample is only $60\text{ cm}^2\cdot\text{V}^{-1}\cdot\text{s}^{-1}$. This is similar in character to degenerate bulk Si with a B dopant concentration of $1.5\times 10^{19}\text{ cm}^{-3}$ [57]. However, the behavior of this sample is not identical to degenerate Si. For instance, the temperature dependence of the resistivity of degenerate Si is not the same as that for sample S211 shown in Fig. 5.5a. From the linear part ($T < 100\text{ K}$) of the semilog resistivity dependence of the inverse temperature plot of Fig. 5.5a, the activation energy of the acceptor in S211 is estimated to be 17 meV, which is radically different from the ionization energy of boron (45 meV). The presence of this low activation energy and the low mobility at high temperatures suggests that the conduction in $\text{Ge}_x\text{Si}_{(1-x)}$ alloy layers is significant even at high temperatures. It is found in Takeda et al. [56] that the mobility is lower in $\text{Ge}_x\text{Si}_{(1-x)}$ alloys, for all compositions and temperatures. The lower activation energy for the acceptor can probably be explained by the existence of lower energy states in the $\text{Ge}_x\text{Si}_{(1-x)}$ layer which arise from the differences in the energies of the valence bands (ΔE_v).

The other two samples, S222 and S210, show the characteristics of compensated bulk Si with a dopant concentration of $\approx 5\times 10^{17}\text{cm}^{-3}$ [57]. The sheet charge densities of these two samples exhibit a usual freezeout behavior as shown in Fig. 5.5b. The hole mobilities of samples S210 and S222 exhibit temperature dependences of $\approx T^{-1.6}$ and $\approx T^{-1.4}$ for $T > 140\text{ K}$ respectively.

This temperature dependence is very similar to that of p-type Si with a impurity concentration of 10^{17} cm^{-3} [57]. As shown in Fig. 5.5c, The Hall mobility falls from a peak value of $450 \text{ cm}^2 \cdot \text{V}^{-1} \cdot \text{s}^{-1}$ at 90 K to a value of $100 \text{ cm}^2 \cdot \text{V}^{-1} \cdot \text{s}^{-1}$ at 30 K. At this point, The Hall mobility experiences a rapid decline as the carriers freeze out and for temperature below 30 K the hopping mechanism is the main source of conduction. From the linear part (for $T < 30$ K) of the semilog resistivity dependence of the inverse temperature plots of Fig. 5.5a the activation energies for the hopping conductivity are estimated to be 5.9 meV and 5.4 meV for S210 and S222 respectively. These values indicate that the hopping conductivity occurs for an impurity concentration of the order of $\approx 10^{17} \text{ cm}^{-3}$. The acceptor activation energies for samples S222 and S210 are also estimated from Fig. 5.5a to be 42.1 and 46.7 meV respectively. These values are close to the ionization energy of boron impurities in Si.

The Ge content, x , in samples S211, S222 and S210 is 0.087, 0.046 and 0.04 respectively. The relation describing the valence band discontinuity [45],

$$\Delta E_v = 0.74x, \quad (5.1)$$

gives (ΔE_v) 's of 64.4, 34.0 and 29.6 meV. Only sample S211, which exhibits the 2-DHG behavior, has a ΔE_v larger than the ionization energy of B. The lack of 2- DHG behavior for the two samples S222 and S210 can be attributed to the small ΔE_v in comparison with the ionization energy of B. The fact that the activation energies are inversely proportional to ΔE_v demonstrates that the conduction in the $\text{Ge}_x\text{Si}_{(1-x)}$ layer is significant.

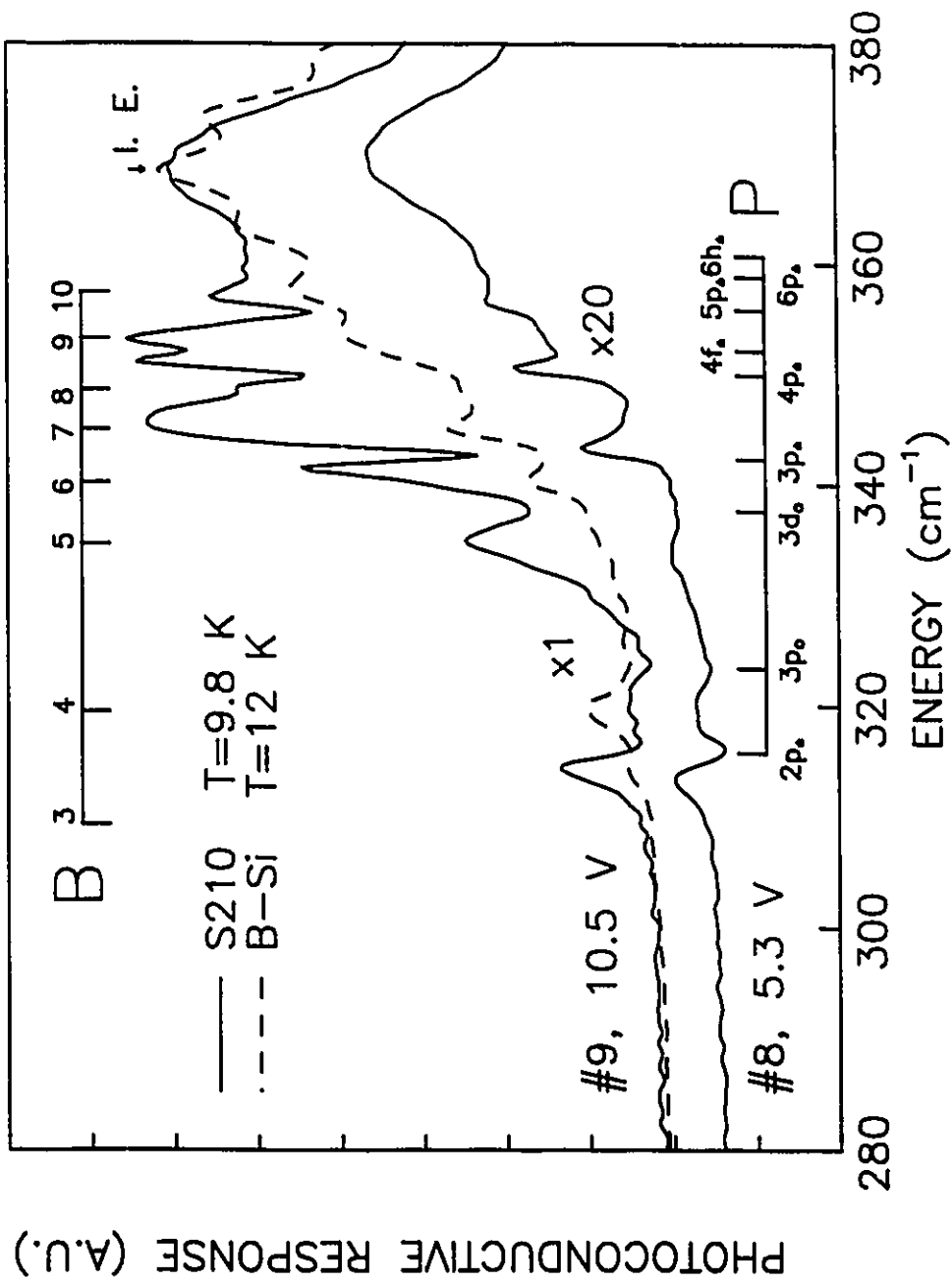
5.6 PTIS OF $\text{Ge}_x\text{Si}_{(1-x)}/\text{Si}$

PTI spectra for the $\text{Ge}_x\text{Si}_{(1-x)}/\text{Si}$ strained-layer heterostructure samples are presented in this section. It is found that sample S211, which displays a 2-DHG behavior, does not show a strong photoresponse. This is probably due to the number of photogenerated carriers being small in comparison with the number of residual hole carriers. Conversely, samples S210 and S222 show a strong photoresponse. As a result, the PTIS spectra presented here will concentrate on these two samples.

Figure 5.6 shows the PTI spectra of sample S210, at a temperature of 9.8 K, in the absence of band-edge light for two different applied voltages (5.3 and 10.5 V). It is striking to note the vast differences between the two spectra. It is found that the positive peaks in spectrum no. 8 can be identified as P transitions lines. By comparing this spectrum with spectrum no. 5 in Fig. 5.3a for the n-type substrate, it is found that they are similar. Therefore, it is concluded that the photoresponse from the n-type substrate dominates the resulting spectrum. However, as higher voltages are applied, these P transition lines appear as negative peaks in the PC continuum as shown in spectrum no. 9. As will be discussed, this PC continuum is in fact from the PTI of the impurity in the epitaxial layer, particularly from the B-doped Si layer. Thus, it is concluded that the photoresponse is dominated by the substrate for low applied voltages.

To understand the above phenomena, the structure of the sample and how the electrical contacts are made for the PTIS measurements need to be discussed. The epitaxial layers, which are p-type, were grown on n-type Si substrates. Ohmic contacts are made to the p-type epitaxial layer,

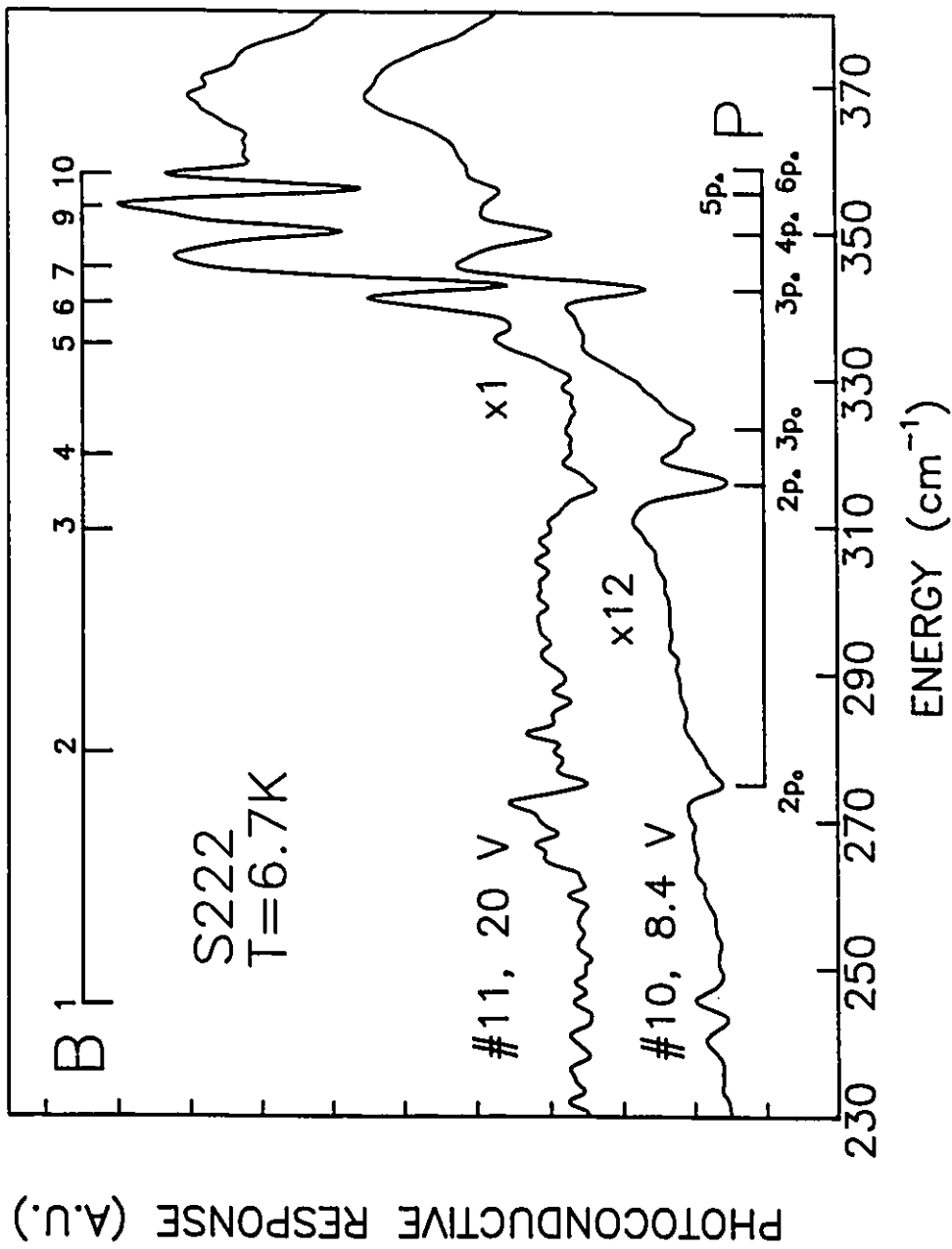
Figure 5.6 PTI spectra for sample S210 at a temperature of 9.8 K, without band-edge light, for two different applied voltages: no. 8 with 5.3 V and no. 9 with 10.5 V. The known excited states of P and B in bulk Si are shown. The relative photoresponse signal has been multiplied by 20 in spectrum no. 5. The PTI spectrum no.2 of B-doped Si is also shown for comparison with spectrum no. 9. Spectrum no. 2 has been adjusted so that its photoresponse in the region of the ionization energy (I. E.) of boron in Si is approximately matched to that of spectrum no. 9.



and since the substrate is n-type, any current flowing through the substrate will "see" a P-N-P structure. This will seriously limit the amount of current flowing through the substrate. It is well known that the photoresponse is proportional to the drift velocity of the excited charge carriers. For a low applied voltage, the induced electric fields in the epitaxial layer and substrate are both small. However, the carrier mobility in the substrate is much higher than that in the epitaxial layer because it is lightly doped. Hence, the excited free carriers in the substrate will have a higher drift velocity and this will result in a larger photoresponse. Increasing the applied voltage has a much smaller effect on the substrate due to the blocking contact in the reverse-bias P-N junction. On the other hand, increasing the applied voltage has a substantial effect on the epitaxial layer, which has ohmic contacts. As the applied voltage increases, the drift velocity of the excited carriers also increases. Thus, at a sufficiently high voltage, the photoresponse in the epitaxial layer will dominate the resulting spectrum. Spectrum no. 9 exhibits this behavior, since the effects of the boron impurity in the epitaxial layer overshadows those of the phosphorous majority impurity in the substrate. The negative peaks, which can be identified as excited states of P, are probably due to a photoresponse from the substrate. That is, the photoresponse of the P impurity in the substrate behaves like the photoresponse of a minority impurity of a sample with band-edge light. Another mechanism, which will increase the photoresponse in the epitaxial layer when the applied voltage is high, is impact ionization. This will be discussed later.

Fig. 5.7 shows the PC spectra for sample S222 at a temperature of 6.7 K without band-edge light, for two different applied voltages (8.4 and 20 V). These spectra are similar to spectrum no. 9 in Fig. 5.6, in that the P

Figure 5.7 PTI spectra for sample S222, at a temperature of 6.7 K, without band-edge light, with two different applied voltages: no. 10 with 8.4 V and no. 11 with 20 V. The known excited states of P and B in bulk Si are shown.

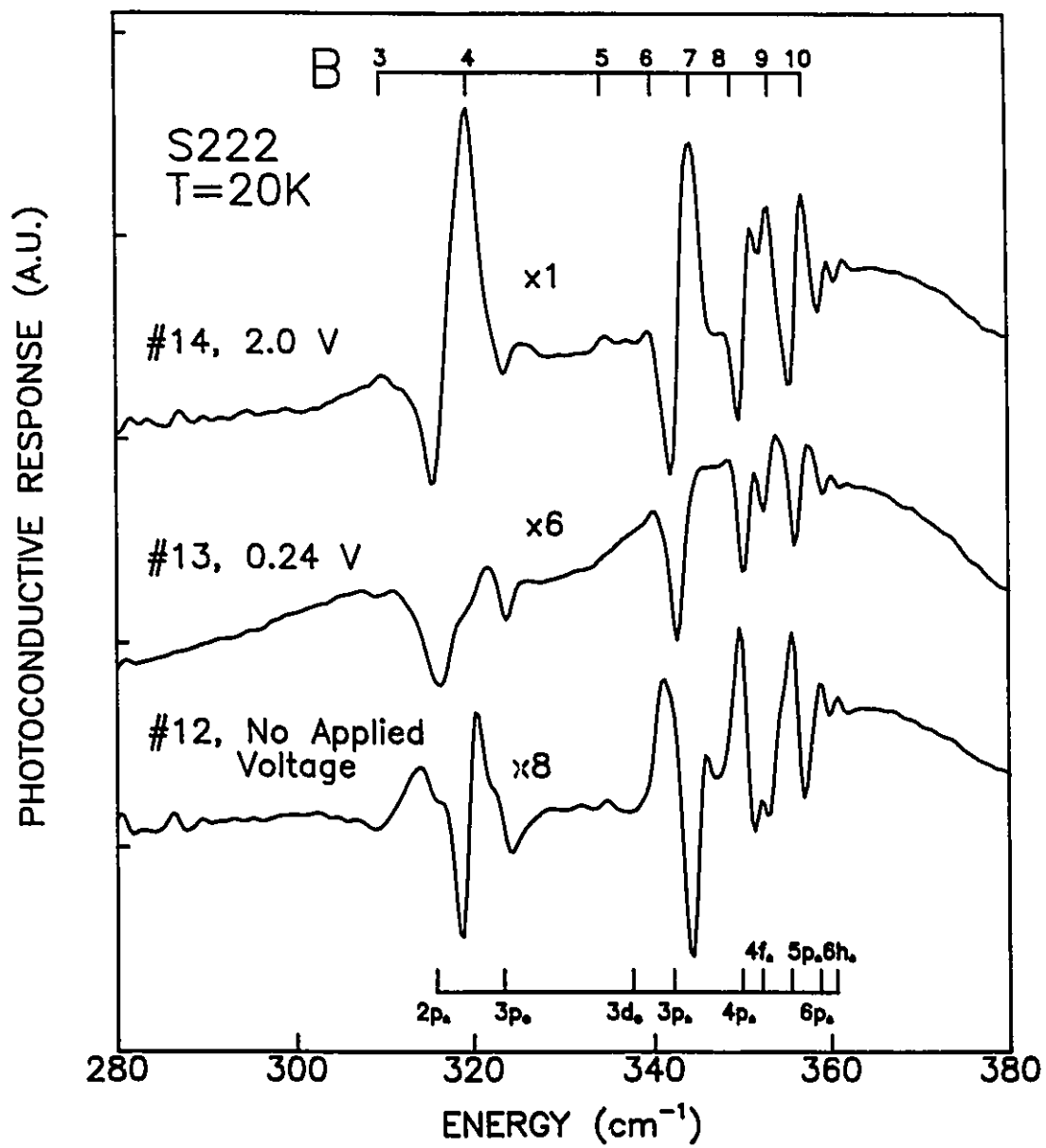


transition lines appear as negative peaks in the PC continuum of B. In fact, when the applied voltage is low, sample S222 behaves in the same manner as sample S210, whereby the substrate dominates the photoresponse. There are some interesting features which appear in these low temperature spectra (nos. 9, 10, 11). First, the PC continuum of these spectra develops at much lower frequencies compared with the typical response of B or P impurities in Si. For instance, the PC continuum starts at a lower frequency for spectrum no. 9 than that of spectrum no. 2 for the B-doped Si sample as shown in Fig. 5.6. Second, the relative response for the region between 340 and 360 cm^{-1} increases as the applied voltage increases as demonstrated in Fig. 5.7. Third, the intensities of the excitation lines increase as higher voltage is applied as shown in Fig. 5.7.

The influence of an electric field on the line intensity in PTIS has been investigated previously [58]. It is found that the impact ionization of the optically excited impurity atoms plays an important role in the photoresponse; the intensities of the excitation lines increase as higher electric fields are applied. As shown in Fig. 5.7, the impurity whose photoresponse dominates the PC continuum in spectrum no. 10 cannot be easily identified; however, as higher voltage is applied, as in spectrum no. 11, some positive peaks (for instance, 7, 9, 10 states) can now be identified as B excitation states.

The photoimpact mechanism cannot account for the PC continuum originating at lower frequencies. It was shown in section 5.5 that the valence band discontinuity, ΔE_v , will lower the activation energy. The PC continuum starting at a lower energy is consistent with this behavior. The lower PC continuum may also demonstrate that some of the free holes generated in

Figure 5.8 PTI spectra for sample S222, at a temperature of 20.0 K, with band-edge light and three different applied voltages: no. 12 with no applied voltage, no. 13 with 0.24 V and no. 14 with 2.0 V. The known excited states of P and B in bulk Si are shown.



the B-doped epitaxial layer will go to the $\text{Ge}_x\text{Si}_{(1-x)}/\text{Si}$ interface because of the lower energy states. These carriers will make a significant contribution to the PTI spectra because of the much higher mobility in the $\text{Ge}_x\text{Si}_{(1-x)}/\text{Si}$ layer as discussed in section 5.3. The strong electric field dependence between 340 and 360 cm^{-1} may be due to the fact that the hot carriers assist the optically excited impurity holes in tunnelling through the potential barrier in the Si layer. Another possible explanation is that the strong electric field may lower the effective potential barrier in such a way that the optically excited holes will tunnel through this barrier with higher probability.

Figure 5.8 shows the PTI spectra of sample S222 at a temperature of 20 K in the presence of band-edge light for three different applied voltages (0.0, 0.24, and 2.0 V). It is interesting to note that spectrum no. 12 was obtained without an applied voltage. In fact, it was found that all of the $\text{Ge}_x\text{Si}_{(1-x)}/\text{Si}$ epitaxial samples exhibited a photovoltaic response, whereby a photovoltaic potential is generated when the sample is illuminated with band-edge light. The cause of this effect is uncertain. It may be related to the inhomogeneity of the epitaxial layers, and the P-N junction between the B-doped layer and the n-type substrate or between the B-doped layer and the non-intentionally doped layer which may be n-type. The photovoltaic potential is around 130 mV when the sample is illuminated with the tungsten halogen lamp from the spectrometer for temperatures between 6 and 20 K.

In spectrum no. 12, the positive peaks are identified as P transition lines, whereas the negative peaks are identified as B transition lines. Comparing this spectrum with spectrum no. 7 of Fig. 5.3b, it can be concluded that the photoresponse is mainly due to the substrate. However, when a small voltage is applied, the P peaks are reversed as shown in spectrum no.

13. A higher applied voltage will intensify the P and B transition lines as shown in spectrum no. 14. It is concluded that the PC response of the last two spectra is dominated by the epitaxial layer. Unlike the response without band-edge light, a large applied voltage is no longer needed to produce a PC response which is dominated by the epitaxial layer. This behavior may result for two possible reasons. First, it is known that the carrier mobility is limited by ionized impurities at low temperatures [32, 24], the neutralization of ionized impurities will substantially improve the carrier mobility in the epitaxial layer relative to the substrate. This results from the fact that the substrate has a lower concentration of impurities than the epitaxial layer. Second, the absorption coefficient of Si is large (10^3 to 10^4 cm^{-1}) [59] for photon energies (1.8 to 2.5 eV) which comprise the band-edge light. Most of the band-edge light will be absorbed in the epitaxial layers; therefore, there is a carrier concentration gradient across the sample. This will substantially reduce the resistance in the epitaxial layer, while having a smaller effect on the substrate. The low resistance region will dominate the PC response. Thus, the presence of band-edge light will make it easier for the epitaxial layer to dominate the PC response. Sample S210 exhibits a similar response under similar experimental conditions. From this analysis, it is concluded that B and P are the dominant majority and minority impurities in the epitaxial layers. Table 5.2 lists the B and P transition lines observed in sample S222 with the band-edge light. In comparison with the known transition lines in bulk Si, they correspond to the same energies within the experimental uncertainty. This indicates that the free carriers are mainly generated in the unstrained heavily B-doped Si epitaxial layers.

TABLE 5.2. Boron and phosphorus excited state energies (cm^{-1}) observed when the PTIS spectra are obtained with band-edge light.

Energy Level	Boron (B) (cm^{-1})		Energy Level	Phosphorus (P) (cm^{-1})	
	This work	Literature value ^b		This work	Literature value ^b
2	277.8	278.39	2p _o		275.08
3	309.7	309.51	2p _±	315.8	315.93
4	319.6	319.37	3p _o	323.5	323.40
4A		320.05	3d _o	337.8	337.6 ^c
4B		321.87	4p _o		340.87
5	335.1	334.38	3p _±	342.2	342.38
6	340.0	340.01	4f _o		348.77
7	344.4	344.74	4p _±	349.9	349.87
8		349.0 ^b	4f _±	352.2	352.27
9	353.3	353.7 ^b	5f _o		354.33 ^c
10	357.1	357.4 ^b	5p _±	355.5	355.77
			5f _±		357.36
			6p _±	358.8	358.78
			6h _±	360.4	360.70

^a From ref. 49 unless otherwise noted.

^b From ref. 50.

^c From ref. 51.

5.7 CONCLUSIONS

The transport properties of the selectively boron-doped $\text{Ge}_x\text{Si}_{(1-x)}/\text{Si}$ strained-layer heterostructures have been presented. The effects of Ge content, x , in the $\text{Ge}_x\text{Si}_{(1-x)}$ layer have been demonstrated. It is concluded that the conductivity in this layer is significant; however, a large x is needed

to make the layer's conductivity play the dominant role and to ensure the presence of a 2-DHG behavior as exhibited by sample S211.

Far-infrared PTIS has been used to investigate the impurities of samples, S210 and S222, which do not show 2-DHG behavior. A comparison of the PTIS spectra of these samples to that of the underlying substrate reveals that the photoresponse from the substrate is dominant at low applied voltages. It is clear that a high purity substrate is desired if a photoresponse from the substrate is to be avoided. As the applied voltage is increased, the response from the epitaxial layers becomes evident. It was found that the excited impurity states in the epitaxial layer have the same energies as B or P impurities in bulk Si. Therefore, it is concluded that the majority impurity is identified as the intentional dopant boron while the dominant minority impurity is phosphorus. These results also indicate that the excited carriers come from the heavily B-doped epitaxial Si layers which are not strained. It was noted that the PC continuum starts at a lower energy region compared with bulk Si. This probably arises from the effects of ΔE_v and the importance of the PC response from the carriers conducted through the strained layer which has a much higher mobility. The strong voltage dependent photoresponse in the epitaxial layer is mainly attributed to a photoimpact mechanism.

In conclusion, the possibility of using the PTIS technique to probe the impurities in an epitaxial layer has been demonstrated. The impurities in the strained-layers have not been observed in these samples because the strained $\text{Ge}_x\text{Si}_{(1-x)}$ layers were not intentionally doped. They have much smaller absorption compared to the heavily B-doped layers; therefore, their PC response is not significant. However, further use of this technique to investigate the impurities in the strained $\text{Ge}_x\text{Si}_{(1-x)}$ layer is important, since

the excited impurity states often provide important information, such as the band structure of a material.

Appendix A

Schechter Envelope Functions

With the approximation of infinite spin-orbit splitting which is good for Ge, the acceptor wave functions have the form:

$$\psi_{\mu}(\mathbf{r}) = \sum_{\mathbf{p}=1}^4 F_{\mathbf{p}}^{\mu}(\mathbf{r})\varphi_{\mathbf{p}}(\mathbf{r}), \quad (A.1)$$

where μ refers to the μ -th degenerate state of the acceptor level and \mathbf{p} refers to the \mathbf{p} -th degenerate band. $\varphi_{\mathbf{p}}(\mathbf{r})$ are the Bloch wavefunctions at the top of the valence band, $F_{\mathbf{p}}^{\mu}(\mathbf{r})$ are the solutions of the effective-mass equations. These envelope functions $F_{\mathbf{p}}^{\mu}(\mathbf{r})$ for the acceptor ground state were first obtained by D. Schechter in the following form:

$$F^1(\mathbf{r}) = c_1 \begin{pmatrix} 1 \\ 0 \\ 0 \\ 0 \end{pmatrix} e^{-r/r_1} + \frac{c_2}{2} \begin{pmatrix} 3z^2 - r^2 \\ 0 \\ -\sqrt{3}(x^2 - y^2) \\ 0 \end{pmatrix} e^{-r/r_2} + ic_3 \begin{pmatrix} 0 \\ z(x + iy) \\ xy \\ 0 \end{pmatrix} e^{-r/r_2},$$
$$F^2(\mathbf{r}) = c_1 \begin{pmatrix} 0 \\ 1 \\ 0 \\ 0 \end{pmatrix} e^{-r/r_1} - \frac{c_2}{2} \begin{pmatrix} 0 \\ 3z^2 - r^2 \\ 0 \\ \sqrt{3}(x^2 - y^2) \end{pmatrix} e^{-r/r_2} - ic_3 \begin{pmatrix} z(x - iy) \\ 0 \\ 0 \\ -xy \end{pmatrix} e^{-r/r_2},$$

$$\begin{aligned}
F^3(r) &= c_1 \begin{pmatrix} 0 \\ 0 \\ 1 \\ 0 \end{pmatrix} e^{-r/r_1} - \frac{c_2}{2} \begin{pmatrix} \sqrt{3}(x^2 - y^2) \\ 0 \\ 3z^2 - r^2 \\ 0 \end{pmatrix} e^{-r/r_2} - ic_3 \begin{pmatrix} xy \\ 0 \\ 0 \\ z(x + iy) \end{pmatrix} e^{-r/r_2}, \\
F^4(r) &= c_1 \begin{pmatrix} 0 \\ 0 \\ 0 \\ 1 \end{pmatrix} e^{-r/r_1} + \frac{c_2}{2} \begin{pmatrix} 0 \\ -\sqrt{3}(x^2 - y^2) \\ 0 \\ 3z^2 - r^2 \end{pmatrix} e^{-r/r_2} + ic_3 \begin{pmatrix} 0 \\ -xy \\ z(x - iy) \\ 0 \end{pmatrix} e^{-r/r_2}.
\end{aligned}
\tag{A.2}$$

The parameters c_1 , c_2 , c_3 , r_1 and r_2 are obtained using the standard variational procedure. The values of the parameters for p-type Ge are listed in Table A.1.

TABLE A.1. Values of the Parameters for Ge.

r_1 (Å)	r_2 (Å)	c_1 $10^9 \text{cm}^{-3/2}$	c_2 $10^{21} \text{cm}^{-7/2}$	c_3 $10^{21} \text{cm}^{-7/2}$
^a 44.0	34.4	1.67	-2.15	4.68
^b 37.8	29.9	2.088	-2.60	7.85

^asee Ref. 24

^bsee Ref. 44

List of References

1. J. Blinowski and J. Mycielski, *Phys. Rev.* **136**, A266 (1964) and J. Blinowski and J. Mycielski, *Phys. Rev.* **140**, A1024 (1965).
2. R. C. Milward and L. J. Neuringer, *Phys. Rev. Lett.* **15**, 664 (1965) and L. J. Neuringer, R. C. Milward and R. L. Aggarval, *J. Phys. Soc. Jap. Suppl.* **21**, 582 (1966).
3. A. I. Demeshina, R. L. Korchazhkina, N. N. Kuznetsova and V. N. Murzin, *Sov. Phys. Semicond.* **4**, 363 (1970).
4. R. A. Smith, S. Zwerdling, S. N. Dermatis and J. P. Theriault, Pro. IXth Int. Conf. on Phys. of Semiconductors, Moscow, 1968 (Nauka, 1968), p. 149.
5. S. Zwerdling and J. P. Theriault, *Infrared Phys.* **12**, 165 (1972).
6. Y. Nakagawa and H. Yoshinaga, *J. Phys. Soc. Jap.* **30**, 1212 (1972).
7. V. S. Vavilov, A. G. Kazanskii, O. G. Koshelev and P. V. Reznikov, *Sov. Phys. Semicond.* **10**, 947 (1976).
8. E. Kaczmarek and Z. W. Gortel, *Phys. Rev. B* **10**, 2535 (1974).
9. Neutron Transmutation Doping in Semiconductors. ed. by J. Meese. New York: Plenum Press, 1979.
10. E. E. Haller, N. P. Palaio and M. Rodder, in Neutron Transmutation Doping of Semiconductor Materials. ed. by R. D. Larrabee. New York: Plenum Press, 1982.
11. Sir Nevill Mott, Metal-Insulator Transitions. New York: Barnes and Nobles Books, 1974.

12. B. I. Shklovskii and A. L. Efros, Electronic Properties of Doped Semiconductors. New York: Springer-Verlag, 1984.
13. M. Banaszkiewicz, *Phys. Stat. Sol. B* **69**, 247 (1975).
14. S. D. Baranovskii and A. A. Uzakov, *Sov. Phys. Semicond.* **16**, 1026 (1982).
15. S. Tanaka and H. Y. Fan, *Phys. Rev.* **132**, 1516 (1963).
16. A. Miller and E. Abrahams, *Phys. Rev.* **120**, 745 (1960).
17. A. L. Efros and B. I. Shklovskii, in Electron-Electron Interactions in Disordered Systems. ed. by A. L. Efros and M. Pollak. Amsterdam: North-Holland, 1985.
18. A. L. Efros and B. I. Shklovskii, *J. Phys. C: Solid State Phys.* **8**, L49 (1975).
19. A. L. Efros, *J. Phys. C: Solid State Phys.* **9**, 2021 (1976).
20. J. H. Davies, P. A. Lee and T. M. Rice, *Phys. Rev. B* **29**, 4260 (1984).
21. S. D. Baranovskii, B. I. Shklovskii and A. L. Efros, *Sov. Phys. JETP* **51**, 199 (1980).
22. S. D. Baranovskii and A. A. Uzakov, *Sov. Phys. Semicond.* **15**, 533 (1981).
23. B. I. Shklovskii and A. L. Efros, *Sov. Phys. JETP* **54**, 218 (1981).
24. D. Schechter, *J. Phys. Chem. Solids* **23**, 237 (1962).
25. E. Kaczmarek, *Acta Phys. Polon.* **30**, 267 (1966), E. Kaczmarek, *Acta Phys. Polon.* **30**, 277 (1966) and E. Kaczmarek, *Acta Phys. Polon.* **30**, 283 (1966).
26. Z. W. Gortel and E. Kaczmarek, *Acta Phys. Polon.* **A41**, 641 (1972).
27. Y. A. Osip'yan, V. M. Prokopenko and V. I. Tal'yanskii, *Sov. Phys. JETP* **60**, 156 (1984).
28. K. Kuriyama, M. Yahagi, and K. Iwamura, *J. Appl. Phys.* **54**, 673 (1983).

29. G. Cripps, Master Thesis, McMaster University, 1986.
30. S. F. Mughabghab, M. Divadeenam and N. E. Holden, Neutron Cross Sections, Volume 1. New York: Academic Press, 1981.
31. Van der Pauw, *Philips Res. Repts.* **13**, 1 (1958).
32. K. Seeger, Semiconductor Physics. New York: Springer-Verlag, 1985.
33. F. J. Morin *Phys. Rev.* **93**, 62 (1954).
34. S. M. Sze, Physics of Semiconductor Devices. New York: John Wiley & Sons, 1981.
35. J. Harvey, Director of Health Physics, private communication.
36. I. S. Park and E. E. Haller, *J. Appl. Phys.* **64**, 6775 (1988).
37. C. M. Randall and R. D. Rawcliffe, *Applied Optics* **6**, 1889 (1967).
38. R. J. Bell, Introductory Fourier Transform Spectroscopy. New York: Academic Press, 1972.
39. R. L. Jones and P. Fisher, *J. Phys. Chem. Solids* **26**, 1125 (1965).
40. G. A. Thomas, M. Capizzi, F. DeRosa, R. N. Bhatt and T. M. Rice, *Phys. Rev. B* **23**, 5472 (1981).
41. F. W. Wooten, Optical Properties of Solids. New York: Academic Press, 1972.
42. S. M. Sze, Semiconductor Devices. New York: John Wiley & Sons, 1985.
43. P. Fisher and A. K. Ramdas, in Physics of the solid state. ed. by S. Balakrishna, M. Krishnamurti and B. Ramachandra. London: Academic Press, 1969.

44. K. Suzuki, M. Okazaki, and H. Hasegawa, *J. Phys. Soc. Jap.* **19**, 930 (1964).
45. R. People, *IEEE J. Quantum Electronics*. **QE-22**, 1696 (1986).
46. Sh. M. Kogan and T. M. Lifshits, *Phys. Status Solidi A* **39**, 11 (1977).
47. R. People, J. C. Bean, and D. V. Lang, *J. Vac. Sci. Technol.* **A3**, 846 (1985).
48. E. E. Haller, *Mikrochim Acta* **III**, 241 (1987).
49. M. S. Skolnick, L. Eaves and R. A. Stradling, *Solid State Comm.* **15**, 1403 (1974).
50. A. Onton, P. Fisher and A. K. Ramdas, *Phys. Rev.* **163**, 686 (1967).
51. B. Pajot, J. Kauppinen and R. Anttila, *Solid State Comm.* **31**, 759 (1979).
52. E. M. Bykova, T. M. Lifshits and V. I. Sidorov, *Sov. Phys. Semicond.* **7**, 671 (1973).
53. L. S. Darken and S. A. Hyder *Appl. Phys. Lett.* **42**, 731 (1983).
54. G. Bambakidis and G. J. Brown *Phys. Rev. B* **33**, 8180 (1986).
55. H. Morkoc, in The Technology and Physics of Molecular Beam Epitaxy. ed. by E. H. C. Parker. New York: Plenum Press, 1982.
56. K. Takeda, A. Taguchi, and M. Sakata, *J. Phys. C: Solid State Phys.* **16**, 2237 (1983).
57. F. J. Morin and J. P. Maita, *Phys. Rev.* **96**, 28 (1954).
58. E. A. Kurkova and V. I. Sidorov, *Sov. Phys. Semicond.* **9**, 850 (1976).
59. W. C. Dash and R. Newman, *Phys. Rev.* **99**, 1151 (1955).